PhD Thesis 2013 Ankush

SYNTHESIS AND CHARACTERIZATION OF $SrFe_{12}O_{19}$: EFFECTS OF RARE EARTH ELEMENTS ON STRUCTURAL, MORPHOLOGICAL AND MAGNETIC PROPERTIES

BY

ANKUSH

DEPARTMENT OF PHYSICS AND MATERIALS SCIENCE

JAYPEE UNIVERSITY OF INFORMATION TECHNOLOGY

WAKNAGHAT, SOLAN-173234, INDIA

JULY 2013

SYNTHESIS AND CHARACTERIZATION OF $SrFe_{12}O_{19}$: EFFECTS OF RARE EARTH ELEMENTS ON STRUCTURAL, MORPHOLOGICAL AND MAGNETIC PROPERTIES

THESIS SUBMITTED IN THE FULFILLMENT OF THE REQUIREMENTS

FOR THE DEGREE OF

DOCTOR OF PHILOSOPHY

IN

PHYSICS

BY

ANKUSH

DEPARTMENT OF PHYSICS AND MATERIALS SCIENCE

JAYPEE UNIVERSITY OF INFORMATION TECHNOLOGY

WAKNAGHAT, SOLAN-173234, INDIA

JULY 2013

CERTIFICATE

This is to certify that the thesis entitled, **"SYNTHESIS AND CHARACTERIZATION OF $SrFe_{12}O_{19}$: EFFECTS OF RARE EARTH ELEMENTS ON STRUCTURAL, MORPHOLOGICAL AND MAGNETIC PROPERTIES"** which is being submitted by **Mr. Ankush** in fulfillment for the award of degree of **Doctor of Philosophy** in **Physics** by the **Jaypee University of Information Technology**, is the record of candidate's own work carried out by him under our supervision. This work has not been submitted partially or wholly to any other University or Institute for the award of this or any other degree or diploma.

Date: July 22, 2013

Prof. P.B. Barman

Supervisor
Department of Physics and Materials Science
Email: Pb.barman@juit.ac.in
Phone: +91 9418228268

Dr. Ragini Raj Singh

Co-Supervisor
Department of Physics and Materials Science
Email: raginirajsingh@gmail.com
Phone: +91 9625643296

To my parents

&

My Sisters

ACKNOWLEDGMENT

With a deep sense of gratitude and profound thankfulness; I would like to express my deep and sincere gratitude to my PhD supervisors, **Prof P.B. Barman** and **Dr. Ragini Raj Singh** for all the support and persistent encouragement extended to me throughout my research period. I am always grateful to them for their competent advice and sustained guidance without which the successful completion of this work would not have been possible.

I truly thank to JUIT authorities especially **Dr. Y. Medury (COO)**, **Prof. Ravi Prakash (Ex-Vice Chancellor)** and **Director, Brig. (Retd.) Balbir Singh** for providing me every kind of financial and administrative assistance during entire course.

I extend my warm and sincere thanks to Prof. Sunil Kumar Khah, Dr. Vineet Sharma, Dr. Poonam Sharma, Dr. Rajesh Kumar, Dr. Surajit Kumar Hazra, Dr. Pankaj Sharma, Dr. Dheeraj Sharma, Dr. Sanjiv Kumar Tiwari, Dr. Rakesh Kr Bajaj, Dr. Tiratha Raj Singh and Dr. Aman Mahajan for consistent support.

I am thankful to our librarian Mr. Shri Ram, Mr. Kamlesh Mishra, Mr. Ravendra Kumar Tiwari, Mr. Ashok Kishtwal (CS/IT), Mr. Hardeep Singh Rana (CS/IT), Mr. Vineet Paliwal (CS/IT) and Mr. Shambhunath (ECE) for their cooperation during entire work.

I would like to express my deep sense of gratitude and indebtedness to my Parents, Shri. Suresh Kumar, Smt. Shashi Lata Thakur and my sisters for their complete association and unflagging love during my research work.

I am really thankful to my friends: Satwinder Singh, Neha Sharma, Sunanda Sharda, Sharad Suthar, Pawan Kumar, Abhishek Kandwal, Hitanshu, Dikshita Gupta, Madan Mohan Sati, Ved Prakash, Manoj Gaur, Piyush Chauhan, Ankit Srivastava, Arun Prashar, Paviter Singh, Anshuman Shai (JUIT-Noida), Sunil (JUIT-Noida), Suresh Lakhanpal and Archit Sood from JUIT who rendered every type of assistance and provided me a convivial place to work.

I would like to acknowledge Panjab University and NIPER-Mohali with special thanks for providing the necessary characterization facility for the determination of structural, morphological and thermal properties of the materials under Sophisticated

Analytical Instrumentation Facility and Central Instrumentation Laboratories project, respectively. Many thanks also go to the Dr. Aman Mahajan, Assistant Professor, Department of Physics-GNDU, Amritsar, for the assistance on the electrical and dielectrical measurements. I am also indebted to Dr. Ramesh Chandra at the IIC, IIT Roorkee for the assistance on the VSM and SEM measurements.

Finally, for the completion of this work, I thank to the almighty God for fulfilling my desire to complete this study under his kind blessings.

Date: July 22, 2013 **(ANKUSH)**

CONTENTS

Abstract

This thesis work preferentially concerned with the study of thermal, structural, morphological and magnetic properties of strontium hexaferrite nanoparticles along with their derivatives. The basic compositions of synthesized nanoparticles are:

I. $SrF_{12}O_{19}$ (at different calcinations temperature)
II. $SrLa_xFe_{12-x}O_{19}$ (x = 0.0, 0.23, 0.43, 0.63, 0.83 and 1.0)
III. $SrNd_xFe_{12-x}O_{19}$ (x = 0.0, 0.23, 0.43, 0.63, 0.83 and 1.0)
IV. $SrCe_xFe_{12-x}O_{19}$ (x = 0.0, 0.23, 0.43, 0.63, 0.83 and 1.0)

The work has been systematically described in seven different chapters.

Chapter I contains a brief introduction of nanoferrites and their general properties.

Chapter II describes the synthesis of hexaferrite nanoparticles and experimental technique used for the characterization of synthesized nanoparticles for thermal, structural, morphological and magnetic properties.

Chapter III crystallization kinetics of strontium hexaferrite has been investigated by TG/DTG/DTA. The precursor and calcinated $SrF_{12}O_{19}$ sample have been characterized for structural, chemical, morphological and magnetic properties using X-ray diffraction (XRD), Fourier transform infrared spectroscopy (FTIR), scanning electron microscopy (SEM) and vibrating sample magnetometer (VSM) respectively.

Chapter IV concerns with the substitutional effects of La^{3+} on structural, morphological and magnetic properties.

Chapter V describes the first report on Nd^{3+} doped M-type hexaferrite nanoparticles: $SrNd_xFe_{12-x}O_{19}$ ($0 \leq x \leq 1$) prepared by citrate precursor using the sol-gel technique followed by gel to crystallization. The influence of the Nd^{3+} substitution, Fe^{3+}/Sr^{2+} molar ratio and the calcination temperature on the crystallization of ferrite phase have been examined. The structural analysis has been

analysized by using XRD and FTIR. The magnetic behaviour of synthesised nanoparticles has been investigated by VSM.

Chapter VI contains the synthesis of $SrCe_xFe_{12-x}O_{19}$ nanoparticles; and structural, morphological and magnetic properties of synthesized powders have been systematically investigated by using XRD, FTIR, SEM and VSM, respectively.

Finally, overall conclusion of the work is described in chapter VII.

List of Publications

- "Crystallization Kinetics of Strontium Hexaferrite: Correlation to Structural, Morphological, Dielectric and Magnetic Properties" **Ankush Thakur**, R. R. Singh and P. B. Barman *Electronic Materials Letters* **8** (2012) 595.
- "Structural and Magnetic Properties of La^{3+} Substituted Strontium Hexaferrite Nanoparticles Prepared by Citrate Precursor Method" **Ankush Thakur**, R. R. Singh and P. B. Barman *Journal of Magnetism and Magnetic Materials* 326 (2012) 35.
- "Synthesis and Characterizations of Nd^{3+} doped $SrFe_{12}O_{19}$ Nanoparticles" **Ankush Thakur**, R.R. Singh and P.B. Barman, *Journal of Material Chemistry and Physics* Accepted (2013).
- "Preparation and Crystallization kinetics in Ce^{3+} substituted $SrFe_{12}O_{19}$ nanoparticles: Comparative study of magnetic properties for different rare earth elements" **Ankush Thakur**, R.R. Singh, R. Kumar, M. Kumar and P.B. Barman, under review in *Material Research Bulletin.*
- "Effects of La^{3+}-Nd^{3+} ions and pre-calcination on the growth of hexaferrite nanoparticles prepared by gel to crystallization technique" **Ankush Thakur**, R.R. Singh and P.B. Barman under review in *Acta Materialia*.

Participation and presentations in workshops/Seminars/Conference

- "Influence of La^{3+}-Nd^{3+} ions on the growth of hexaferrite nanoparticles" **Ankush Thakur**, R.R. Singh, P.B. Barman, International Conference on Nanoscience and Technology ICN+T, at Paris France, Sep 9-13, 2013 (Accepted for Oral Presentation).
- "Thermal analysis of strontium hexaferrite nanoparticles using TG/DTA" **Ankush Thakur**, R.R. Singh, P.B. Barman, International Conference on material Science and Engineering ICMSE, at Guilin, Guangxi, China, Oct 4-06, 2013 (Accepted).

- "Influence of Ce^{3+}-La^{3+} content on the formation of strontium hexaferrite nanoparticles" **Ankush Thakur**, R.R. Singh, P.B. Barman, National Conference on Multifunctional Advanced Materials, at Shoolini University, Solan, India, May 2-04, 2013.
- "A Study on the Formation of Nanocrystalline Strontium Hexaferrite Produced *via* a Citric acid and Glycine as a Chelating Agent" **Ankush Thakur**, R.R. Singh, P.B. Barman, International Conference on Macro and Supramolecular Architectures and Materials held at Coimbatore (Tamil Naidu), India, Nov. 21-25 2012.
- MRSI two days workshop on "Antenna Materials" Attended held at JUIT, Waknaghat, Solan, H.P., India, Dec 14-15, 2012.
- "Synthesis and Characterization of Strontium Hexaferrite" **Ankush Thakur** and P.B. Barman, 2nd conference on "Advanced Materials and Radiation Physics" held at Longowal (PB.), India during 04-05 Nov. 2011.
- IUCEE workshop on "Electronic and Opto-electronic Materials" held at JUIT, Waknaghat, Solan, H.P., India, 30-05-2011 to 03-06-2011.
- "Magnetic Properties of Strontium Hexaferrite" **Ankush Thakur**, A.K. Srivastava and P.B. Barman, National Conference on Recent Trend in Material Science, at JUIT, Waknaghat, Solan, H.P., India, (2010).

List of Figures

List of Tables

CHAPTER I

Introduction

1.1 Introduction

The technology can be used as to refer to a collection of techniques by which humans modify nature to meet their needs and wants. It is the application of mathematics, science and the arts for the benefit of life. The technology word designates for the study of something, or the branch of knowledge of a discipline. Presently, everything is depends on technology and no one can serve without it. Moreover, it decreases the human efforts and increases the efficiency. We think of technology in terms of its artifacts: computers and software, aircraft, pesticides, water-treatment plants, birth-control pills, and microwave ovens, to name a few. But technology is more than these tangible products. Technology includes the entire infrastructure necessary for the design, manufacture, operation and repair of technological artifacts from corporate headquarters and engineering schools to manufacturing plants and maintenance facilities. The knowledge and processes used to create and to operate technological artifacts: engineering know-how, manufacturing expertise and various technical skills are equally important parts of technology.

Nanotechnology refers to research and technology development at the atomic, molecular and macromolecular scale. Nanotechnology includes the fundamental understanding of nanomaterials in nanoscale. Study on fundamental relationships between physical properties and phenomena of nanometers are also referred to as nanoscience. Nanotechnology word was originated from a Greek world which means “dwarf” *i.e.* one billionth of a meter (1nm). One nanometer is approximately the length equivalent to 10 hydrogen or 5 silicon atoms aligned in a line [1]. The ability to fabricate and process nanomaterials and nanostructures is the first corner stone in nanotechnology. Nanostructured materials are those with at least one dimension falling in nanometer scale and include nanoparticles (including quantum dots, when exhibiting quantum effects), nanorods and nanowires, thin films and bulk materials made of nanoscale building blocks or consisting of nanoscale structures [2].

The historic birth of the nanotechnology is commonly credited to Feynman. Historically nanotechnology was for the first time formally recognized as a viable field of research with the landmark lecture delivered by Richard P. Feynman, the famous Noble Laureate physicist on December 29th 1959 at the annual meeting of the American Physical Society entitled "There's Plenty of Room at the Bottom - An

invitation to enter a new field of physics". Feynman stated in his lecture that the entire encyclopedia of Britannica could be put on the tip of a needle and in principle, there is no law preventing such an undertaking [1].

1.1.1 History of ferrites

The history of ferrite is believed to be before the birth of Christ around the time period of 800BC. The naturally occurring magnetic materials were ladestone that attract the iron piece consisting of the ore magnetite (Fe_2O_3). These stones were found in the district of Magnesia in Asia Minor, hence the mineral's name became magnetite (Fe_3O_4). In earlier century the people use these materials as compass to navigate and allowed mariners to find North without the use of the stars.

Professor Takeshi Takei [3] has put their efforts to improve the magnetic properties of magnetite for their magnetic applications. William Gilbert in 1600 published his work “De Magnete” on magnetism that describes the magnetic behavior of lodestone. No major achievement has been achieved for next two years but a milestone in the history of electromagnetism is occurred when in 1819, Hans Christian Oersted has observed the influence of electric current on magnetic needle. In this way number of researchers has worked on this idea that leads the development or basis of new science of electromagnetism. The research on soft ferrite was in progress in all parts of world. However, the production of soft ferrite did not come commercially before the discovery of JL Snoek 1945. In 1945, JL Snoek has successfully synthesized a soft ferrite in the Phillips Research Laboratories, Netherlands. JL Snoek found the importance of soft ferrite in different area or field etc. Snoek synthesized different type of ferrite including shape, size for inductor and antenna applications and in 1947, his work has been published the book entitled in New Developments in Ferromagnetic Materials. The theoretical modeling on ferrimagnetism, given by L Neel, provides the information for basic phenomenon of "spin-spin interaction". The idea of Neel develops a new stage in the field of ferrite. It helps to study crystal structure, crystal behaviour by material interaction and their properties. The development of microwave ferrites as reported E. Albers Schonberg leads the growth of ferrite era in field of electronic and telecommunication industry. The application and use of ferrite leads the miniturization of big devices. The unique

and novel properties of these materials make these ferrites still in demand in commercial, non-commercial as well as defence equipments field. However, magnetic materials have been widely used in early years for various area especially Neolithic men used the lodestone to navigate, where lodestone is an iron ore which is magnetic ceramic compound derived from iron oxides such as magnetite (Fe_3O_4). The magnetite is oxide materials which come in structural class of compounds generally known as spinels or soft ferrite. Ferrites are the class of the ferromagnetic materials and discussed in detail in the following section.

1.1.2 Ferrites

Ferrites are non-conductive ferromagnetic ceramic compounds which are mixed crystal of various metallic oxides such as hematite Fe_2O_3 and magnetite Fe_3O_4. It may be considered that these materials consist of oxygen ions in closed packed structure with cations. On the basis of their magnetic behaviour they are classified into two categories; soft and hard ferrite. Soft or hard does not mean that the materials are mechanically soft and hard, but refers to their low or high coercivity.

1.1.3 Classification of ferrites

Ferrites are often classified into three categories on the basis of their crystal structure and chemical formulas: spinel, garnet and magnetoplumbite.

1.1.3.1 Spinel ferrite

Spinel ferrite are represented by the chemical formula $MeFe_2O_4$ where M stands for several metallic elements *viz.* Fe, Mn, Mg, Ni, Zn, Cd, Co, Cu, Al etc [4]. Spinel ferrites have low magnetic anisotropies and easily reverse the direction of spins without dissipating much energy. However, they are highly resistive materials which prevent the eddy currents in the core.

1.1.3.2 Garnet ferrites

Garnet ferrites are cubic crystal in nature with formula $Me_3^{3+}Fe_5O_{12}$ or these ferrites consists oxides of rare earth elements (Table 1), where Me = Y, Sm, Eu, Gd, Tb, Dy, Ho, Er, Tm or Lu [4].

1.1.3.3 Magnetoplumbite ferrites

Magnetoplumbite ferrites are generally known as hard magnetic material due to high coercivity value [5]. They are hexagonal in structure with chemical formula $MeFe_{12}O_{19}$, where, Me = Sr or Ba. Strontium hexagonal ferrites are important and subject of present study. After the discovery of hexaferrite by Philips in the 1950s, degree of interest in these materials of researchers has increased and is still growing. These materials have been extensively used in modern technology applications such as magnetic recording media, telecommunications equipment, injection moulded pieces, plastoferrite, color imaging, ferrofluids as well as permanent magnets due to their appropriate properties including perfect mechanical, chemical and thermal stability [6]. These materials can also be useful for components in electrical devices due to their high resistivity, mainly those operating in the region of microwave to radio frequencies. Hexagonal hard ferrites are considered to be the most particulate media for perpendicular recording due to their, chemical, morphological and magnetic characteristics.

Table 1: Summary of different types of ferrite [5].

Spinel Ferrite	**$1Fe_2O_3 – 1MeO$**	**MeO- Transition metal oxide**
Garnet Ferrite	$5Fe_2O_3 – 3Me_2O_3$	Me_2O_3- Rare earth metal oxide
Magnetoplumbite Ferrite	$6Fe_2O_3 – 1MeO$	MeO- divalent metal oxide from group II A, SrO, BaO

The class of M-type ferrite was initially known as ferroxdure and to distinguish it from the spinel ferrite, it was named ferroxcube. Their structure was not confirmed as being isomorphous with the hexagonal magnetoplumbite until it was first studied and characterized magnetically in the early 1950s by Philips. The structures of hexaferrites are classified into five categories on the basis of chemical formula and crystalline structure *viz.* M-type or $SrFe_{12}O_{19}$, W-type or $SrMe_2Fe_{16}O_{27}$, Y-type or $SrMe_2Fe_{12}O_{22}$, X-type or $Sr_2Me_2Fe_{28}O_{46}$ and Z-type or $Sr_2Me_2Fe_{24}O_{41}$. Among the hexagonal ferrites, the M-type ferrites have greatest interest in the scientific as well as

technological field. M-type ferrites has a space group ($P6_3/mmc$) and often expressed as RSR*S* exhibit hard magnetic characteristics (Figure 1.1). The crystal structure of magnetoplumbite unit cell of the M-type hexagonal ferrite is combination of two structural blocks stacked along the c-axis consisting of 10 hexagonally closed-packed oxygen layers: RSR*S*. The S and R block stands for spinel and hexagonal structure. R* and S* are the blocks obtained by 180° rotation of R and S with respect to c-axis having equivalent atomic arrangements.

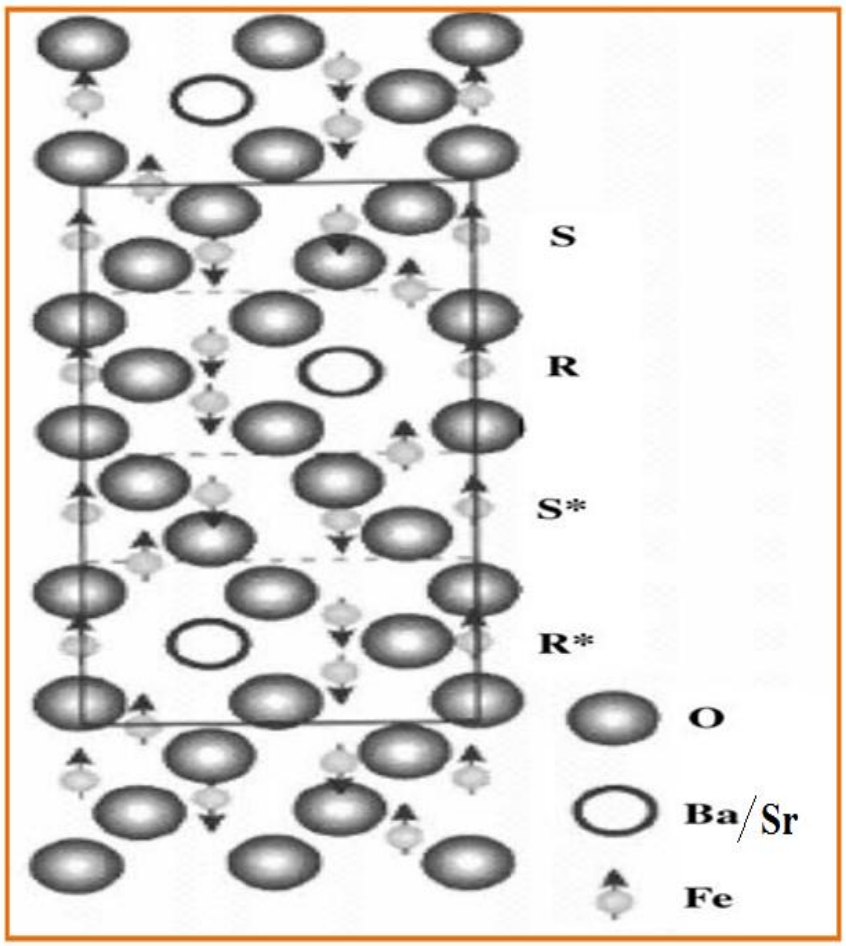

Figure 1.1: Crystal structure of hexaferrite [7].

$SrFe_{12}O_{19}$ contains 64 ions per unit cell on 11 different sites. The Fe^{3+} ions are distributed over five distinct crystallographic sites different in coordination and spin orientation, three octahedral sites (12k, 2a, $4f_2$), one tetrahedral site ($4f_1$) and trigonal bipyramidal site (2b) [8]. Among 12 Fe^{3+} ions in formula, 6 Fe^{3+} has been arranged in

12k sites having spin up direction. Similarly, both 2a and 2b sites contains one Fe^{3+} ions in up direction and 4 Fe^{3+} ions distributed over two different $4f_1$ and $4f_2$ site in downward directions. Here, if we take spin of the structure collectively than 8 Fe^{3+} ions are in up direction and 4 Fe^{3+}ions in downward direction which cancel the effect of each other. The magnetic moment of Fe^{3+} is $5\mu_B$ due to the presence of 5 unpaired electrons in 3d-orbit. The net magnetic moment per unit formula is 20 μ_B. These crystallographic sites are coupled with O^{2-} ions to form colinear ferrimagnetic order and superexchange interaction between Fe^{3+}-O^{2-}-Fe^{3+}. These sites are responsible for enhancement and dilution in various properties such as structural, morphological, electrical and magnetic. A significant improvement in various properties for hexaferrite have been achieved by altering the substitution cations from metal ion to rare earth elements on the Fe^{3+} or Sr^{2+} sites or both and can be controlled by varying the size and shape of the particles. Specific compositions have been determined using the phase diagram (Figure 1.2).

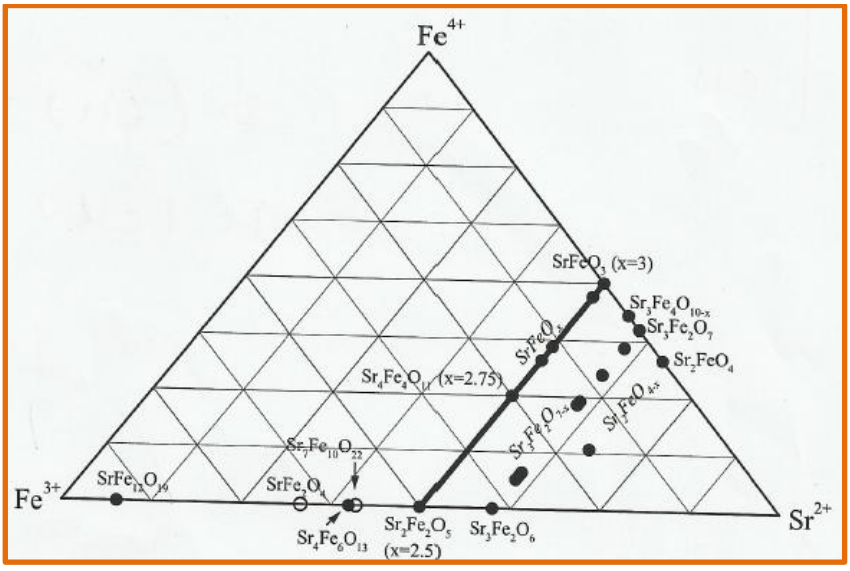

Figure 1.2: Phase diagram of SrO-Fe_2O_3 system [8].

1.1.4 Motivation of thesis work

Extensive research in the field of ferrite has started in 1950, after their discovery due to exceptional magnetic properties and still growing. These materials become very important commercially and technologically, than any other magnetic

material. Nanoparticles of these materials exhibit unique and different properties with respect to their bulk counterparts. The structural, morphological and magnetic properties of these materials can be easily controlled by changing their size. All the properties of ferrite nanoparticles are found to be sensitive to their composition, microstructure and substituted cations as well as synthesis mechanism and processing conditions. However, crystallite size and occupancy of substituted ions at different crystallographic sites may alter the magnetic properties of the materials. Also the production of ferrite will open the door for India in European countries in ferrite industry due to its economical range. It is estimated that by the year 2000AD, India will have capability to produce 10,000 MT of soft-ferrite and 18,000 MT of hard ferrite and may emerge as an important player in the ferrite sector, after meeting the internal demands, it is estimated that India shall be able to export 6000 MT of Hard Ferrites and about 3000 MT of soft ferrite. It will put India into a situation where it can be a major producer and exporter of ferrite products [9]. The ferrite materials have large coercivity and magnetization values which are useful in data storage devices etc. Recently, IBM in cooperation with Fuji Film announced fabrication of new magnetic tape based on hexaferrite nanoparticles with 15 times higher than any commercial tape available now [10]. That's why an investigation on strontium hexaferrite nanoparticles has been studied along with their derivatives.

The rare earth elements (La^{3+}, Nd^{3+}, Sm^{3+} and Gd^{3+}) act as inhibiting agent for the grain growth [11,12]. The inhibiting nature and low solubility leads the growth of secondary or undesired phases in synthesised material. The presence of these secondary phases dilutes the various properties of the material. An effort has been made to synthesise pure nanoparticles without any secondary phase even after the substitution of low soluble rare earth elements. But the difference in ionic radii and octahedral site preference of the rare earth elements; it is expected to enhance the magnetocrystalline anisotropy due to alteration in superexchange interactions. Hence a systematic study on magnetic properties of rare earth doped strontium hexaferrite nanoparticles has been carried out in present work.

This thesis reports the work that has been carried out on pure and rare earth elements doped nanoparticles *viz.* $SrFe_{12}O_{19}$ and $SrMe_xFe_{12-x}O_{19}$ (where, Me = La^{3+}, Nd^{3+} and Ce^{3+}).

1.1.5 Objectives

1.1.5.1 Synthesis and characterization of $SrFe_{12}O_{19}$

- To determine the minimum temperature required for the formation of single phase.
- Synthesis of nanoparticles within the single domain size range.
- To study the effect of temperature on various properties, *viz.*
  I. Formation
  II. Structural Properties
  III. Morphological properties
  IV. Magnetic properties

1.1.5.2 Synthesis and characterization of doped $SrFe_{12}O_{19}$: $SrMe_xFe_{12-x}O_{19}$

- $SrLa_xFe_{12-x}O_{19}$ (x = 0.0, 0.23, 0.43, 0.63, 0.83 and 1.0)
- $SrNd_xFe_{12-x}O_{19}$ (x = 0.0, 0.23, 0.43, 0.63, 0.83 and 1.0)
- $SrCe_xFe_{12-x}O_{19}$ (x = 0.0, 0.23, 0.43, 0.63, 0.83 and 1.0)
- To study the effect of temperature and substitution on various properties.

1.2 Magnetism in ferrite

Magnetism is a property of materials by which it response to various substances in the presence and absence of the applied field. Such behaviour of atoms, molecules and solid can be recognized to the orbital and spin motion of the (negatively charged) electrons. When the atoms are fused together to form solid materials, the intrinsic magnetic moment of each atom acts in such a way that the magnetic spin align themself according to their magnetic interactions. The different type of magnetism occurred because every substance have different magnetic behaviour in the magnetic field and therefore, appropriate to classify them into various groups.

1.2.1 Classifications and domain theory of magnetic materials

The magnetic materials can be classified into five different categories on the basis of alignment and relative arrangement of molecule or atoms under the external applied field. The diamagnetic materials have zero magnetic moment because the

valence shells are completely filled and do not have any unpaired electron in outer orbit. These materials are strongly repelled by an applied field. The materials posses small and negative susceptibility (also known as negative magnetism e.g. Copper, Diamond, Antimony, Bismuth, Gold, Mercury, Silver, Tin, Zinc etc. [13]).

The paramagnetic materials posses net magnetic moment due the presence of the single unpaired electron. However, in the absence of applied magnetic field all the magnetic spins are randomly oriented giving rise to zero magnetization. If the paramagnetic materials are placed in the presence of external magnetic field, then magnetic spins tend to align in the direction of applied field and materials acquires net magnetic moments. These materials are magnetic as long as the magnetic field is present; when the magnetic field is removed materials lost their magnetization. Materials have positive susceptibility and follow the Curie's law which predicts that magnetization is inversely proportional to the temperature.

Ferromagnetic materials have very large value of magnetization or permeability and they posses a permanent magnetic moment even in the absence of applied magnetic field. These materials are strongly attracted by a magnet. The exchange interaction among the atomic spins in domains is very strong that make these materials to retain their magnetization even after the removal of magnetic field (Figure 1.3). In a microscopic system, all the spins are aligned along in the same direction. Further the materials system is divided into number of domains and each domain align along the particular direction [13]. These domains result in dilution of energy of the system. However, when the magnetic field is applied, all the boundary domains in a material align along the direction of applied magnetic field that give rise to non-zero magnetic moment. The strontium hexaferrites are ferromagnetic materials in nature. The ferromagnetic materials have a critical temperature above which the material becomes paramagnetic known as the Curie temperature, as result of thermal agitation.

Every magnetic material has critical temperature above which the material becomes paramagnetic. It is well known that the temperature affects the magnetic behaviour of the materials; as the temperature increased in the system, it increases the magnitude of thermal vibrations. Above the Curie temperature, thermal energy is sufficient to overcome the exchange interaction among the atomic moments that

makes these atomic magnetic moment free to rotate anywhere. This is because increase in thermal agitation contracts the coupling force between the adjacent atomic dipole moments, causing some dipole misalignment. The ferromagnetic materials show a spontaneous magnetic behaviour of ferromagnetic materials even in the absence of magnetic field. As seen in case of ferromagnetic materials; when materials are subjected to or placed under the action of external applied field; we observed that if the strength of applied field is small than the alignment of domains are reversible and vice versa for large applied field. For the maximum applied field the material attains the saturation.

On further increase in temperature no other variation has been observed in magnetization. When the applied field is decreased gradually, the value of magnetization is also decreased and follows another path. However, the ferromagnetic material still have the value of magnetization and is known as remanent magnetization. The amount of energy required to reduce the value of magnetization to zero is known as coerecive force. When the field is further increased then the materials again gets saturated along opposite side and a loop has been formed after completing of cycle is known as hysteresis. For the explanation of spontaneous magnetization in ferromagnetic materials, Weiss introduces the concept of domains that the every material is composed of small volume or domain. Below Curie temperature T_C, every material is composed of a region of small-volume; known as magnetic domains and each domain is separated by domain boundaries or wall. The domain walls are generally in the order of $10^{-8} – 10^{-12}$ m^3. The polycrystalline material consists of large number of microscopic domains with different direction of magnetization. In each domain there exist a spontaneous magnetization, whose value depends upon the temperature. The magnitude of the magnetization of the entire material is vector sum of magnetization of all the domains.

1.2.2 Anisotropy: magnetocrystalline anisotropy, stress anisotropy, shape anisotropy

The magnetocrystalline anisotropy is an important characteristic of magnetic materials and is an intrinsic property of a ferro or ferri magnet which is independent of crystallite size and shape.

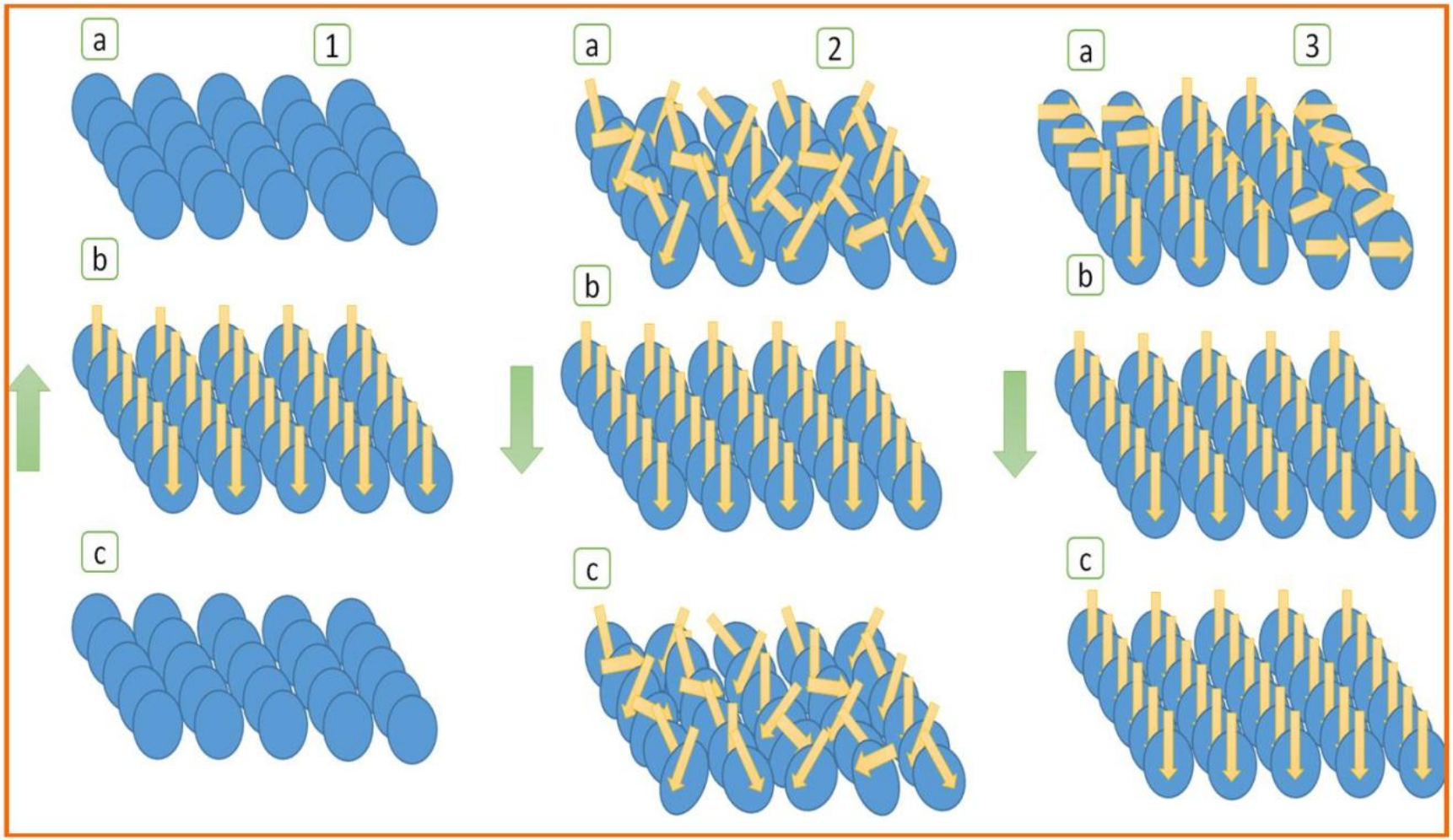

Figure 1.3: (1) Diamagnetic, (2) paramagnetic and (3) ferromagnetic material (a) in the absence of applied field, (b) in the presence of applied field, (c) in the absence of applied field, respectively.

Every crystal has certain direction of preferred orientation in crystallographic axis and is known as easy axes of magnetization. The ferromagnetic materials exhibit both type of magnetic anisotropy *viz.* easy and hard anisotropy or directions of the magnetization. However, the direction of magnetizations in a crystal arises from the interaction of the spin magnetic moment. The strontium hexaferrite is ferromagnetic material in nature and has easy axis of magnetization is along c-axis. It means that nanocrystalites of hexaferrites are easily magnetize along the direction of c-axis or opposite to it. This type of behaviour of any material is known as unidirectional magnetocrystalline anisotropy and the magnetocrystalline anisotropy for single domain nanoparticles has been approximated by Stoner-Wohlfarth single domain theory [14], where energy barrier E_A is also proportional to volume of nanoparticles V under the same magnetization direction. The stress anisotropy (Figure 1.4) in a crystal arises due to change in lattice structure which take place by the means of any deformation or any production of any strain in the system as the strain is found to be a function of applied magnetic field. Therefore, when any ferromagnetic material is placed inside the magnetic field, dimension of the material changes due to the production of strain resulting to shape anisotropy. This is because the strain in a crystal changes the position of atoms inside the materials *i.e.* it affects the exchange interaction energy between the neighbouring atoms. The change in dimension of the magnetic material when magnetized is known as magnetostriction [13,15].

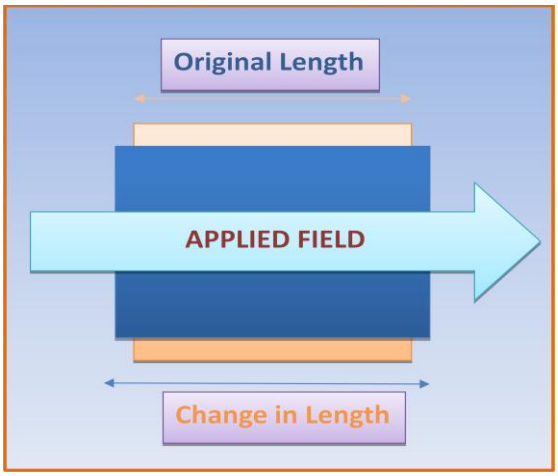

Figure 1.4: Stress anisotropy of material.

1.3 Properties of strontium hexaferrite

1.3.1 Magnetic properties of hexaferrite

The magnetic properties reported for strontium hexaferrite (SrM) are found to be slightly higher than any other M-type ferrite. The saturation magnetization value for single crystal SrM has been reported between 92.6-74.3 A m^2 kg^{-1}. The SrM has comparatively high Curie point 470°C and anisotropy constant 3.5 x 10^6 erg cm^{-3} that result in the formation of high anisotropic material along the c-axis (H_A 1591 kA m^{-1}). This is because SrM ferrite has slightly higher magnetic moment 20.6 μ_B [16]. The saturation magnetization of SrM depends on the magnetic moment and superexchange interaction in the hexagonal ferrites. According to Angeles [18,17], every element has different magnetic moment and has different site preference. This preference not only depends upon the occupation tendency but also on composition and synthesis conditions. If an ion replace the ferric ion from the spin down ($4f_1$ and $4f_2$); then the total number of unpaired electrons in the upward spin are increased and vice versa. It leads to increase or decrease in magnetic saturation values.

Coercivity is the energy or reverse field required to demagnetize the magnetic materials. It has been found that there is some difference in theoretical and experimental value *i.e.* the theoretical coercivity value is 594 kA m^{-1} and experimental value is 159-255 kA m^{-1}, respectively. The coercivity of M-type ferrite is strongly influenced by temperature and size of the particles. There is lot of confusion and disagreement for critical domain range (experimental estimated value is 1.8 μm), whereas according to Kittle theory the critical domain range lies between 0.3-0.9 μm. Craik et al. 1977 have found that the coercivity value increases with a decrease in grain size, especially when the size of particle is in single domain size [19]. The nanoparticles of hexaferrite prepared by standard ceramic route in the temperature range 1100°C and 1350°C indicates the decrease in coercivity value, where the size of the particles in micrometer range (increases from 0.5 micro meter to several micrometer). This decrease in H_C value with calcination temperature indicates the direct relationship between grain size and coercivity *i.e.* larger the grain size, lower the coercivity values [20]. The magnetic material having

coercivity above 600 Oe can be useful in longitudinal magnetic recording media devices while if the coercivity is too high (1200 Oe), the material can be used for perpendicular recording media which is a developing new technology in the magnetic recording materials. Most important factor in storage media is the remanence value which designates the quality and performance of any media [17]. High the remanence value in a material keeps the information for longer time and vice versa.

1.3.2 Chemical, thermal and mechanical properties of hexaferrite

The chemical property of the ferrites strongly depends upon their composition and synthesis technique. These materials are found to be stable up to some extent in week acids such as CH_3COOH, citric acid and phenol solutions, but are unstable in strong acids *i.e.* HCl, HNO_3, H_2SO_4 and H_3PO_4 [17]. Thermal properties are important part for the crystallization. This is because during the synthesis process proper thermal calcination is necessary for crystallization process. If high crystallization temperature or time is applied, it may alter the properties of nanoparticles (especially crystallite size). The knowledge of thermal parameters such as activation energy gives an idea for the synthesis temperature. The knowledge of calcination temperature allows us to control the grain size to obtain the desired properties [21]. Tyagi et al. (2010) have calculated the activation energy for the strontium hexaferrite and found to be 168.33 KJ/mole [22]. The other thermal parameters such as thermal conductivity, diffusivity and heat capacity which are strongly influenced by impurities, temperature, pressure, lattice imperfection and porosity are found to be 2.69 Wm^{-1} K^{-1}, 1.132 mm^2 S^{-1} and 2.73 MJ m^{-3} K^{-1}, respectively [17]. Also ferrites are high melting point materials (1390°C) having Curie temperature above 450°C with maximum density 5.101 g/cm^3 (for SrM). Hardness, tensile strength, flexural strength and critical stress intensity factors are the basic parameters of mechanical property. The mechanical properties give the reliable information about quality of hexaferrite materials. The calculated value of hardness for hexaferrite has been found to be 5.9 GPa in the c-axis, whereas measured value is 6.0

GPa. The flexural strength for strontium hexaferrite was found to be 86.3 ± 7.8 N mm^{-2} [23], when the sample was placed perpendicular to c-axis.

1.4 Synthesis techniques

Solid state technique is widely used technique to prepare the hexagonal ferrite traditionally in early days. The nanocrystalline hexaferrite particles have been synthesized using a mixture of starting materials of iron oxide and metal carbonates at temperatures above 1000°C. This is because the crystallization of ferrite does not occur at room or low temperature. However, the firing of starting material at such high temperature leads the formation of uncontrollable crystal or particles which results in dilution in various properties such as structural, electrical, dielectric and magnetic properties. Steier et al. [24] have investigated the formation of hexaferrite from the stoichiometric mixtures of $BaCO_3$–Fe_2O_3. They found that the ferrite phase has been observed when the system is calcinated between 700°C to 900°C and below it, intermediate phases have been observed. However, Dursun S. et al. [25] have tried to solve the problem of uncontrollable particle size in solid state reaction by ball milling technique. They used similar solid state method with same starting materials. But they also made some variation in synthesis process where the starting materials were milled in isopropanol using zirconia balls in high density polyethylene bottle for 24h. The isopropanol was evaporated using magnetic stirrer to eliminate differential powder settling. The precursor product was calcinated at 1100°C for 6h to obtain single phase. Here, although the powder was calcinated at high temperature that still leads the formation of large grain size particle. Now the calcinated powders were again ball-milled for 24h using ZrO_2 balls in isopropyl alcohol to reduce particle size. The solid state method seems to be typical technique to obtain ferrimagnetic hexagonal oxides particles due to the calcination of particles at higher temperature and longer durations resulting to large particle size and low limited chemical homogeneity [26]. Benito et al. 2001 [27] have used ceramic method for the production of hexaferrite nanoparticles at lower temperature in order to avoid all problems (crystallite size, morphology, magnetic

parameters, etc.). A ceramic technique involves the mixing of oxide and carbonate powders at the atomic or ionic level before reaction. It produce the ferrite phase in one step (rather than multi step like solid state reaction) using ceramic technique, but this can be achieved only with the help of high energy mechanochemical milling. The coprecipitation is another chemical route which has been used since 1960s for the synthesis of nanoparticles. Lot of research has been done in order to improve the homogeneity of the particles through this route. Lisjak et al. 2007 [28] have investigated the formation of strontium hexaferrite from metal nitrates and chlorides in water or an enthanol solution using co-precipitation in order to elucidate the low temperature for formation. They have proved that the crystallization reaction takes place in two competing process; (i) directly from amorphous precursor and (ii) indirectly via crystalline intermediates. Structural analysis confirms that the lower Fe:Sr (or Ba) ratio and low calcination temperature is required to produce pure strontium hexaferrite. The mixture of metal salts and base was autoclaved under pressure for the ferrite formation and is known as hydrothermal synthesis. Hydrothermal method employed expensive autoclaves, requires good quality seeds of fair size, and does not allow observation of the crystal as it grows [26]. Also this technique still have some limitation even after the mixing of starting materials at ionic levels in autoclave process because it has been observed that the presence of number and strength of secondary phases is more comparative to other techniques. The existence of secondary phase in the precursor powder means that the system needs more care during the synthesis. Salt melt method involves the reactions of metal chlorides which are co-precipitated by by NaOH, Na_2CO_3 or $NaHCO_3$. The salts of sodium chloride and potassium chloride have been added to the mixture of metal chlorides finally heated to a flux between 600 and 1100°C. The possibility of the presence of sodium and potassium salt cannot be ruled out and can be removed from ferrite product by washing with distilled water. Hexaferrite with desired magnetic properties has been synthesised with this method in a non-stoichiometric mixture with Fe:Ba ratio of 10. The grain size and magnetic properties can be varied by changing the compositions of the fluxing components [16,29]. Low-temperature

combustion technique takes long time for the self-ignition reaction to occur and needs cationic surfactants to remove impurities such as hematite [30,31]; whereas mechanical alloying process leads to (impurities) the formation of secondary phase and lattice strains [26,32]. The present investigation deals with the synthesis of pure and rare earth elements doped strontium hexaferrite nanoparticles by citrate precursor method. Among the synthesis methods, this method is appears to be simple, economical and convenient for mass production of fine grained ferrite powders. This method of preparation method gradually gaining importance because it neither it requires expensive chemicals nor equipment like autoclaves for hydrothermal process. On the other hand, the synthesised nanomaterials exhibit high purity, chemical homogeneity, controlled crystallite size as well as defined morphology with optimum properties.

1.5 Literature review

Jin et al. (1998) have prepared strontium hexaferrite (M-type) fine particles by mechanical alloying. The synthesized particles have been characterized for structural, morphological and magnetic analysis by XRD, SEM and VSM, respectively. The effects of milling conditions on magnetic properties of $SrFe_{12}O_{19}$ compounds have been studied. Its clear from heat treatment that temperature plays an important role in structural transformation as compared with long time milling process. The result reveals that the saturation value is more sensitive than coercivity for sample which is annealed at 750-800°C [33]. Ebrahimi et al. (2000) have prepared hexaferrite nanoparticles conventionally [34]. The synthesized particles are heated in hydrogen atmosphere and subsequently calcinated in air. The structural analysis shows the decomposition of strontium hexaferrite into Fe_2O_3 and $Sr_7Fe_{10}O_{22}$. It has been observed that during the hydrogenation process, there is an increase in magnetization while intrinsic coercivity found to be decrease. This can be attributed to the formation of α-Fe phase. Significant improvement in the coercivity has been achieved in the synthesized material after the re-calcination. The highest intrinsic coercivity obtained in this work was 400 kA/m (5 kOe) which occurred after hydrogenation at 700°C for 1h under an initial pressure of 1.3 bar

followed by re-calcination at 1000°C for 1h. This was attributed mainly to very fine grains formed as a result of hydrogenation and subsequent re-calcination. The chemical sol–gel route has been employed by Fang et al. (2001) to prepare hexaferrite nanoparticles [35]. The magnetic study on the basis of heat treatment of the gel and iron/ strontium ratio in the starting solution has been carried out. Result reveals that the sample synthesized between 400°C and 500°C for several hours is significant for optimum conditions. $(Zn, Ti)_x$ substituted strontium ferrite have higher values of both coercive field strength and saturation magnetization than that of $(Zn, Ir)_x$ substituted strontium ferrite. The electrical transport properties of erbium substituted Ni–Zn ferrites of various compositions from room temperature to well beyond the Curie temperature have been investigated by Kumar et al. (2001) [36]. The plot for electrical conductivity i.e. log (σT) versus $10^3/T$ are found to be linear and show a transition near the Curie temperature. An attempt was made also to explain the conduction mechanism in these ferrites. The Seebeack coefficient calculated for synthesized material on that basis materials are classified as *n* type semiconductors. The properties of gadolinium substituted Ni–Zn ferrites have been correlated with these of erbium substituted Ni–Zn ferrites. Sileo et al. (2002) have prepared nickel zinc ferrite ($Ni_{1-x}Zn_xFe_2O_4$) and their derivatives (x = 0.2, 0.4, 0.5, 0.6 and 0.7) by a combustion method. XRD analysis indicates that after combustion the gel is directly transformed into single phased nanoparticles [37]. The crystallinity and domain size of the particles are found to increase with sintering processes. Wang et al. (2002) have synthesized ultrafine powders of Z-type hexaferrite $Ba_3Co_2Fe_{24}O_{41}$ denoted herein as a Co_2Z by citrate precursor method and characterized by X-ray diffraction and VSM [38]. Z-type hexaferrite ceramics have been sintered below 900^0C and microstructures as well as high frequency characteristics have been studied. The results show that the magnetic properties were much influenced by the amount of sintering aids and sintering temperatures. Singh et al. (2003) have used the citrate precursor method for the synthesis of $Mn_xNi_{0.5-x}Zn_{0.5}Fe_2O_4$, ($x$ = 0.05, 0.1, 0.2, 0.3, 0.4) ferrites [39]. The effect of composition and synthesis process on electrical resistivity has been investigated. It was found that resistivity decreases with increase in

Mn concentration except for $x = 0.3$ (where it shows a rise). Soft $Mn_{0.4}Zn_{0.6}Fe_2O_4$ ferrites have been prepared by a wet chemical process using metal nitrate solution through citrate precursor method by Thakur et al. (2003) [40]. The electrical and magnetic measurements on Mn–Zn ferrite indicates that these ferrites especially suitable for high frequency applications due to high electrical resistivity and low magnetic loss. The smaller grain size and homogeneity in grains leads the enhancement in saturation magnetization, initial permeability and Curie temperature. The nanowires of $SrFe_{12}O_{19}$ with diameters of 100 nm and lengths of 2.5 mm have been prepared by Wang et al. in 2004 in a hydrothermal cell at 180°C with an 0.35T applied magnetic field [41]. The transmission electron microscope observations shows that the morphology of the particles changed from flake-like (in zero magnetic field) into nanowires in a magnetic field. Sivakumar et al. (2004) have synthesized a fine strontium hexaferrite powder by a sonochemical method employing $Fe(CO)_5$ and $SrCO_3$. $SrCO_3$ was first synthesized using strontium nitrate and urea, and it was found that applying ultrasound radiation during this process results in the uniform formation of $SrCO_3$ hexagonal rods [42]. These rods were then dispersed with in situ generated amorphous Fe_2O_3, using $Fe(CO)_5$ as the source. The resultant precursor was then calcinated at 900°C, which is lower than the conventional solid-state reaction of applying 1300°C to get the strontium hexaferrite fine powder. Lechevallier et al. (2005) have made significant improvements of the magnetic properties of M-type hexaferrites by substituting of rare-earth element (Sm^{3+}, Nd^{3+} or La^{3+}) in the Sr^{2+} site, and the substitution of a metal ion (Co^{2+} or Zn^{2+}) in the Fe^{3+} sites [43]. The presence of secondary phases have been analyzed with the help of XRD whereas the location of the substituted elements has been determined with the help of ^{57}Fe Mossbauer spectrometry. Verma et al. (2005) have prepared nickel zinc ferrite $Ni_{1-x}Zn_xFe_2O_4$ (x = 0.2, 0.35, 0.5 and 0.6), by the citrate precursor technique and temperature dependence of resistivity, dielectric constant and dielectric loss have been investigated for four different compositions of nickel–zinc ferrites [44]. The sample having composition $x = 0.6$ show low dielectric losses up to a measurement temperature of around 200^0C at higher frequencies as compared to samples of other compositions. Cu substituted Ni Zn ferrite has been

prepared using the citrate precursor method by Dimri et al. (2006) [45]. The synthesized powders were calcinated at 600^0C for the duration of 1h and then sintered at 900^0C for 3h to obtain desired properties. The effect of composition on structural, dielectric and magnetic properties of $Ni_{0.6-x}Cu_xZn_{0.4}Fe_2O_4$ (where $0 \leq x \leq 0.4$) particles was investigated. X-ray diffraction measurements confirmed the formation of single-phase cubic spinel structure at such low temperature. The addition of copper results in grain growth, and composition $x = 0.2$ shows 92 emu/g saturation magnetization value. The effect of the surfactant on the crystallite size of the final product has investigated for the first time by Alamolhoda et al. (2006) [46]. The thermal analysis shows the formation temperature of hexaferrite. The XRD results show that adding surfactant to the sol does not change the composition of the combustion product and the surfactant burns completely during the combustion process. The addition of surfactant into the gel results in the reduction of crystallite size. The structural and magnetic properties of $SrFe_{12-x}R_xO_{19}$ (R = La, Gd and Er; $x = 0.2$, 0.5 and 1) powders heat treated at 800°C, 900°C and 1000°C, for various times, have been characterized with X-ray diffractometer, vibrating sample magnetometer and scanning electron microscope. Doroftei (2006) have used sol-gel autocombustion method for the preparation of rare-earth substituted strontium ferrite nanopowders [47]. The structural analysis confirms the formation of M-type hexagonal structure by different heat treatments. The heat treatment conditions such as temperature and time affects the magnetic parameters as well as microstructure. Shirtcliffe et al. (2007) have synthesized aluminium doped strontium and barium ($SrAl_xFe_{12-x}O_{19}$ and $BaAl_xFe_{12-x}O_{19}$) hexaferrite nanoparticles *via* a sol-gel route using citric acid to complex the ions followed by an auto-combustion reaction [48]. XRD, TEM, SEM/EDX have been used for the investigation. Samples were prepared by sonicating the particles in ethanol for 1h and placing drops of the suspension onto carbon-coated copper TEM grids before allowing them to in the air. The results indicate the increasing aluminium content affects the morphology of the particles. The effect of Gd substitution in M-type strontium hexaferrites i.e. $(Sr_{1-x}Gd_x)O_{5.25}$ Fe_2O_3 and $Sr_{1-x}Gd_xFe_{12-x}Co_xO_{19}$ (where x = 0-0.4) has been systematically investigate by Litsardakis et al. (2007) [49]. The plating process has

been studied by Pan et al. (2007) [50]. The Co–Ni–P coated strontium ferrite nanocomposites have been prepared by electroless plating enhanced by ultrasonic wave at room temperature. The morphology, crystal structure and microwave absorption properties of the Co–Ni–P coated powder have been analysised with field emission scanning electron microscopy (FE-SEM), X-ray diffraction (XRD), energy dispersive analysis of X-rays (EDX) and vector network analyzer. The results reveal that the strontium ferrite powder has been successfully coated with Co–Ni–P alloy. Powders of sample $SrFe_9(Mn_{0.5}Co_{0.5}Zr)_{3/2}O_{19}$ synthesized from sol–gel method show a hexagonal fine platelet structure and narrow particle size distribution, Ghasemi et al. (2008) [51]. Zr–Cu doped strontium hexaferrite nanoparticles have been prepared by Iqbal et al. (2008) using chemical co-precipitation method [52]. The electrical results show the semiconductor-metal transition behavior for $SrZr_xCu_xFe_{12-2x}O_{19}$ (where x = 0.0–0.8) at a temperature T_{M-S}. The crystallite size estimated by Scherrer formula (26–37 nm) and the Curie temperature (T_C) of the sample found to be decreases with the increase in Zr–Cu concentration. Soibam et al. (2009) have prepared lithium zinc ferrites having the general formula $Li_{0.5-0.5x}Zn_xFe_{2.5-0.5x}O_4$ where $0 \leq x \leq 0.6$ in steps of 0.2 by the citrate precursor method [53]. The sample characterizations have been carried out with the help of XRD and LCR-meter. Results show that the Curie temperature decrease with increasing Zn concentration and permeability found to be increase with the increase in the concentration of zinc. Costa et al. (2009) have reported the preparation of Ni–Zn–Sm ferrite powders by combustion reaction [54]. The mixture of metal nitrates and fuels (urea, glycine or 1:1 mixture) have been used to obtain high crystalline nanoparticles, where the mixture was heated in microwave oven for 5 and 10 min using the power of 450 and 630W. Jacobo et al. (2009) have prepared strontium hexaferrite samples ($SrFe_{12}O_{19}$ (S0), $Sr_{0.7}Nd_{0.3}Fe_{11.7}Co_{0.3}O_{19}$ (SS), $Sr_{0.7}Nd_{0.3}Fe_{10.7}Co_{0.3}O_{19}$ (SM) and $Sr_{0.7}Nd_{0.3}Fe_{8.4}Co_{0.3}O_{19}$ (SL)) of different composition by the self-combustion method and heat-treated in air at 1100°C for 2h [55]. The phase identification of the powders was performed using XRD. Only sample SL (with the lowest iron concentration) shows well-defined peaks of the hexaferrite phase with no secondary phases. Nd–Co substitution modifies saturation

magnetization (M_S) and coercivity (H_C) but only samples with low Fe^{3+} content (SL and SM) show the best magnetic properties, indicating that the best results for applications of this ferrite will be obtained with an iron deficiency in the stoichiometric formulation. Raghavender et al. (2010) have prepared $NiFe_2O_4$ nanoparticles having 29 to 50 nm sizes using sol gel auto-ignition method [56]. The analysis has been carried out *via* X-ray diffraction, Fourier transform infrared spectroscopy and VSM. The IR spectra show the absorption bands corresponding to stretching vibrations of tetrahedral and octahedral bonds which confirm the formation of spinel phase. The polycrystalline samples of U-type hexaferrite series: $Ba_4Co_{2-x}Mn_xFe_{36}O_{60}$, with x varying from 0 to 2.0 in steps of 0.5, through conventional solid state reaction route in order to develop a new microwave absorbing material over the X-band (8.2–12.4 GHz) frequency range. The variation of electromagnetic parameters and microwave absorbing properties were studied over the X-band frequency range with varying composition. Both dielectric loss and magnetic loss were found to decrease with increasing x, whereas the dielectric constant and magnetic permeability variations are reciprocal with Mn addition, Meena et al. (2010) [57]. The synthesis and characterization of Nd–Ni doped strontium–barium hexaferrite nanomaterials: $Sr_{0.5}Ba_{0.5-x}Nd_xFe_{12-y}Ni_yO_{19}$ (x = 0.00–0.10; y = 0.00–1.00) have been systematically investigated by Iqbal et al. 2011 [58]. Structural analysis inferred that the lattice parameters and cell volume are inversely related to the dopant content. A temperature dependent DC-electrical resistivity measurement shows the decreasing behaviour of resistivity for strontium–barium hexaferrites from 1.8 $x10^{10}$ to 2.0 x 10^8 ohm cm. Single-phase M-type strontium hexaferrites $Sr_{1-x}Nd_xFe_{12-x}Co_xO_{19}$ (x = 0–0.3), have been formed by being heated at 1200°C for 3h in air (Zhang et al. 2012) [59]. Crystalline structure, morphology, magnetic properties, and microwave absorption properties of synthesised nanoparticles have been studied *via* X-ray diffraction, scanning electron microscope, vibrating sample magnetometer, and vector network analyzer, respectively. Saturation magnetization and coercivity found to be maximum at x = 0.2. M-type barium hexaferrites $Ba_{1-x}Ce_xFe_{12-x}Co_xO_{19}$ ($0.0 \leq x \leq 0.3$) [60] have been synthesized by a simple chemical co-precipitation method in 2012 by Zi et al. X-ray

diffraction studies indicate that the samples are of single phase. The results of field-emission scanning electronic microscopy (FE-SEM) show that the grains are regular hexagonal platelets with sizes from 0.5 to 1.5 μm. It is observed that the value of the coercivity field (H_C) increases at low substitution ($x \leq 0.1$), reaches a maximum at $x = 0.1$, and then decreases at $x \geq 0.1$, while the value of saturation magnetization (M_S) decreases monotonically with increasing x. The variations of magnetic properties can be explained on the basis of substitutional effects of Ce–Co. Chang et al. 2012 have prepared Ce-substituted barium ferrite with chemical composition $BaCe_{0.05}Fe_{11.95}O_{19}$ by the citrate sol–gel method [61]. $Ba_{(1-x)}La_xFe_{12}O_{19}$ ($0.00 \leq x \leq 0.10$) nanofibers have been fabricated by Li et al. 2012 using electrospinning technique followed by heat treatment at different temperatures for 2h [62]. Various characterization methods including scanning electron microscopy, X-ray diffraction, vibrating sample magnetometer, and microwave vector network analyzer were employed to investigate the morphologies, crystalline phases, magnetic properties, and complex electromagnetic parameters of nanofibers. The SEM images indicate that samples with various values of x are of a continuous fiber-like morphology with an average diameter of 110 nm. The VSM results show that coercive force (H_C) decreases first and then increases, while saturation magnetization (M_S) reveals an increase at first and then decreases with La^{3+} ions content increase.

1.6 Applications of ferrite materials

The growing market of magnetic materials for motor, generators, transformers, actuators and sensors, information storage, magnetic recording, transport, security, defence and aerospace and diagnostic devices; the hexaferrites are getting importance due to their low cost and their tremendous electrical and magnetic properties than any other magnetic materials. The most commonly used magnetic materials for the scientific and technological applications are ferromagnetic and alloys or ferrimagnetic ceramics. The use of any material for any particular function depends upon number of physical and economical factors. The alloys of rare earth elements are believed to be permanent magnet of best quality. But the problem is the scarcity and major part of rare earth

element (RE) comes from China. China has decided to decrease the export of raw materials and started to sell manufactured magnets directly in the market [63]. It causes the disturbance in the market resulting increase in price of rare earth magnets. To overcome this problem researchers focus their mind on the synthesis of hexaferrite for magnetic applications. Permanent magnet prepared from hard magnetic ferrite are not so good in comparison to magnet prepared from alloys of RE. But subsequently it overcome the problem of cost and scarcity. That's why the ferrites are widely used than any other permanent magnetic materials. As well as the increasing growth of electrical and microwave devices that are working at higher frequency range in industry, commercial and military such as radar, wireless and mobile communication causes the electromagnetic interference (EMI) problems. Presently, our whole world is covered with the electromagnetic waves which are creating problem to human society (biological tissues). To overcome this problem, electromagnetic absorbing materials have come in to existence. The hard magnetic materials work as a dielectric or magnetic filler. This is because ferrite materials have perfect dielectric and microwave properties like permeability, permittivity and high dielectric constant. The spinel ferrites are already used as EM absorbing materials but due to lack of response at higher frequency, hexaferrite have replaced them from market. The one major problem with ferrite materials occurs when we are working in the microwave frequency range we require low dielectric loss. This can be achieved only when material is perfect insulator. The ferrite materials are not a good insulator. This problem can be eliminated by fabricating ferrite powder on a superconducting substrate or composite in a non-conductive matrix. To meet the requirements or demands lot of alteration have been done in their properties, by substitution of different cations in basic structure. Recently, the composites of ferrite have come in existence for high absorption. The plastoferrites are composites of magnetic materials in which ferrite powder is mixed with a thermoplastic matrix. However, the plastoferrite leads the dilution in various properties such as magnetic properties etc, but results in aggregation of particles that enhance the microwave or dielectric behaviour due to less porosity. Plastoferrite are hard in nature; neither brittle and nor fragile. The most

common example of plastoferrite is refrigerator door magnets. Ferrites are also used to shield rooms and chambers used for the testing of new devices operating in microwave frequencies. These materials are also coated on military aircraft for stealth operation or reduction of radar signatures *i.e.* in stealth technology. The ferrites are applicable for many appliances (such as loudspeakers, microphones, TV picture tube ion traps and most widely in D.C. motors in portable electric motors) due to their response both in low and high frequency. Soft ferrites are very useful in low frequency range due to low electrical loss and high resistivity. But these materials are not useful where we have to transmit electrical energy in high frequency range through wire. The hard ferrites mainly operate at high frequencies as permanent magnets and help to reduce high frequency noise in dc circuit. Also the hard ferrite materials have high electrical resistivity that decreases the tendency for the production of induced current within the materials results in loss of energy in the form of heat. Considering all the properties and applications of strontium hexaferrites, this thesis aims for the synthesis and characterization of different strontium hexaferrites doped with rare earth elements. Thesis is divided into seven chapters including this chapter and last chapter as summary.

CHAPTER II

Synthesis and Experimental Techniques

2.1 Synthesis of strontium hexaferrite

This chapter describes the preparation and characterization techniques for the synthesis of strontium $SrFe_{12}O_{19}$ and $SrMe_xFe_{12-x}O_{19}$ (where, Me = La^{3+}, Nd^{3+} and Ce^{3+}; x = 0.0, 0.23, 0.43, 0.63, 0.83 and 1.0).

2.1.1 Chemicals required for synthesis of $SrFe_{12}O_{19}$ and $SrMe_xFe_{12-x}O_{19}$ samples are:

I. Strontium nitrate $Sr(NO_3)_2$ (Merck, 99.9%), lanthanum nitrate hexahydrate $La(NO_3)_3.6H_2O$ (CDH, 99.9%), cerium nitrate hexahydrate $Ce(NO_3)_3.6H_2O$ (CDH, 99.9%), neodymium nitrate hexahydrate $Nd(NO_3)_3.6H_2O$ (CDH, 99.9%), and Ferric nitrate nonahydrate $Fe(NO_3)_3.9H_2O$ (CDH, 99.9%).

II. Citric acid monohydrate $C_6H_8O_7.H_2O$ (Merck, 99.9%).

III. Aqueous ammonia (25%) AR-grade was taken as pH controller (Merck, 99.9%).

2.1.2 Steps involved in sample preparation are given below:

I. Aqueous solution of metal nitrates was prepared separately in stoichiometric proportion by dissolving the salts in distilled water.

II. Aqueous solution of citric acid was added to the salt solution with cation to citric acid molar ratio of 1:1.5.

III. Aqueous ammonia is then added drop wise to adjust the required pH value of 6-7 the solution.

IV. The solution was then heated at 80-85°C, with continuous stirring for several hour with the help of magnetic stirrer.

V. The solution is then heated on a hot plate at 180-230°C to form a dried precursor powder.

VI. The precursor powder was further dried in muffle furnace at deferent temperature to form fine dried precursor powder.

VII. Sample prepared after calcination are crushed in mortar pestle to get powder for characterization.

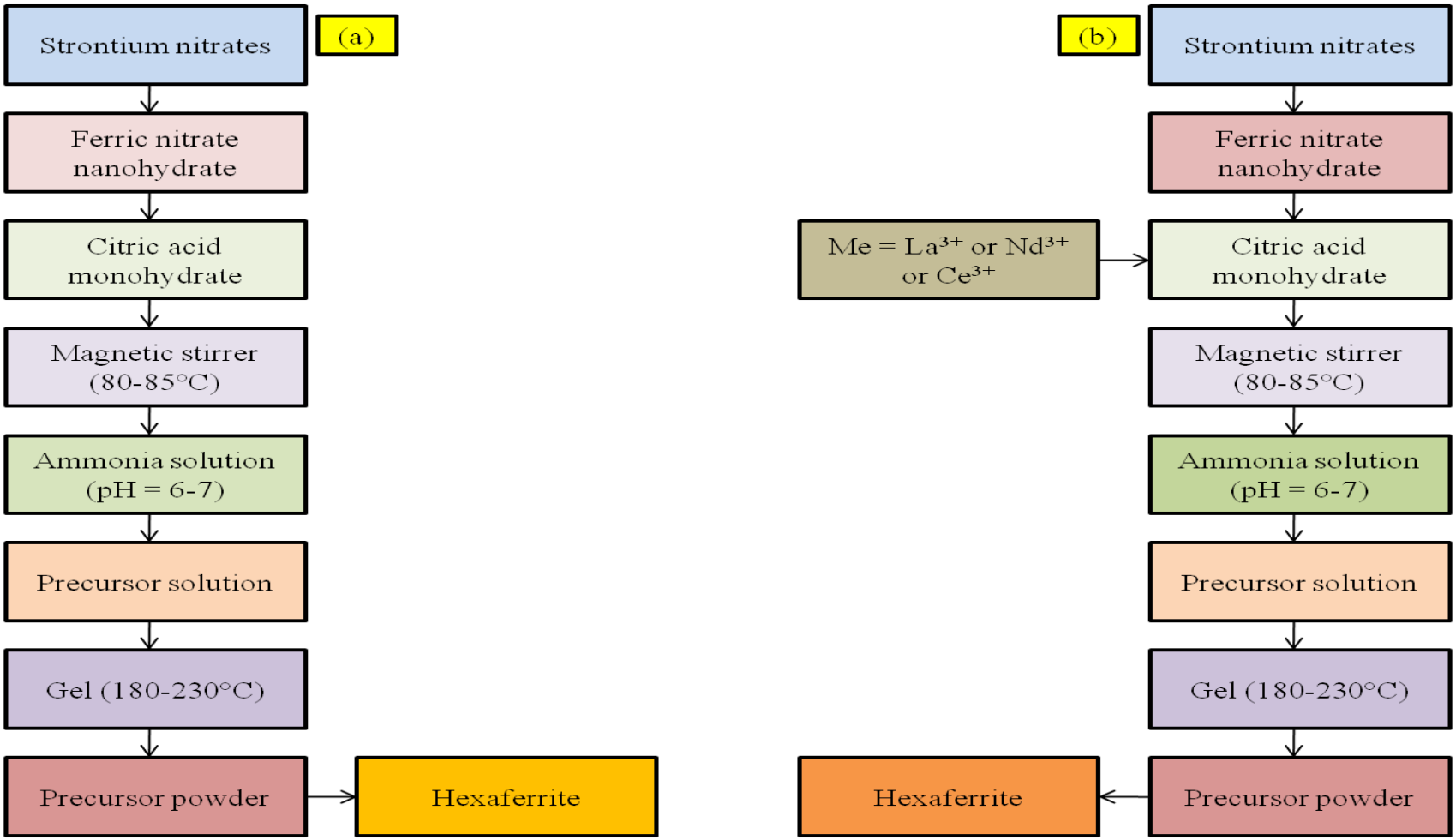

Figure 2.1: Flow chart of synthesis of (a) $SrFe_{12}O_{19}$ and (b) $SrMe_xFe_{12-x}O_{19}$ (where, Me = La^{3+}, Nd^{3+} and Ce^{3+}; x = 0.0, 0.23, 0.43, 0.63, 0.83 and 1.0).

VIII. For synthesis of doped strontium ferrite similar steps have been followed except the addition of corresponding dopant. It has been systematically described in Figure 2.1b.

2.1.3 Chemical mechanism occurs in sol

This can be explained on basis of crystal structure and ionization of the citric acid, which is composed of three carboxyl groups and one hydroxyl group. The crystallization of nanoparticles is depends upon the nature of chemical species and strongly influenced by presence of metal ions, chelating agent as well as pH of the solution. In Sr^{2+}/Fe^{3+} -citric acid system, the citric acid is not able to make complexes with the metal ions in highly acidic medium, but as the pH of solution is increased, it results in the ionization of citric acid above pH 3 and start complexation with metal ions. The different complex ions of Sr^{2+}or Fe^{3+} -citrate system have been formed according to pH of the solution. The optimum pH for the formation of pure Sr^{2+}-citrate complex ions is greater than 4, whereas the formation of pure Fe^{3+} -citrate complex is less than 7.5. Therefore, the 6-7 is the optimum pH for the simultaneous formation of stoichiometric citrate complexes of same metal ions in a solution to avoid precipitation. Still the existence of magnetic phase can be attributed to the ability of transition metal ions to form metal-citrate complexes over wide pH range that leads to the formation of ferrite nanoparticles with low crystallinity even in highly acidic medium. Moreover, more than one metal ion can able to complexed with a single citric ion at the optimum pH. After sol formation the matrix left for gelation for 5-10 hours depending upon the amount of sol.

2.1.4 Sol-Gel method and its significance

A sol is a liquid and a gel consists of a three dimensional continuous network, which encloses solid nanoparticles dispersed in a liquid (a sol) agglomerate together to form a continuous three-dimensional network extending throughout the liquid (a gel). The sol-gel is process, involves the evolution of inorganic networks through the

formation of a colloidal suspension (sol) and gelation of the sol to form a network in a continuous liquid phase (gel).

- The basic idea behind the sol-gel process is to dissolve the compound in a liquid in order to bring it back as a solid in a controlled manner.
- Multi component compounds can be easily synthesized with a controlled stoichiometry by mixing sols of different compounds.
- Mixing of metal ions at an atomic level enables the formation of homogenous particles and also prevents the problem of co-precipitation.
- Results in small particles, which are easily sinterable.

2.1.5 Sol-Gel method can be characterized by a series of distinct steps

- **Step 1:** Preparation of sol from deferent metal precursors.
- **Step 2:** Formation of the gel by a polycondensation or polyesterification reaction due to the development of an oxide- or alcohol- bridged network which results in a dramatic increase in the viscocity of the solution and generally known as gelation.
- **Step 3:** During the aging of the gel (Syneresis), gel has been transformed into a solid mass, accompanied by contraction of the gel network and expulsion of solvent from gel pores. Also, Ostwald ripening (where smaller particles are consumed by larger particles during the growth process) and phase transformations may occur concurrently with syneresis process.
- **Step 4:** Drying of the gel is a complicated process due to the occurrence of fundamental changes in the structure of the gel during the removal of water and other volatile liquids from the gel network.
- **Step 5:** Formation of particles and densification of the gel has been achieved at high temperature where pores of the gel networks are collapsed and remaining organic species are volatilized.

2.1.6 Factors that affect sol-gel process

Sol-gel process particularly sensitive to the following parameters

- **pH:** Inorganic materials that involve water are sensitive to pH of sols.
- **Solvent:** Play a vital role during the chemical reaction, it helps to dissolve the solute in proper manner.
- **Temperature:** The reaction kinetics for the formation of the nanoparticles has been strongly influenced by temperature. This is because, if the temperature is too high, the reactions that join nanoparticles together into the gel network occurs so quickly that clumps form instead and solid precipitates out of the liquid.
- **Reaction-generated heat:** Heat released during any chemical reaction which involved in the formation of nanoparticles cause things to react faster and releasing even more heat.
- **Time:** Slower time is better for sol-gel means if you allow to gel, for slow process the uniform structure has been obtained. This also increases in the quality and strength of gel.
- **Catalysts:** Catalyst is an agent that accelerates the chemical reactions. Acids (H^+) and bases (OH^-), both are acts as catalysts that effect the chemical reaction according to their means. Even small quantity of catalysts shows drastic changes in gel formation time from days to weeks or minutes. This is another reason why sol-gel chemistry is usually pH sensitive.
- **Agitation:** Mixing of metal ions with each other is an important step to ensure that the chemical species are uniformly distributed in the solution. This can be done by keep the solution on the stirrer to achieve agitation.
- The Rest Depends on the **Recipe!**

2.1.7 Formation of precursor powder from gel

$$Gel \xrightarrow{200^{o}C} \gamma - Fe_2O_3 + SrO + NH_4NO_3 + CO_2 \uparrow$$

$$SrO + CO_2 \xrightarrow{200\text{–}500^{o}C} SrCO_3$$

$$SrCO_3 + 2\gamma - Fe_2O_3 \xrightarrow{500\text{–}700^{o}C} SrFe_2O_4$$

$$SrFe_2O_4 + 5\gamma - Fe_2O_3 \xrightarrow{800\text{–}1200^{\circ}C} SrFe_{12}O_{19}$$

Unlike spinel ferrites, the formation of hexaferrite does not takes place in single step, it formed gradually from some intermediate phases due to its complicated crystalline structure. Where, the interaction between free Sr^{2+} ions and CO or CO_2 generated from the decomposition of citric acid, leads to the formation of SrO and then $SrCO_3$. When the calcination temperature is increased to 500°C, $SrCO_3$ decomposes and Sr^{2+} liberated reacts with γ-or α-Fe_2O_3 to form a small amount of monoferrite $SrFe_2O_4$. The reaction between monoferrite and iron oxide (γ-or α-Fe_2O_3) leads to formation of strontium hexaferrite. The amount of strontium hexaferrite increases monotonically with the increase in temperature and appears as a major phase at 800-1200°C. Above reactions can also be written as

$$Sr(NO_3)_2 + 12\ Fe(NO_3)_3.9H_2O + C_6H_8O_7.H_2O + NH_4OH \rightarrow SrFe_{12}O_{19} + NH_4NO_3 + CO_2 + H_2O \ (\textbf{For pure } \mathbf{SrFe_{12}O_{19}})$$

$$Sr(NO_3)_2 + (12\text{-}x)\ Fe(NO_3)_3.9H_2O + x\ Me\ (NO_3)_3.6H_2O + C_6H_8O_7.H_2O + NH_4OH \downarrow SrMe_xFe_{12-x}O_{19} + NH_4NO_3 + CO_2 + H_2O \ (\textbf{For doped } \mathbf{SrFe_{12}O_{19}})$$

2.2 Characterization Techniques

2.2.1 Thermal analysis (DTA/DTG/TG)

Thermal analysis enables to measure or identify the response of the specimen including heat transfer and change in mass against the time and temperature. Basically, the thermal analysis has been done using differential thermal analysis (DTA) to study all type of physical and chemical changes that are related to heating and cooling as shown in Figure 2.2. These are basic thermoanalytic methods which are concerned with heat change in the sample during chemical reactions. The specimen and reference sample are kept in an identical atmosphere or thermal environment (in DTA). The difference between the temperature of specimen and reference sample as a function of time (or temperature) has been measured which provides the useful information regarding the kinetics behavior of

reactions. The phase change in the sample relative to the reference has been occurred in two ways either of exothermic or endothermic. In other words, the exothermic reaction means the system is releasing some amount of energy during crystallization process. The DTA instrument consists of thermocouples, furnace, digital recording system, sample containers (Figure 2.3). The sample containers are made up of Al_2O_3. The sample with appropriate quantity has been placed in sample container w.r.t to reference container. Both the containers are connected through thermocouple via voltmeter. When the temperature of specimen is increased in comparison to reference sample during the phase transformation, voltmeter gives some deflection. This changes (or deflection) in the sample during phase transformation; whether it is due to exothermic or endothermic reaction can be detected and plotted. Thermogravimetric (TG) analysis is the technique which enables us to determine the characteristic of materials. TG determines the change in physical and chemical properties in the sample during analysis such as degradation temperature, moisture, decomposition point or level of content of organic and inorganic compound in a material. It provides the information about the weight gain or loss of the specimen during process and it records the change in mass versus increasing temperature or time. However sometime we get the weight loss curve in such a way where it was difficult to interpret and at that time DTG help us to find desired result. The DTG technique enables us to determine the weight loss with change in temperature (in that situation). DTG works on similar principle and is just the derivative of TG plot. Technique is useful because it point critical time and temperature of the reaction under eminent conditions. Moreover, it is very useful where TG technique is unable to find the point or amount of weight loss, DTA shows the point of maximum weight loss.

2.2.1.1 Theoretical background for thermal analysis

Nanomaterials with crystallite size smaller than 100 nm have achieved incredible significance in last decades. M-type hexaferrite nanoparticles have evoked several useful properties in the various field. Crystallization of nano-material plays a significant role in determining the transport mechanisms of charge carriers in crystalline materials. Several

quantitative methods have been proposed in order to evaluate the level of stability of these promising materials. Most of the methods are based on the activation energy, extent of crystallization and temperature corresponding to maximum crystallization. The exploitation of electromagnetic interference and environmental pollution encouraged for the development of single phase crystalline nanoparticles to minimize the electromagnetic interference. Therefore, it is very essential to examine the kinetic stability of the materials, whereas there is no simple way to formulate the stability of the crystalline materials to develop them as a suitable material for electronic industry. The crystallization rate has been easily and accurately evaluated by thermal differential analysis technique. DTA is a universally accepted technique for the examination of crystallization kinetics of crystalline as well as amorphous materials. There are two different approaches available for calorimetric measurements of materials; isothermal and non-isothermal technique. In isothermal transformation, any change in physical quantity of the precursor or the heat evolved during the crystallization process, when the temperature of the precursor is brought quickly above the glass transition temperature can be measured as a function of time. The non-isothermal transformation has overcome the problems related to time consumption and the un-attainability to acquire a test temperature instantaneously during the analysis. The non-isothermal transformation has been performed at constant heating rate and any change in physical parameter during the investigation is measured as a function of temperature or time [64]. Constant heating rate technique is a more reliable way for the examination of a crystal transformation comparatively, where it is difficult to achieve transition temperature instantaneously in isothermal process [65]. There are several models available for calculation of activation energy of crystallization process based on isothermal and non-isothermal process. The kinetics of crystallization is based on non-isothermal kinetic models *i.e.* Kissinger's equation [66], Matusita-Sakka theory [67] and Augis and Bennett approximation [68].

2.2.1.2 Kissinger's equations

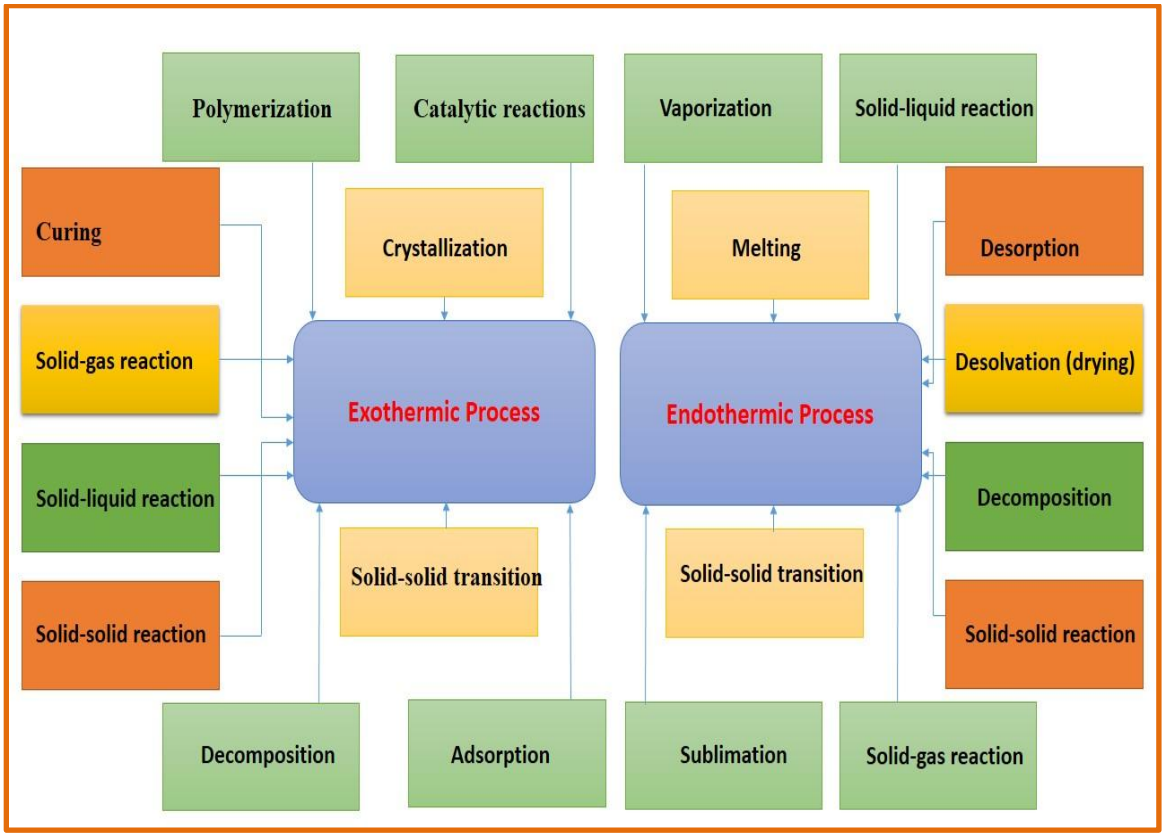

Figure 2.2: The possible chemical processes during thermal analysis (http://www.anasys.co.uk/library/dsc2.htm).

In isothermal crystallization process the fraction of crystallization can be represented as:

$$\alpha = 1 - \exp(-kt^n) \quad (1)$$

where α is the fraction of crystallization, t is time, k is the rate constant and n is the Avrami exponent. The rate of crystallization of a material can be expressed in the form:

$$\frac{d\alpha}{dt} = k_o n(1-\alpha)\,[\ln 1/(1-\alpha)^{(n-1/n)}\, exp(-E/RT)] \quad (2)$$

where E is the activation energy for the crystallization process, R is the universal gas constant (8.314 $Jmole^{-1}K^{-1}$), T is reaction temperature and k_o is the pre-exponential factor and can be calculated from Arrhenius equation:

$$k = k_o exp(-E/RT) \quad (3)$$

In isothermal crystallization process, the heating rate is always kept constant *i.e.* dT/dt = β *(*constant). The Kissinger expressed the activation energy of the crystallization process of the prepared sample at crystallization temperature for the particular heating rates following equation using the Arrhenius and rate of crystallization equation:

$$ln\frac{\beta}{T_C^2} = -\frac{E}{RT_C} + ln\frac{AR}{E} \quad (4)$$

where β is the heating rate (K/min), T_c is the maximum peak temperature of DTA curve. The plots of $\ln(\beta/T^2_c)$ against $\ln(1000/T)$ at different heating rates gives a straight line known as Kissinger's plot. Thus the slope value of the straight line obtained from these plots yield to calculate the activation energy value. The pre-exponential factor A can be determined from the linear intercept value.

2.2.1.3 Matusita and Sakka theory

Matusita and Sakka derived an expression for the determination of activation energy of crystallization (E) from classical relation of Johnson-Mehl-Avrami (JMA) equation in which the rate of crystallization at any temperature equal to crystallization temperature T_c and is independent of heating rate β. The modified equation can be expressed as follow:

$$ln\beta = -\frac{E}{RT_C} + Constant \quad (5)$$

The activation energy can be calculated from above equation by plotting graph between ln(β) against ln(1000/T_c).

2.2.1.4 Augis and Bennett approximation

Augis and Bennett also developed an approximation method to determine the value of activation energy and is given by:

$$ln\frac{\beta}{T_C} = -\frac{E}{RT_C} + Constant \quad (6)$$

Here also the slope obtained from the plots of ln(β/T_c) against ln(1000/T) at different heating rates using above equation can be used to calculate the value of activation energy.

Figure 2.3: DTA setup EXSTAR TG/DTA 6300 at IIT-Roorkee.

2.2.2 X-ray diffraction technique

The X-ray diffraction is one of the most important characteristic tool which is widely used in materials science.

Figure 2.4: Panalytical's X'pert pro XRD at Punjab University.

XRD is a versatile and non-destructive technique for the qualitative and quantitative analysis of the materials, which gives the detailed information regarding chemical composition as well as probe crystallographic structure of natural and synthesized materials at atomic level. The powder diffraction pattern produces one dimensional data rather than three dimensional location of each reflection due to the rotational projection of the randomly oriented reciprocal lattices.

Powder XRD is a long-range order technique which helps us to find the crystallization, purity of the substance, crystal transformation, allotropic transformation, lattice constants and presence of impurity or intermediates phase in the crystal lattice. XRD technique requires an X-ray, specimen and detector. When X-ray is incident on specimen it diffracts the incident ray in all possible orientation of 2θ. The intensity of diffracted radiation has been measured with the help of movable detector as function of 2θ, when the interaction between the monochromatic X-rays and crystal planes occurred. The interplanar spacing has been calculated using the Braggs equation:

$$n\lambda = 2d \sin\theta \qquad (7)$$

where, n is an order of reflection, d is the interplanar spacing, λ is the X-ray wavelength and θ is the angle of diffraction. XRD technique has been employed for structural characterization. The diffraction patterns have been recorded using Cu-Kα radiation with the help of X-ray diffractometer. Figure 2.4 shows the photograph of X-ray diffractometer (X'Pert Pro). The divergence of scanning beam on the source slide was controlled with the help of 0.15 mm slit. The specimen were scanned in the range 20° to 70° in 1°/min with step size of 0.02° operating at 45 kV and 40 mA. The X-ray peak broadening technique has been used to measure the crystallite size [69].

2.2.3 Scanning Electron Microscopy (SEM)

SEM is non-destructive microscopy technique useful in qualitative or semi-quantitative measurements. The SEM uses an electron beam of high energy for the study of the surface of specimen in which beam of electron interacts with the specimen and collects the information regarding surface morphology, chemical composition etc.;

Figure 2.5: SEM at IIT-Roorkee.

and crystalline structure and orientation of materials making up the sample. It collects the data from the specimen and produce the two dimensional images. The basic components of electron microscopy are electron gun, an anode, deflecting lenes, specimen holder and image recording system. It uses high energy beam of electrons instead of light to form an image *i.e.* tungsten or lanthanum hexaboride thermionic emitters as an electron source. The filament is resistively heated *via* current to achieve high temperature that produces electrons having high energy (Figure 2.5). These electrons are attracted by the anode and accelerated towards the sample. The series of magnetic lenes used to focus the electron beam on to the sample and aperture has been used to generate monochromatic beams (SEM Quanta 200 FEG from FEI Neitherlands microscope). Finally the monchromatic beam interacts with the surface of specimen. The different type of interaction have been occurred which are recorded with the help of different detectors. There are two type of processes occurred; elastic scattering and inelastic scattering. When a beam of electron interacts with the sample through without exchange of energy then it will be reflected back without loss of any energy. These electrons are usually called backscattered electrons. When the electron beam interacts inelastically with the specimen some of the electrons are knocked out of their orbital due to exchange of energy, and are called secondary electrons. These electrons are captured by the scintillator/photomultiplier are then amplified and their interaction has been converted into the image with the image recording system.

2.2.4 Fourier Transform Infrared Spectroscopy (FTIR)

Fourier transform infrared spectrometer has been used to study the IR properties of hexaferrite in the Mid-IR range, 4000-400 cm^{-1}, using Perkin Elmer (RX-IFTIR). Fourier transform infrared spectroscopy is a technique which enables us to identify the organic, inorganic materials and specially the presence of impurity phase in natural or synthesized materials. FTIR (Mid-IR) is a non-dispersive technique and has been applied to solid, liquid and gases due to their superior speed and sensitivity. The

dispersive instrument separate the individual frequencies of energy emitted from the radiated source. This can be done with the help of prism or grating. The infrared prism based on the similar principle like visible prism, where it separate visible light into different frequencies. However, the grating element is more sensitive and superior dispersive element which separate the infrared frequencies. The particular frequency has been allowed to specimen and detector detects the amount of energy passed through the sample. The slow scan process is major problem in dispersive instrument, because it measure single frequency at a time and it take long duration for multiple scanning.

The FTIR spectroscopy have examined all the frequencies simultaneously rather than viewing each component sequentially. The non-dispersive FTIR technique overcomes all the difficulties that are occurred in dispersive instrument and which are difficult and impossible to analyze. The initial infrared spectroscopy is based on dispersive method, where infrared light is separated or dispersed with the help of prism. This method makes the analysis slower than slow because individual frequency has been incident or passed through sample. This problem has been overcome using an interferometer which help or enable us to scan all the frequencies at one time. The non-dispersive FTIR contains not only radiation source and detector as well as interferometer, where FT stands for Fourier transform. The Figure 2.6 shows the basic components of Fourier transform infrared spectrometer. The different approach has been employed in an FTIR spectroscopy during the sample analysis and to measure the absorption spectra at different frequency components.

The radiation source is the heart of the instrument in the form of glober. The same types of radiation sources are used for both dispersive and Fourier transform spectrometers. The IR beam is collimated with help of collimeters and allow to incident on a beam splitter. The beam splitter splits the incident beam into two components in which 50% of incident beam is reflected towards the movable beam and remaining component is transmitted. It generates the optical path difference between the beams. The beams are returned back to beam splitter. These beams are then recombines with each other which

produces interference phenomenon which can be measured as a function of optical path difference by a detector.

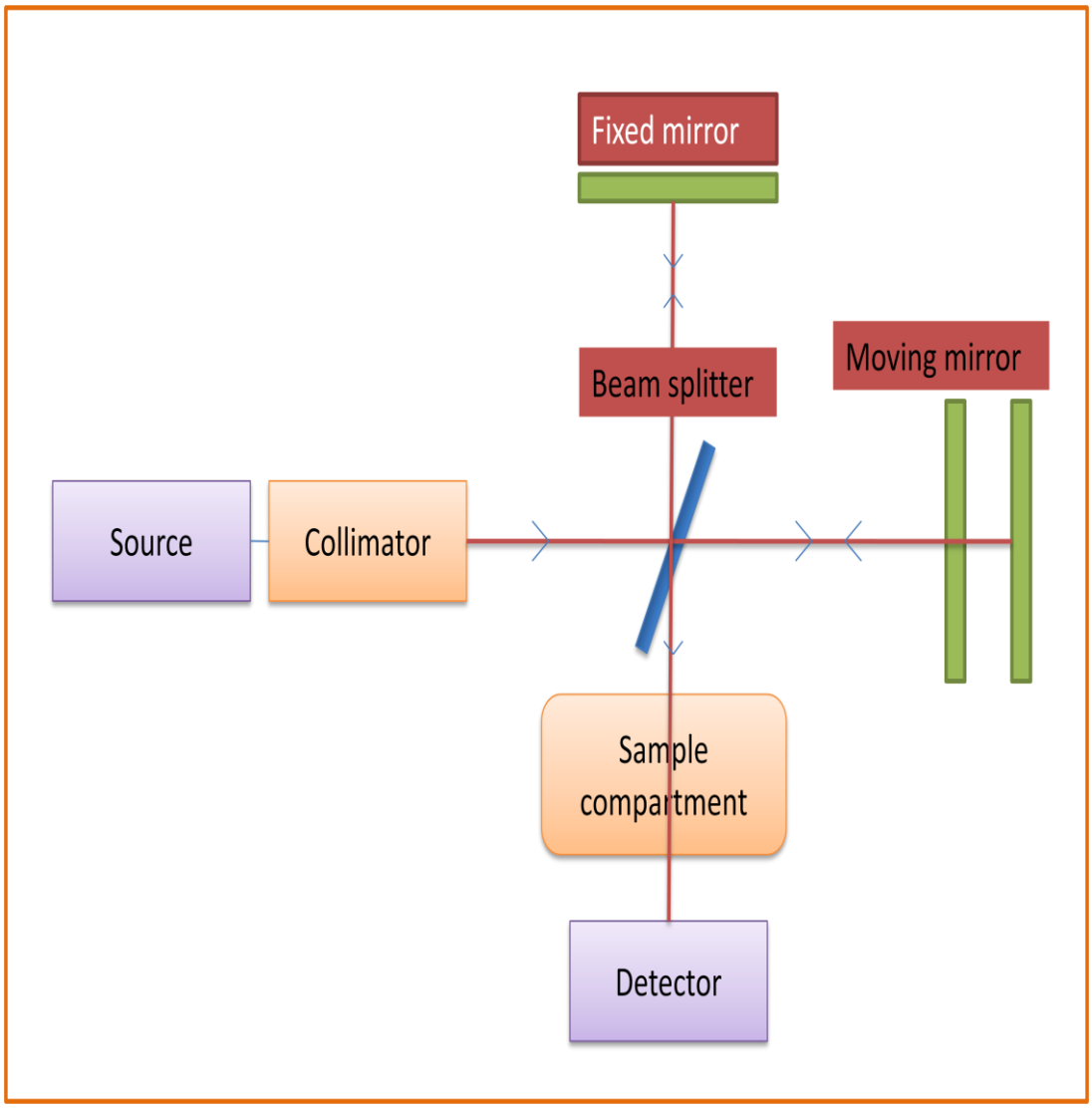

Figure 2.6: Schematic diagram of FTIR- Spectrometer-RZX, Perkin Elmer.

A complete different approach is taken in an FTIR spectrometer to differentiate and measure the absorption at component frequencies. The monochromator is replaced by an interferometer, which firstly divides the radiant beams and generates an optical path difference between the beams. It then recombines them in order to produce repetitive interference signals measured as a function of optical path difference by a detector. As its name implies, the interferometer produces interference signal, which contain infra-red spectral information generated after passing through a sample. The Michelson interferometer is commonly used interferometer which consists of; moving and fixed mirrors as well as a beam splitter. This beam splitter (semi reflecting devices) and the mirror are perpendicular to each other and have unique functioning. The radiation source emits infrared light which is collimated with the help of collimator and directed towards the interferometer. The beam splitter split the light into two parts, the half of the IR beam is reflected towards moving mirror and half of the part is transmitted to the fixed mirror. Both the beams move some path and again recombine at beam splitter [70]. The interference between two reflecting beams generates patterns due to change in relative position of fixed and moving mirrors. Finally resultant beam passes through the specimen and the part of light absorbed or transmitted through sample has been detected through detector.

2.2.6 Vibrating Sample Magnetometer (VSM)

The magnetic properties of the hexaferrites are investigated with the help of vibrating sample magnetometer. Hysteresis loops of the different ferrite samples were analyzed at room temperature up to the applied magnetic field 10 kOe using VSM (Model PAR 155, from Princeton Applied Research USA; and Lakeshore 7410). This study is carried out in order to take the measurements of the different magnetic parameters, *viz.* saturation magnetization (M_S), retentivity and coercivity (H_C) of the hexaferrites. The schematic diagram of VSM and their components have been shown in

Figure 2.8, respectively. The VSM is used to study the magnetic behavior of magnetic materials and the instrument is based on the principle of Fraday laws of induction *i.e.*

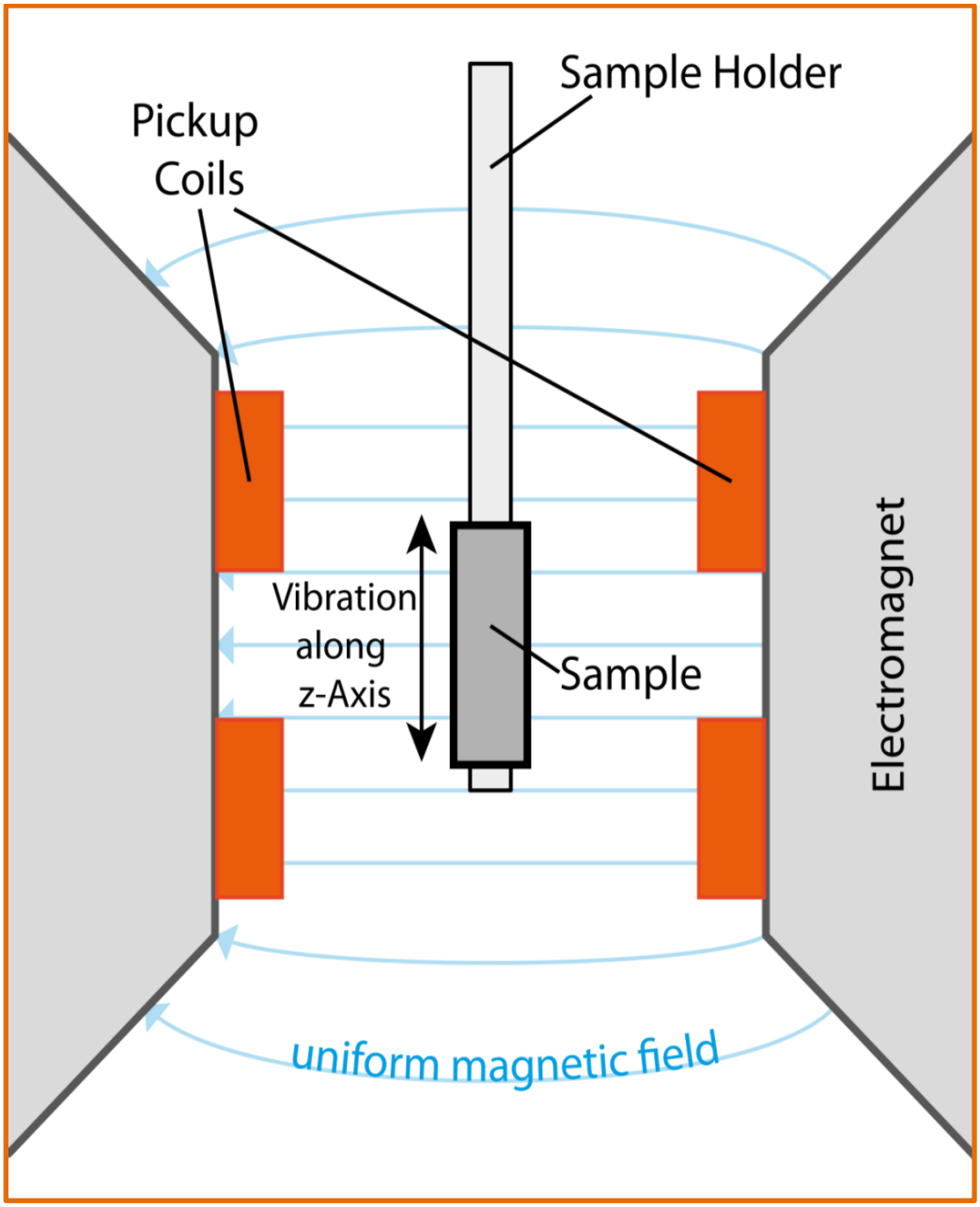

Figure 2.8: Schematic diagram of VSM
(http://en.wikipedia.org/wiki/Vibrating_sample_magnetometer)

varying magnetic field will produce an electric field. Magnetization in the sample is to be studied by applying a uniform or constant magnetic field to sample. If the specimen is magnetic in nature then applied magnetic field will magnetize the sample by aligning the magnetic domains along the direction of applied field. However, the applied magnetic field is generally not uniform but slowly varied. The induced changes in the magnetic field are detected by search coil. The alignment of magnetic domains or spins originates magnetic field around the samples. When the sample is moved up and down this field varies as a function of time and can be sensed by asset of pick up coils. The change in magnetic field causes an electric field in pick up coils. This measured electric field gives the information about the changing magnetic field and this current is proportional to magnetization of the sample. The stronger the magnetization, larger the induced current and this current can be amplified by amplifier. The behavior of magnetic materials such as paramagnetic, diamagnetic, ferromagnetic and other samples can be distinguished by plotting saturation magnetization (M_S) versus applied field (H).

2.2.7 Formulas

The crystallite size D, strain η and specific surface area S, have been calculated using following equations [71-75]:

$$D = \frac{k\lambda}{\beta Cos\theta} \tag{8}$$

$$\beta \,\mathrm{Cos}\,\theta = \frac{0.9\lambda}{D} + 2\,\eta\,\mathrm{Sin}\,\theta \tag{9}$$

$$S = \frac{6000}{D\,\mathrm{D_x}} \tag{10}$$

$$\frac{1}{d_{hkl}^2} = \frac{4}{3}\left(\frac{h^2 + hk + k^2}{a^2}\right) + \frac{l^2}{c^2} \tag{11}$$

where, λ (1.54056 Å) is the X-ray wavelength, β is the full width at half maximum in radian, θ is the Bragg's angle, D_x is the X-ray density, lattice parameters (a and c), d_{hkl} is the d-spacing value and h, k and l are the corresponding miller indices of the diffraction lines in XRD patterns.

The porosity P in the system has been calculated using the relation [73]:

$$P = \left(\frac{D_x - D_b}{D_x} \right) \times 100 \qquad (12)$$

where, D_b is bulk density. X-ray density D_x has been measured using the expression [72]:

$$D_x = \frac{ZM}{N_A V_{cell}} \qquad (13)$$

where, M is the molecular weight, N_A is Avogadro's number, V_{cell} is volume of nanoparticles and Z is the number of molecules per unit cell. Preferential orientation of crystal growth has been measured by texture coefficient (T_C) [76].

$$T_c = \frac{I_{(hkl)} / I_{o(hkl)}}{(1/N)\left[\sum_N I_{(hkl)} / I_{o(hkl)} \right]} \qquad (14)$$

where, I is the observed intensity, I_o is the standard intensity (*JCPDS*-International Center for Diffraction Data) and N is the number of diffraction peaks. The energy barrier is the minimum applied field required for spin reversal of the nanoparticles in the direction of magnetic field orientation and can be expressed as [77]:

$$E_A = KVSin^2\theta \qquad (15)$$

where, V volume of nanoparticle, E_A is the energy barrier and θ is the angle between the applied field and easy axis of the nanoparticles. The magnetocrystalline anisotropy

constant for single domain nanoparticles has been determined by saturation magnetization and coercivity value [78]:

$$H_C = \frac{2K}{\mu_o M_S} \qquad (16)$$

where, μ_0 is the permeability of free space, K is magnetocrystalline anisotropy constant and M_S is the saturation magnetization.

CHAPTER III

Synthesis and Characterization of Strontium Hexaferrite Nanoparticles: $SrFe_{12}O_{19}$

3.1 Introduction

The strontium hexaferrite ($SrFe_{12}O_{19}$) is a hard magnetic material with magnetoplumbite structure [79]. This material has attracted much attention in past few decades due to their scientific and technological applications in the region of microwave to radio frequencies. This is due to high magnetocrystalline anisotropy, high Curie temperature, high electrical resistivity, high dielectric constant as well as high magnetization and coercivity [80-83]. The dielectric and magnetic properties of ferrite materials in the nano regime are significantly different from their bulk counterparts. M-type $SrFe_{12}O_{19}$ has a space group $P6_3/mmc$ and often expressed as RSR*S*. The S and R block stands for spinal and hexagonal structure. R* and S* are the blocks obtained by 180° rotation of R and S with respect to c-axis having equivalent atomic arrangements [84,85]. The hexagonal hard ferrite contains two 64 ions per unit cell on 11 different sites. The Fe^{3+} ions are distributed over five distinct crystallographic sites, three octahedral sites (12k, 2a, $4f_2$), one tetrahedral site ($4f_1$) and trigonal bipyramidal site (2b) [86]. These crystallographic sites are coupled by O^{2-} ions to form collinear ferrimagnetic order and superexchange interaction between Fe^{3+}-O^{2-}-Fe^{3+}. The superexchange interaction and magnetocrystalline anisotropy are strongly depends upon the site occupation and different crystallographic site construct different role to dielectric and magnetic properties.

In this chapter, citrate precursor technique for the synthesis of $SrFe_{12}O_{19}$ nanoparticles has been used. This method allows the subsequent crystallization to occur at low temperature, leading to formation of nanoparticles due to intimated mixing of staring materials on ionic levels and low cost technique for the mass production. The reaction kinetics for the prepared $SrFe_{12}O_{19}$ nanoparticles has been examined through differential thermal analysis using non-isothermal model. The effect of calcination temperature and crystallinity on the structural, morphological, dielectric and magnetic properties has been examined. Various parameters such as activation energy, particle size, dielectric constant, magnetization and coercivity have been calculated.

3.2 Experimental

3.2.1 Synthesis and characterization: $SrFe_{12}O_{19}$

Synthesis of strontium hexaferrite nanoparticles was accomplished in an aqueous reaction matrix containing ferric nitrate nonahydrate, strontium nitrate, lanthanum nitrate hexahydrate and citric acid monohydrate as discussed in chapter 2. DTA (EXSTAR TG/DTA 6300), XRD, FTIR, SEM and VSM have been used to study the effects of substitution on various properties.

3.3 Results and discussion

3.3.1 Thermal analysis

The trace of DTA/DTG/TG for a precursor powder at the heating rate of 5 K/min in air atmosphere has been shown in Figure 3.1a

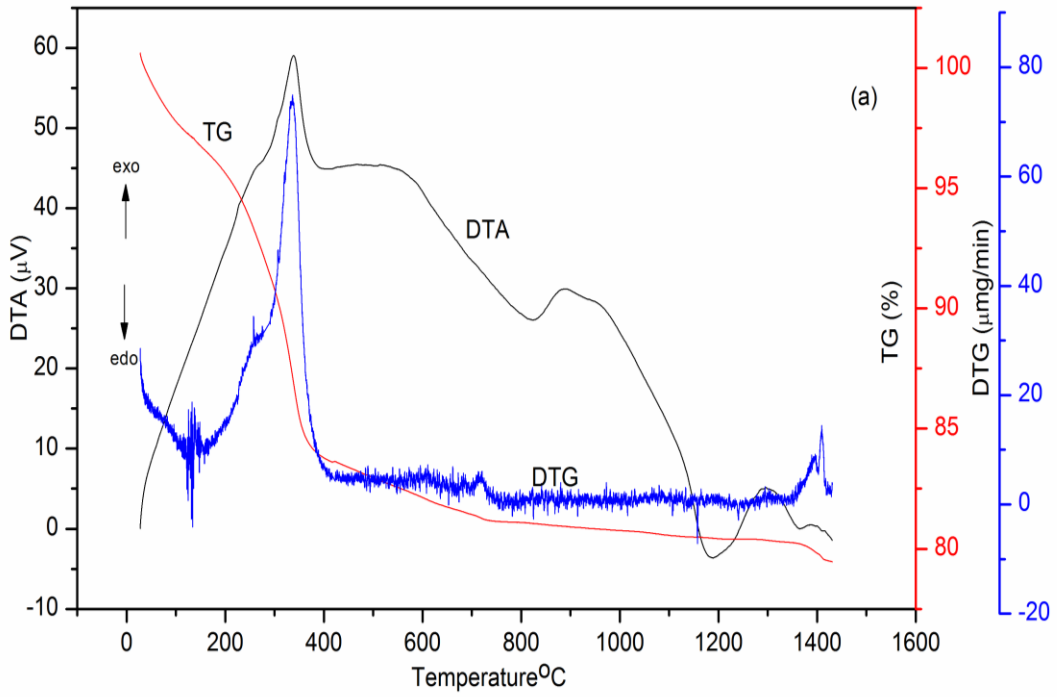

Figure 3.1a: TG/DTG/DTA curves of the precursor of strontium hexaferrite at heating rate of 5 K/min.

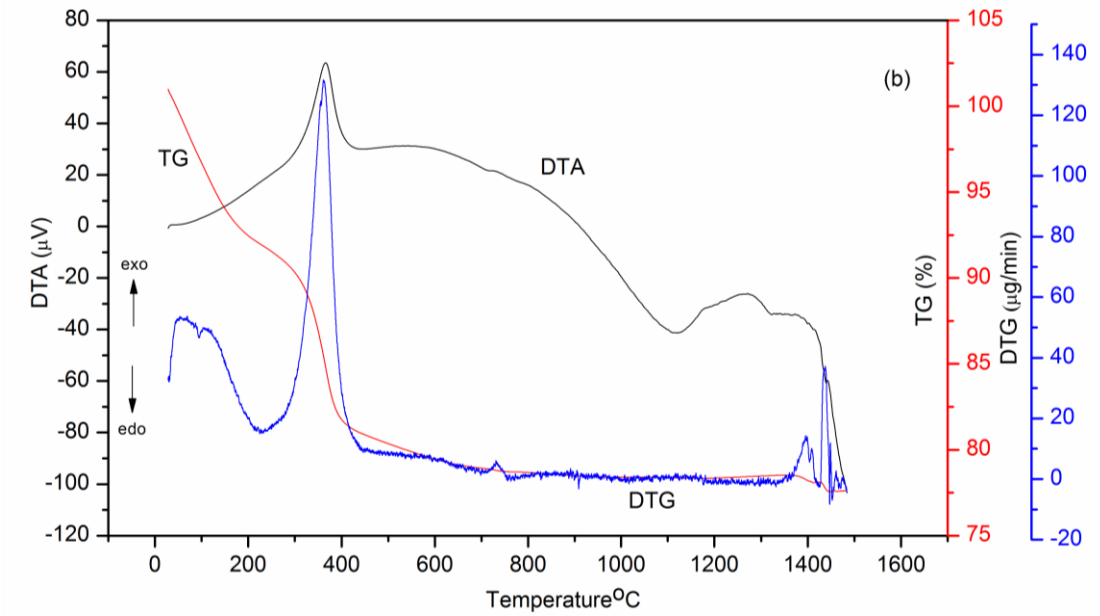

Figure 3.1b: TG/DTG/DTA curves of the precursor of strontium hexaferrite at heating rate of 10 K/min.

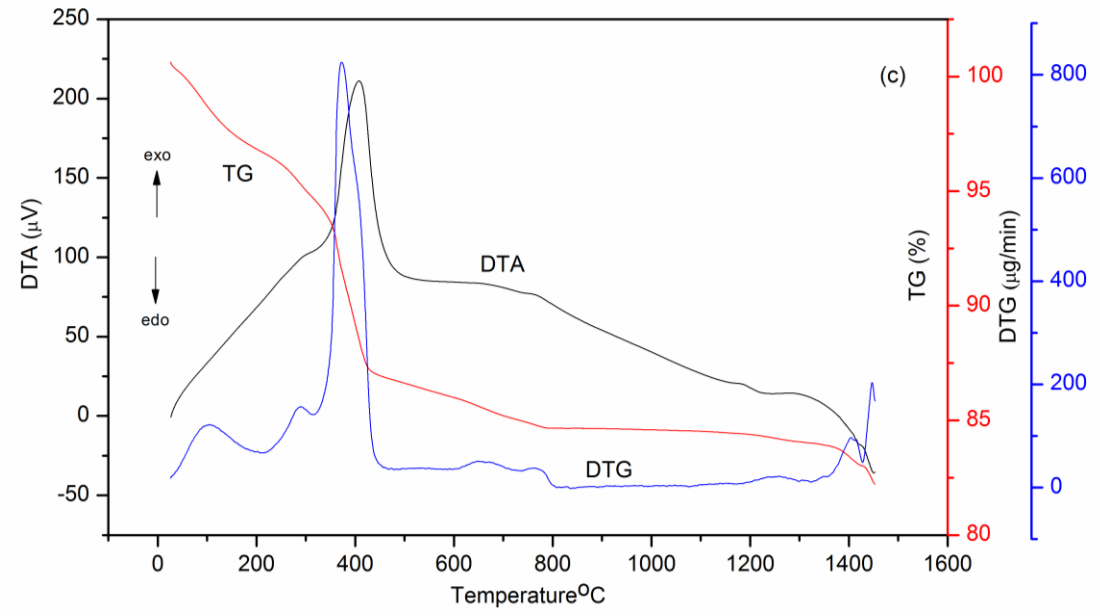

Figure 3.1c: TG/DTG/DTA curves of the precursor of strontium hexaferrite at heating rates of 50 K/min.

During the thermal analysis, it has been seen from the TG-curve that the weight loss of a precursor happens in three distinct steps in the temperature range from room

temperature to 1430°C. The steps occurred at 74-184°C, 330-409°C and 640-942°C respectively. The precursor exhibited a rapid weight loss up to 400^{o}C indicating the hydroscopic nature. This weight loss can be attributed to the removal of water residues from macro and meso pores [87]. In temperature range from 400°C to 942°C an additional weight loss (few amount) of a precursor has been observed. This can be credited to the combustion and decomposition of citrate precursor, and to the reaction of intermediates [88,89]. The DTA-curve in Figure 3.1a depicts both exothermic and endothermic effects of a precursor in the temperature range of 25-1430°C. The DTA results are consistent with the results of TG/DTG. The existence of an exothermic peak at the point of maximum weight loss i.e. 336°C (DTG) is related to decomposition of a precursor composed of citrate-nitrate gel. The formation of hexaferrite phase is not the single step reaction as observed in the case of spinal ferrite. Thermal analysis reveals that the formation takes place in steps by means of endothermic reaction [90]. The existence of an endothermic peak at 824°C corresponds to the formation of $SrF_{12}O_{19}$ as well as intermediate phase. This has also been confirmed by the XRD analysis of a precursor powder calcinated at 700°C and 800°C in air atmosphere. Above the second endothermic peak no further weight loss will be observed in TG-curve indicating the completion of reaction [91].

To aid the further investigation of crystallization process, similar analysis have been carried out under same conditions except the heating rates, 10 and 50 K/min presented in Figure 3.1b and 1c respectively. Similar behavior has been observed for all the measurements with slight shift of DTA peaks to upward direction. It is concluded that for the different heating rates, there are different temperatures for the completion of reaction. The lower the heating rate; lower will be the reaction temperature. The present thermal investigations of a precursor powder at different heating rates will aid in the selection of reaction temperature with proper heating rate for formation of single phase strontium hexaferrite nanoparticles.

There are several models available for calculation of activation energy of crystallization process based on isothermal and non-isothermal processes. In present work we report, the kinetics of crystallization based on non-isothermal kinetic models *i.e.* Kissinger's method, Augis and Bennett approximation and Matusita-Sakka theory

[92-94]. The Kissinger expressed the activation energy of the crystallization process of the prepared sample at crystallization temperature for the particular heating rates following equation using the Arrhenius and rate of crystallization equation:

$$\ln\frac{\beta}{T_C^2} = -\frac{E}{RT_C} + \ln\frac{AR}{E} \qquad (1)$$

where β is the heating rate (K/min), T_C is the maximum peak temperature of DTA curve.

E is the activation energy for the crystallization process, R is the universal gas constant (8.314 $Jmole^{-1}K^{-1}$) and A is the pre-exponential factor.

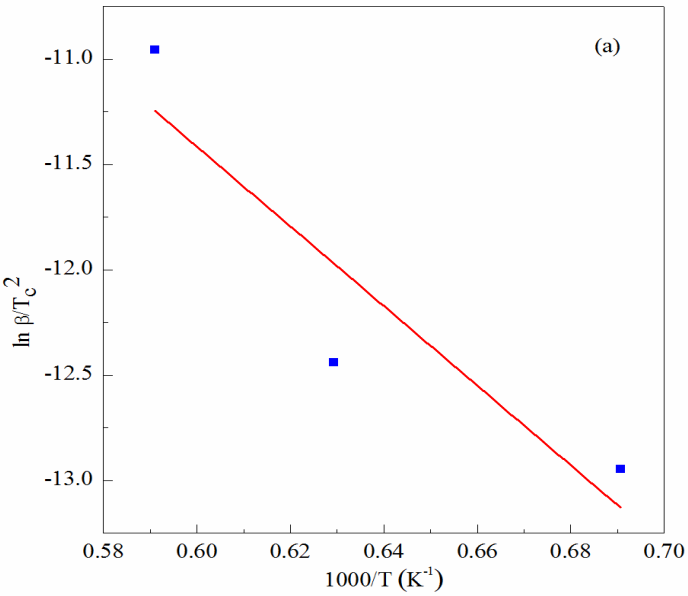

Figure 3.2a: Kissinger's plot for the crystallization process of $SrFe_{12}O_{19}$ precursor powder.

The plots of $\ln(\beta/T^2_c)$ against $\ln(1000/T)$ at different heating rates gives a straight line known as Kissinger's plot (Figure 3.2a). Thus, the activation energy value has been obtained from slope of the straight line of these plots. The calculated value of activation energy for crystallization process of $SrFe_{12}O_{19}$ is, 157 KJ/mol. Activation energy have been verified by employing Augis-Bennett approximation (Figure 3.2b) Matusita-Sakka theory (Figure 3.2c) and non-isothermal kinetic models. The

activation energy values determined from these models are in close resemblance to each other as shown in Table 3.1.

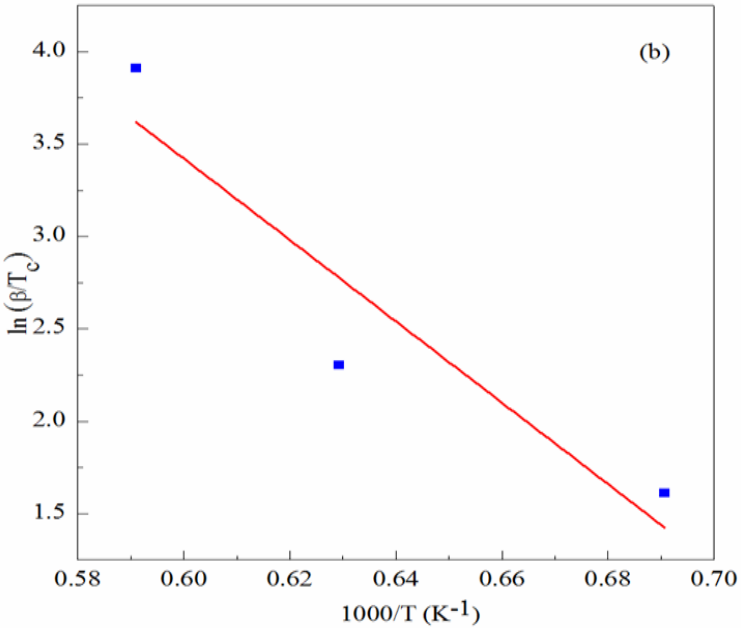

Figure 3.2b: Augis and Bennett plot for the crystallization process of $SrFe_{12}O_{19}$ precursor powder.

.

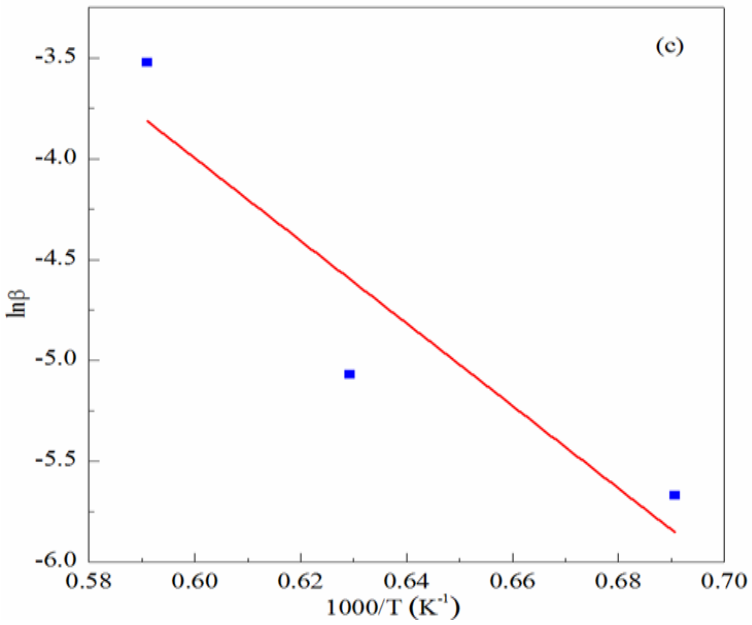

Figure 3.2c: Matusita-Sakka plot for the crystallization process of $SrFe_{12}O_{19}$ precursor powder.

Table 3.1: Crystallization temperature (T_C) and activation energy for crystallization temperature (E) of $SrFe_{12}O_{19}$ at different heating rates.

Heating rate (K)	5	10	50
T_C (K)	144	1589	1692
E (Kissinger) /kJmol^{-1}		152	
E (Augis and Bennett) /kJmol^{-1}		183	
E (Matusita) /kJmol^{-1}		170	

3.3.2 Structural analysis

3.3.2.1 X-ray diffraction

Crystallization process has been interpreted by means of X-ray diffraction studies; for this the precursor powder (A_0) has been further calcinated for different temperatures 700°C (A_1), 800°C (A_2) and 1200°C (A_3). The X-ray diffraction patterns of precursor and calcinated powders have been presented in Figure 3.3(a-d).

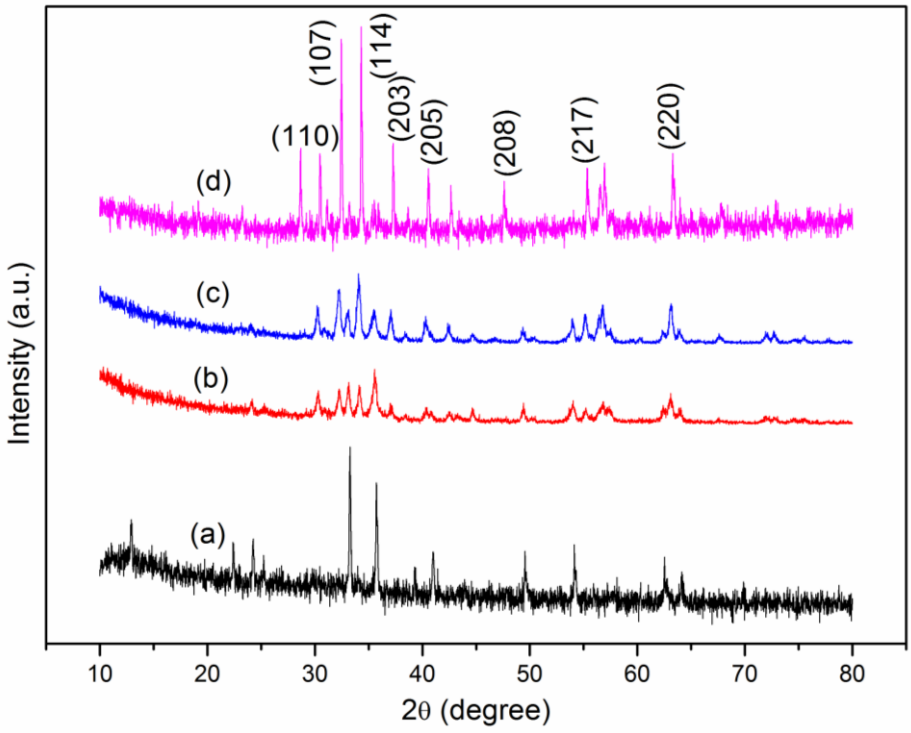

Figure 3.3: X-ray diffraction patterns of $SrFe_{12}O_{19}$ (a) precursor powder and sample calcinated at (b) 700°C, (c) 800°C, (d) 1200°C.

The diffraction pattern of a precursor (Figure 3.3a) shows broad peaks, indicating the presence of nanocrystalline phase. This can be attributed to the existence of organic compounds in precursor powder [95]. As the calcination temperature of precursor powder increases, the diffraction peaks become narrower and intense, representing enhancement of crystallite size and crystallinity respectively. The diffraction patterns of A_1 and A_2 samples shows the formation of ferrite phase along with the presence of secondary phases such as α (γ)-Fe_2O_3 and $SrFe_2O_4$ [96-98]. The existence of secondary phases indicates the incomplete reaction between Fe^{3+} and Sr^{2+} under these synthesis conditions. The presence of α-Fe_2O_3 phase, indicates the system need longer and high calcination temperature for the completion of reaction. This is because, the crystal structure of α-Fe_2O_3 is orthorhombic hexahedron and difficult to convert into ferrite phase as compared to γ-Fe_2O_3 [99]. The sample A_3 (Figure 3.3d) represents the sharp, intense and narrower diffraction peaks, and disappearance of secondary phase indicating the formation of single phase M-type hexaferrite with high crystallinity. All the apparent peaks (110), (114), (107), (203), (205), (206), (208), and (303) in diffraction pattern have been similar to standard (*JCPDS:* 80-1198) diffraction pattern of hexagonal ferrite. The diffraction peak broadening technique has been employed for most intense (114) peak to calculate the crystallite size. The crystallite size for $SrFe_{12}O_{19}$ nanoparticles has been calculated using (eq. 8) Scherrer's formula [100,101]. The calculated crystallite size has been shown in Table 3.2 and it can be seen that the crystallite size increases with the increasing calcination temperature in the direction parallel to c-axis (114).

Table 3.2: Variation of crystallite size with different calcination temperatures.

$SrFe_{12}O_{19}$	Standard 2θ (°)	Observed 2θ (°)	Miller indices (MI)	D (nm)
700°C	34.19	34.08	(114)	26.80
800°C	34.19	34.13	(114)	30.77
1200°C	34.19	34.32	(114)	69.28

The sample A_3 stands for maximum crystallite size but still smaller than the single domain crystal particle size ~270 nm as reported earlier [102,103]. The crystallinity and crystal growth of nanoparticles are closely related to calcination. The growth of crystallite size with increasing calcination temperature can be accredited to the fusion of nanoparticles with each other by melting their surfaces. The fusion of nanoparticles well below their melting point is owing to weak binding of surface atoms result in sharp decrease of surface melting point [104,105].

3.3.2.2 Mid-Infrared spectral region analysis

The Mid-IR spectra of a precursor and calcinated powder are shown in Figure 3.4(a-d).

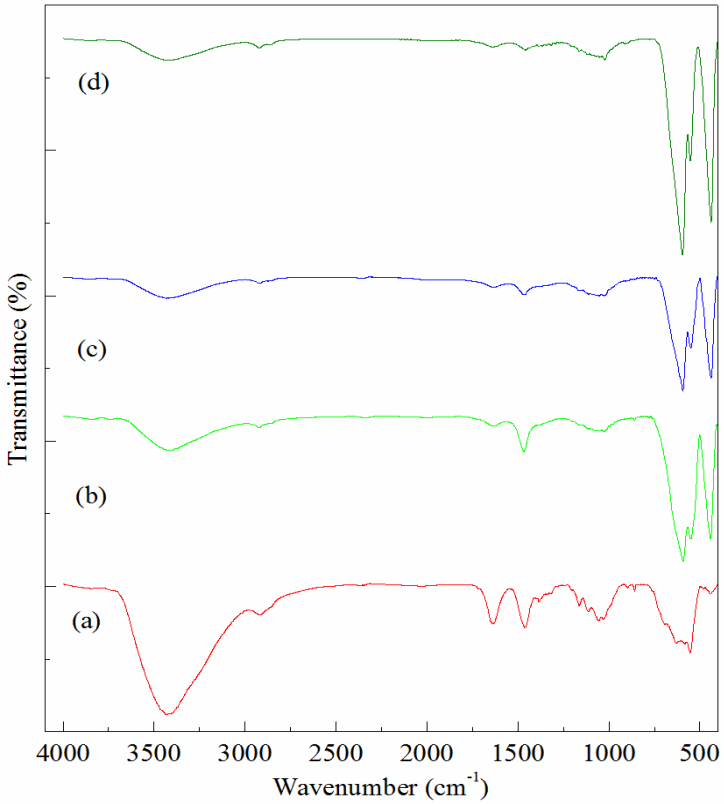

Figure 3.4: Mid-IR spectra of $SrFe_{12}O_{19}$ (a) precursor powder and sample calcinated at (b) 700°C, (c) 800°C, (d) 1200°C.

FTIR-spectrum of a precursor in Figure 3.4(a) shows that the characteristic bands have appeared in the range of 3200-3270 cm^{-1} and 1638 cm^{-1}. These bands are

assigned to be hydroxyl and carboxyl group of citric acid respectively [106,107]. The absorption peak at 1059 cm^{-1} corresponds to C-O stretching vibration of C-O-H band. Frequency bands near 1460.37 cm^{-1}, 1383.59 cm^{-1} and 858.82 cm^{-1} are attributed to nitrate ions [108]. After the calcination of precursor at 700°C, peak appears at 1465.72 cm^{-1} in Figure 3.4(b) and is ascribed to absorption of strontium carbonate bands [109,110]. The observed absorption bands in the range 400-800 cm^{-1} are due to iron oxide [98,111-113]. The absorption band at 2916.52 cm^{-1} arise from Fermi resonance between stretching vibration of O-H band and combination of frequency of stretching vibration of C-O and bending vibration of C-O-H band [89]. The metal-oxygen stretching bands are prominent and other bands start decreasing but still persist (Figure 3.4c) after heating the precursor powder at 800°C. Characteristic bands of CO_2^- group and NO_3^- ions have been diminished after heating the sample to 1200°C which shows the completion of redox reaction in which citrate ions act as reductant and nitrate ions as oxidant [106,107]. A new set of completely resolved bands have been appeared (Figure 3.4d) at wavenumber of 435.05, 551.04 and 594.26 cm^{-1} and identified as stretching vibration of metal-oxygen bond indicating the formation of hexaferrite [98,108,114].

3.3.3 Morphology of strontium ferrite nanoparticles

The SEM micrographs of sample calcinated at different temperatures have been depicted in Figure 3.5(a-c). The average grain size of strontium hexaferrite estimated from SEM micrograph to be ~100 nm. SEM micrograph for precursor has been presented in Figure 3.5(a). It can be seen from the micrograph that the particles are embedded in a sheet like structure due to the presence of impurities or incomplete reaction in sample as confirmed from X-ray diffraction analysis. Small size particles are formed due to fragmentation of sheet like structure with the increase of calcination temperature may be the calcination is responsible for this. It is known that the microstructure of nanoparticles can be influenced and improved by heat treatment [115]. The sample calcinated at 700°C becomes plate or needle like shape (Figure 3.5b). This can be attributed to increase in crystallinity of particles, but morphology of particles still not flawless. It has also been observed from the micrograph that the

particles exhibit porous and agglomerated microstructure. The ignition of sample causes evolution of large amount of gases during combustion or decomposition process and magnetic nature of particles has been responsible for high porosity and agglomeration respectively [116,117].

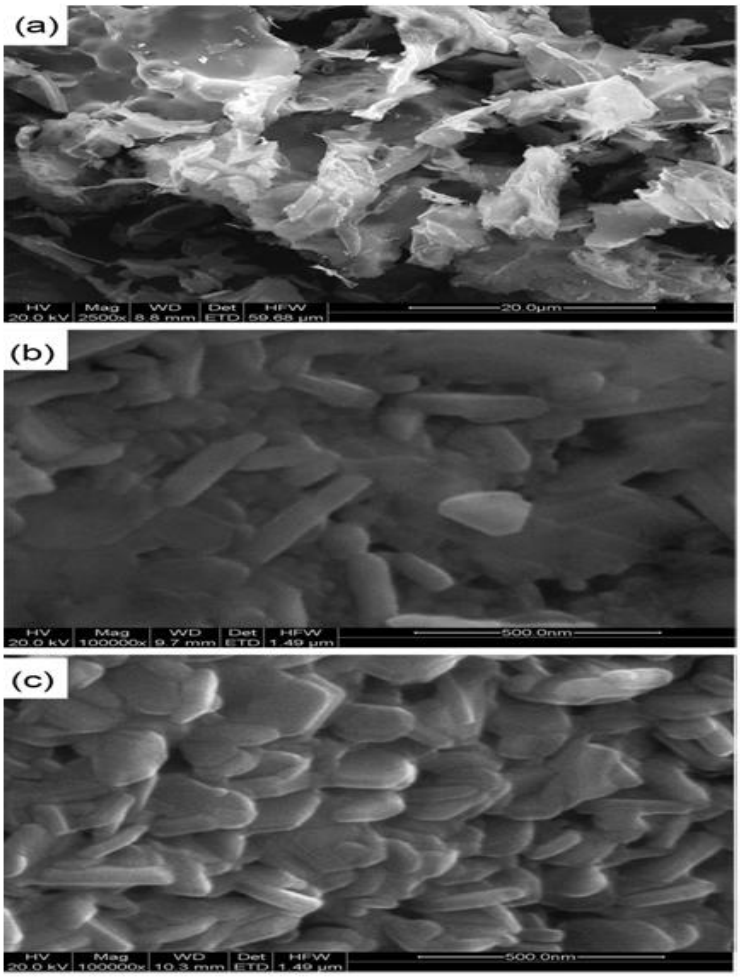

Figure 3.5: SEM micrographs of $SrFe_{12}O_{19}$ (a) precursor powder and sample calcinated at (b) 700°C, (c) 1200°C.

The calcination temperature mends the crystallinity of ferrite phase and can be describe in terms of Ostwald ripening [118]. Ostwald ripening is a process in which large number of nanoparticles are formed initially, but later only few of them remain which grow in size at the cost of smaller ones. The ultrafine and homogeneous

particles have been formed with immaculate and well resolved hexagonal structure for the sample calcinated at 1200°C (Figure 3.5c).

3.3.4 Magnetic analysis

The magnetic properties of a precursor and calcinated powder have been measured from hysteresis loops and can be seen in Figure 3.6.

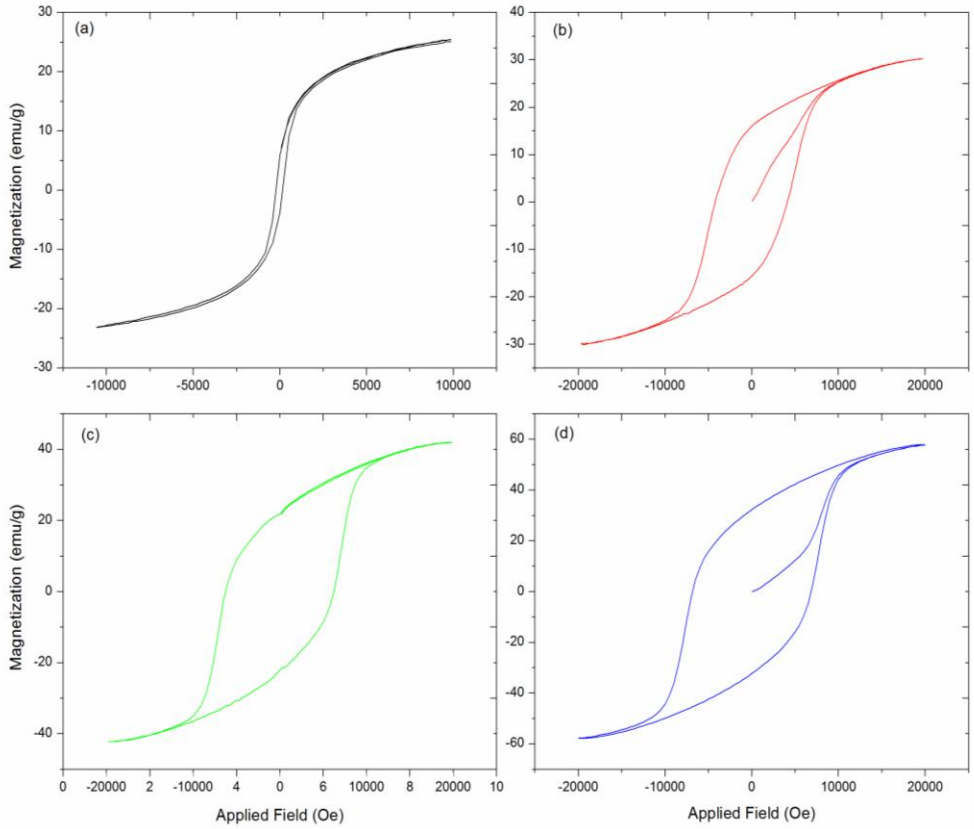

Figure 3.6: Hysteresis loops of $SrFe_{12}O_{19}$ (a) precursor powder and sample calcinated at (b) 700°C, (c) 800°C, (d) 1200°C.

The magnetic properties of ferrite system are influenced by chemical composition, calcination temperature, impurities, and morphology as well as preparation technique [119]. The measured values are listed in Table 3.3. It is observed from Figure 3.6(d) that the magnetic properties perk up as the calcination temperature increases and the optimum values for prepared $SrFe_{12}O_{19}$ have been obtained for the sample calcinated at 1200°C. The continuous improvement in magnetic parameters can be indorsing to

the progressive reaction between un-reacted constituents of iron oxide and non-ferromagnetic monoferrite to form 100% single phase hexaferrite, as discussed above the crystallinity increases with calcination. The low H_C and M value of a precursor powder corresponds to the presence of γ-Fe_2O_3 and non-magnetic phase of strontium oxide respectively [98]. The improvement in crystallinity, phase homogeneity and increase in magnetic domain size of particles result in the alignment of magnetic spins along the direction of applied field [104], and as a consequence the magnetization and coercivity value increases [120,121]. The obtained optimum results for sample calcinated at 1200°C are consistent with the thermal analysis indicating the formation of pure ferrite phase. The variation of coercivity (reverse magnetic field to demagnetize the nanoparticles) with crystallite size has been shown in Figure 3.7.

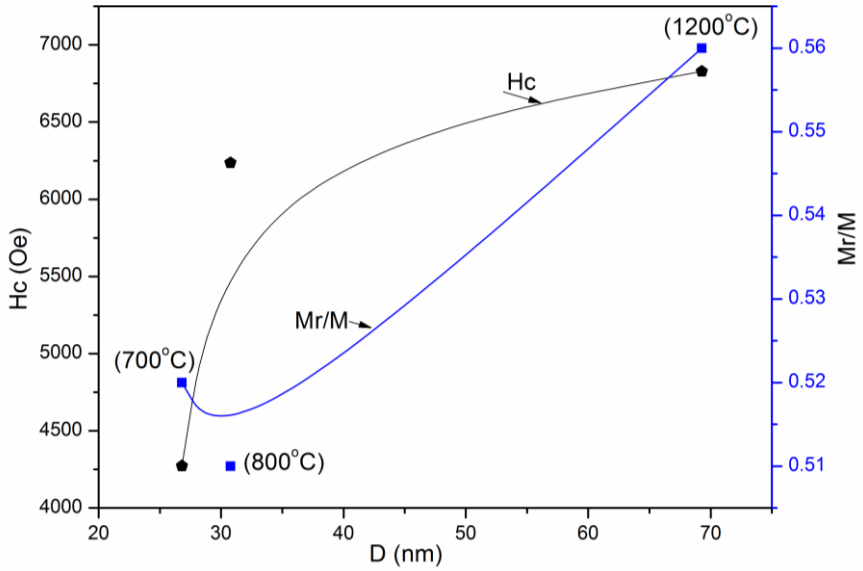

Figure 3.7: The coercivity and squareness ratio of $SrFe_{12}O_{19}$ as a function of crystallite size.

According to Stoner-Wohlfarth single domain theory the coercivity for single domain nanoparticles is approximated by eq. (16) [122]. H_C is directly proportional to energy barrier according to the eq. (15) [120]. The E_A is also proportional to V under the same magnetization direction and thus, the coercivity of nanoparticles is closely related to crystallite size. The increment in coercivity of hexaferrite nanoparticles with

an increase of crystallite size can be explained on basis of Herzer theory [123]. According to Herzer theory, the coercivity of nanoparticles is proportional to D^6 when the crystallite size is within the range of single domain size and inversely proportional to *D* for multi-domain sized particle. Also Figure 3.7 depicts the relationship between squareness ratio with crystallite size. The *Mr/M* ratio is generally known as squareness ratio (SQR), where *Mr* is remanence. The SQR is very important factor in the field of recording media of high density and permanent magnets. Generally, high SQR values have been preferred in such applications. It has been clear from Table 3.3 that SQR increases with increase in temperature (or D) and maximum for highest temperature. However, the samples calcinated at lower temperature shows lower SQR values and it may be attributed to the presence of intermediate phases. The SQR ratio is found to be ~ 0.51-0.56 for all three cases which is the expected value for randomly packed single domain hard magnetic materials. It is comparable remanence value for the same given by the Stoner–Wohlfarth model.

Table 3.3: Values of magnetization, coercivity and squareness ratio for $SrFe_{12}O_{19}$ sample.

$SrFe_{12}O_{19}$	***M* (emu/g)**	**H_C (Oe)**	***Mr/M***
Precursor Powder	25.46	232.8	0.27
700°C	30.17	4272.34	0.52
800°C	41.98	6235.75	0.51
1200°C	57.76	6828.54	0.56

3.4 Conclusions

Hexagonal shaped nanoparticles (69 nm) of $SrF_{12}O_{19}$ have been successfully synthesized when the precursor is calcinated at 1200°C for 4h, using citrate precursor technique. The morphology and crystallite size are strongly influenced by the calcination temperature. The DTA technique reveals that the highly crystalline nanoparticles are formed by the endothermic reaction. The reaction kinetics for the crystallization process of $SrF_{12}O_{19}$ yielded overall activation energy of 157 kJ/mole using Kissinger's non-isothermal model. The crystallization involves the weight loss

of a precursor in three distinct steps. The intense weight loss in the temperature range 30-400°C indicates the hydroscopic nature. The formation of ferrite phase was followed by reaction between intermediates rather than single step formation. The average crystallite size of $SrF_{12}O_{19}$ nanoparticles measured from SEM is larger than the crystallite size calculated from X-ray peak broadening technique. This is attributed that the SEM gives the size of secondary particles rather than size of primary particles. The magnetic parameters are closely related to the crystallinity of particles. It is found that the sample calcinated at 1200°C have higher M and H_C value while comparing with sample calcinated at 700°C. This improvement in hysteresis is considered to be the progressive reaction of intermediates with the calcination temperature. The prepared strontium hexaferrite nanoparticles with preeminent hexagonal crystal structure and size are used as a dielectric or magnetic filler to minimize the electromagnetic interference. The high coercivity and single domain sized nanoparticles can be aid to obtained desired signal to noise ratio (SNR) which can be used for high density perpendicular recording media.

CHAPTER IV

Synthesis and Characterization of La^{3+} doped Strontium Hexaferrite Nanoparticles: $SrLa_xFe_{12-x}O_{19}$

4.1 Introduction

In late 1970's after the discovery of perpendicular recording media, the hard magnetic materials have engrossed an interest of industry researchers worldwide [124]. Perpendicular recording suggested the possibility that the hard drives have areal density higher than 100 Gbits/in^2 [125]. Recently, IBM has announced the fabrication of high density recording media based on hard magnetic materials having capacity 15 times greater than the commercially available recording media [126]. A wide range of smart materials have been used in the fabrication of HDDs based on CoCr (CoCrPt, CoCrPt–SiO_2 and CoCrTa), FePt and iron carbonitrides. However, most of the recording media devices are based on ferrite materials due to their unique properties including large magnetocrystalline anisotropy, perfect chemical and thermal stability [127]. Hard magnetic materials have also fulfilled the technological demands for various electromagnetic absorbers and recording media devices. Recording devices encountered the problems to store number of bits per unit area (areal density) associated with media noise and thermal instability. In order to achieve high areal density (HAD) and signal to noise ratio (SNR), a lot of research work has been carried out to increase the HAD and SNR by reducing the grain size and grain size distribution. Hence, the preparation of uniform single crystalline material with desired particle size is a challenging task. Several methods are available in the literature for the synthesis of strontium hexaferrite [128]. Among them citrate precursor technique is an advanced, highly effective and widely used technique in the industries for the preparation of nanoferrite. This technique allows the subsequent crystallization to occur at low temperature, leading to formation of uniform nanoparticles due to intimated mixing of staring materials on ionic levels and low cost approach for the mass production.

The morphological and magnetic properties of materials are strongly affected by preparation technique and the substitution of cation ions on different crystallographic sites (Fe-sites). Iron ions in strontium ferrite are distributed over five distinct crystallographic sites. The sites are coupled by O^{2-} ions to form collinear ferrimagnetic order and superexchange interaction between Fe^{3+}-O^{2-}-Fe^{3+} [85,129] and are responsible for dilution and enhancement of magnetic properties. The

superexchange interaction and magnetocrystalline anisotropy strongly depend upon the site occupation and the substitution of an element on different crystallographic sites. It also plays an important role in accessing the magnetic properties of the sample. In this perspective, researchers have investigated the effects of substitution of various cation ions from transition metal ions to rare earth elements on the Sr or Fe-sites for enhanced magnetic properties in particular application. The effects of doping of La^{3+} ions in strontium hexaferrite have been studied in this chapter by the means of structural, morphological and magnetic characterization.

4.2 Experimental

4.2.1 Synthesis and characterization: $SrLa_xFe_{12-x}O_{19}$

Synthesis of strontium hexaferrite nanoparticles was accomplished in an aqueous reaction matrix containing ferric nitrate nonahydrate, strontium nitrate, lanthanum nitrate hexahydrate and citric acid monohydrate as discussed in chapter 2. XRD, FTIR, SEM and VSM have been used to study the effects of substitution on various properties.

4.3 Results and discussion

4.3.1 Structural analysis

4.3.1.1 X-ray diffraction

The X-ray diffraction patterns of La^{3+} doped strontium ferrite powder calcinated at 900°C (4h) have been presented in Figure 4.1(a-f). The thermal analysis (section 3.3.1) confirms that the formation of pure hexaferrite phase has been occurred between 900-1200°C. Also it has been found that the properties have improved with increase in calcination temperature and the optimum results obtained for the sample calcinated at 1200°C. When we imposed these conditions on doped hexaferrite materials we have found that, although high calcination improve the structural properties but it dilutes the morphology and magnetic behavior of the materials. To overcome these problems we have adopted lower calcination temperature to 900°C for the synthesis of doped hexaferrite materials. The XRD

analysis shows the crystalline nanoparticles of $SrFe_{12}O_{19}$ have been obtained with hexagonal structure in all samples. The diffraction pattern of a precursor powder shows the presence of intermediates as shown in Figure 3.3a [95,130].

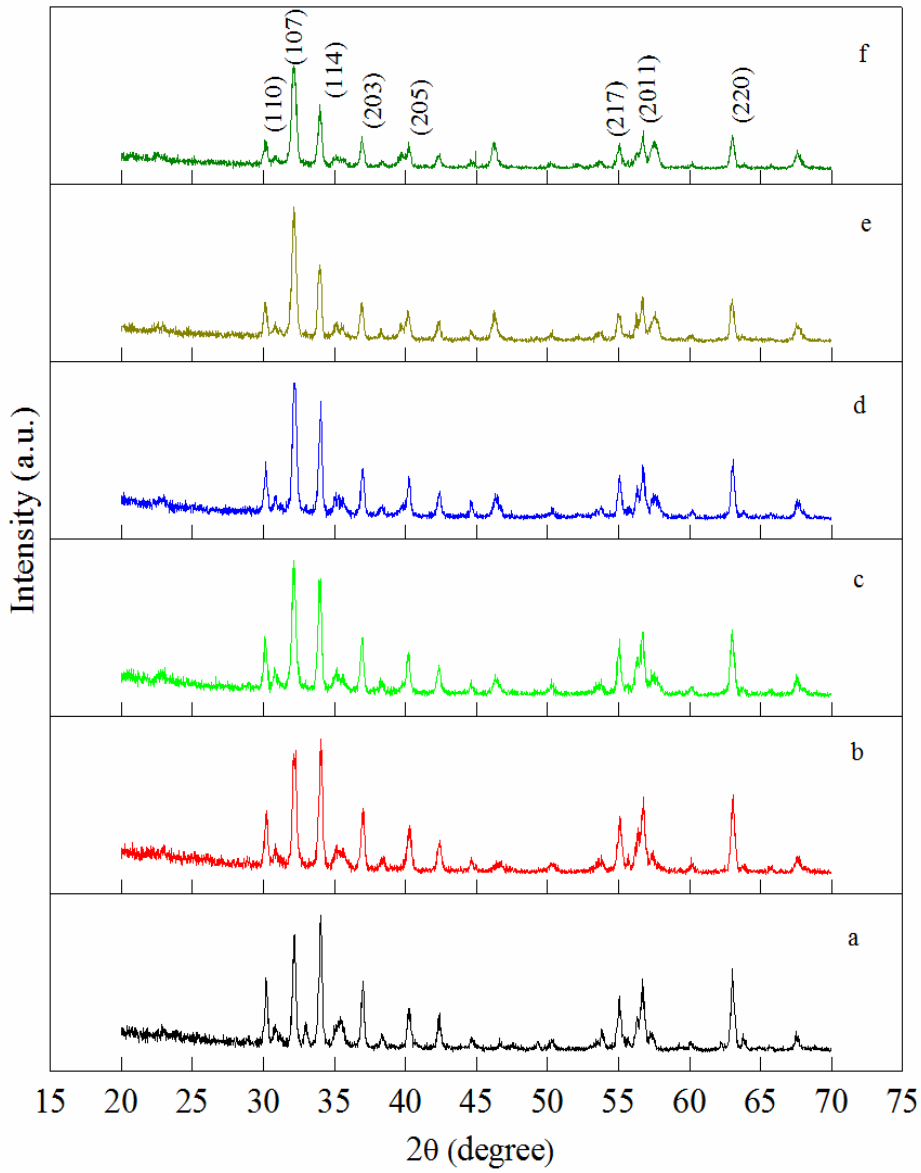

Figure 4.1: X-ray diffraction patterns of $SrLa_xFe_{12-x}O_{19}$ sample calcinated at 900°C (a) x = 0.0, (b) x = 0.23, (c) x = 0.43, (d) x = 0.63, (e) x = 0.83, (f) x = 1.0.

The diffraction peak broadening becomes sharp and intense after the calcination at 900°C which represents the enrichment of crystallinity. All the apparent peaks of

prepared nanoparticles are indexed to (110), (114), (107), (203), (205), (206), (208), and (303) in diffraction pattern is similar to standard (*JCPDS:* 80-1197) diffraction pattern of hexagonal ferrite. However, Figure 4.1a shows the presence of secondary α-Fe_2O_3 (32.9°) phase in diffraction pattern and disappeared thereafter with increase in La^{3+}content in the sample (Figure 4.1b-f). The presence of α-Fe_2O_3 phase in the system reveals the incomplete reaction between Fe^{3+} and Sr^{2+} or low solubility of Sr^{2+} compared to La^{3+} in magnetoplumbite structure [131]. XRD analysis points that the diffraction peak position for La^{3+} doped ferrite exactly appears at same position as for $x = 0$ and the permutation of peak corresponding to (114) and (107) occur at $x \geq 0.43$. The La^{3+}content shows remarkable effect in the diffraction peak intensity for (114) and (107). The diffraction peak intensity of (114) plane decreases with increase in La content while it increases along (107) plane. This increase in peak intensity indicates that the La^{3+} content provokes the formation of ferrite phase along the preferred direction parallel to c-axis along (107) [132]. Preferential orientation (T_C) of crystal growth has been measured by using eq. 14 [133]. The well known classical Scherrer's equation (eq. 8) has been employed to calculate to the values of crystallite size. The obtained crystallite size (*D*) and other parameters are presented in Table 4.1. The *D* size has been found to be decreased with an increase in La^{3+} content (37-25 nm). This decrease in *D* with an increase in doping can be explained on the basis of bond energy or crystallization of doped hexaferrite nanoparticles. The growth or crystallization of ferrite nanoparticles is depends upon the bond formation energy between incorporated metal ions and oxygen ions *i.e.* the bond energy of La^{3+} -O^{2-}. The bond energy of La^{3+} -O^{2-} is higher than that of Fe^{3+} -O^{2-}. Now the La^{3+} ions need more energy to enter into the crystal lattice for the bond formation or in other words substituted ferrite require more energy for the crystallization and growth of nanoparticles [134]. The same reason has been responsible for decrease in c parameter. The crystallite size is a key indicator to achieve desirable signal to noise ratio. The prepared nanoparticles in the range of 25 to 37 nm increase the number of grains which would increase the SNR of the recording media and the desirable SNR can be used for high density perpendicular recording media [135].

Table 4.1: Summary of Structural Parameters*.

S. No.	2θ (°)		d-Values (Å)		β (°)	I/Imax *100	MI	a (Å)	c (Å)	c/a	D (nm)	S	D_x	P (%)	T_C
	Standard	Observed	Standard	calculated											
x = 0	32.35	32.16	2.76	2.77	0.22	84	(107)	5.91	23.18	3.92	37.56	31.82	5.01	0.47	0.98
	34.19	34.02	2.61	2.63	0.21	100	(114)				38.09	31.38			1.01
x = 0.23	32.35	32.18	2.76	2.77	0.27	89	(107)	5.90	23.08	3.91	30.61	37.51	5.22	0.49	1.00
	34.19	34.03	2.61	2.63	0.24	100	(114)				34.60	33.19			0.99
x = 0.43	32.35	32.14	2.76	2.78	0.28	100	(107)	5.92	23.16	3.91	29.51	38.35	5.30	0.50	0.97
	34.19	33.97	2.61	2.63	0.23	84	(114)				36.10	31.34			1.02
x = 0.63	32.35	32.18	2.76	2.77	0.29	100	(107)	5.92	23.10	3.90	28.49	39.10	5.38	0.52	0.99
	34.19	34.02	2.61	2.63	0.22	86	(114)				37.74	29.51			1.00
x = 0.83	32.35	32.14	2.76	2.78	0.30	100	(107)	5.93	23.14	3.90	27.54	40.02	5.44	0.54	0.95
	34.19	33.96	2.61	2.63	0.24	80	(114)				34.59	31.91			1.04
x = 1.0	32.35	32.14	2.76	2.78	0.32	100	(107)	5.92	23.18	3.91	25.82	41.93	5.54	0.55	0.84
	34.19	33.98	2.61	2.63	0.26	64	(114)				31.93	33.90			1.15

* Braggs angle (2θ)

Interplaner spacing (d)

FWHM (β)

Intensity (I)

Miller indices (MI)

Lattice constant (a,c)

Crystallite size (D)

Surface area (S)

X-ray density (D_x)

Porosity (P)

Texture coefficient (T_C)

4.3.1.2 Mid-Infrared spectral region analysis

The infrared absorption spectra provide detailed information about the structural changes *i.e.* the possible intermediates during calcinations. The FTIR transmittance spectra of a precursor and heat treated samples at temperature 900°C (range 4000-400 cm^{-1}) have been shown in Figure 4.2.

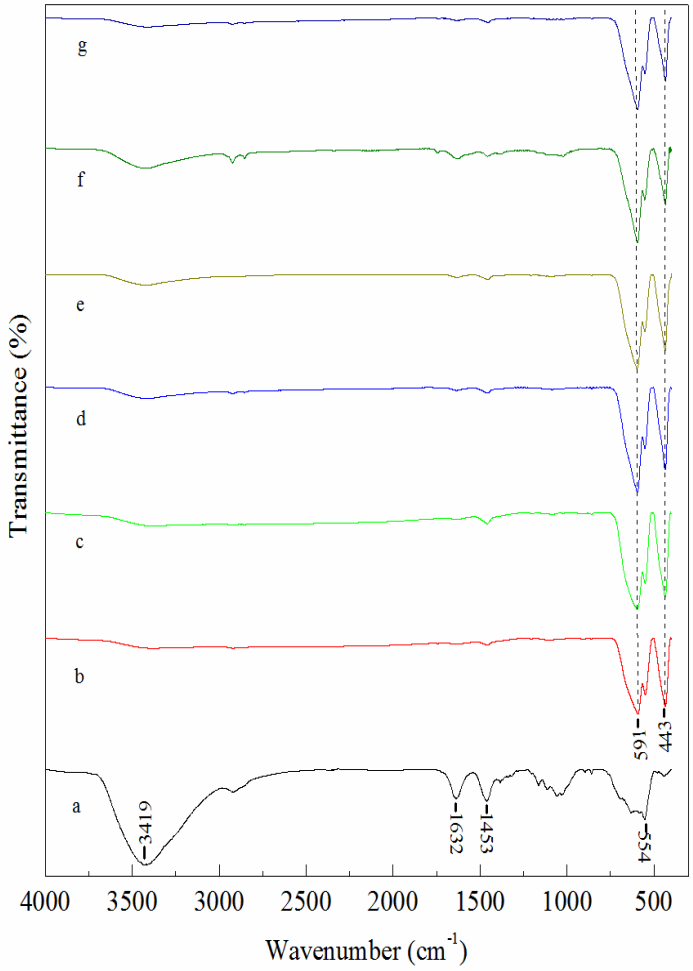

Figure 4.2: Mid-IR spectra of $SrLa_xFe_{12-x}O_{19}$ (a) precursor powder and sample calcinated at 900°C, (b) x = 0.0, (c) x = 0.23, (d) x = 0.43, (e) x = 0.63, (f) x = 0.83, (g) x = 1.0.

The spectrum of precursor (Figure 4.2a) shows the broad absorption bands in the range 3200-3270 cm^{-1}. The absorption band in this range can be ascribed to (O-H) hydroxyl group of citric acid [107,136]. The characteristic bands near 858.82 and

1384.39 cm^{-1} are endorsed to stretching and bending vibrations of NO_3^- respectively [108,137]. The kinks at 2916.52 cm^{-1} in the spectrum is due to the absorbed moisture from the atmosphere indicating the hydroscopic nature of precursor powder [138]. The infrared absorption spectra of samples calcinated at 900°C (4h) for different compositions shows that the absorption band corresponding to O-H stretching still persist, however becomes very weak (Figure 4.2b-g). The characteristic bands related to iron oxide in the range 400-800 cm^{-1} (Figure 4.2a) have disappeared in Figure 4.2b-g and new set of completely resolved bands are appeared at 435.05, 551.04 and 594.26 cm^{-1}. This appearance of fresh bands is attributed to stretching vibration of metal-oxygen bond indicating the formation of hexaferrite [109,137,139].

4.3.2 Morphology of La^{3+}doped strontium ferrite nanoparticles

Micrographs of precursor powder (uncalcinated), pure compound and samples with dopant La^{3+} heat treated at 900°C are exhibited in Figure 4.3(a-d).

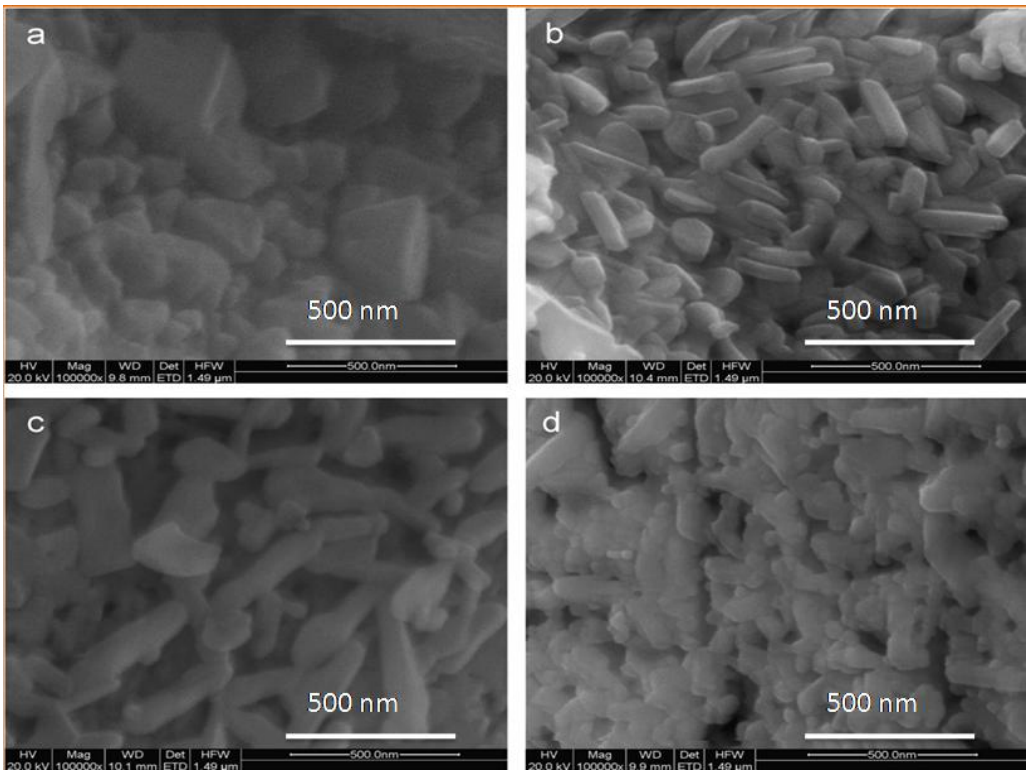

Figure 4.3: SEM micrographs of $SrLa_xFe_{12-x}O_{19}$ (a) precursor powder, (b) x = 0.0, (c) x = 0.63, (d) x = 1.0.

From the micrograph (Figure 4.3a), it is observed that the precursor powder is showing uneven distribution of particles and non-uniformity. After the calcination at 900°C, nanoparticles with plate or needle like structure have been formed in the case of pure composition (Figure 4.3b). It is induced from the Figure 4.3(c-d) that the morphology of samples prepared with La content retards the grain growth and the sample exhibits porous and agglomerated microstructure. The ignition of sample causes evolution of large amount of gases during combustion or decomposition process and interactions between neighboring magnetic particles has been responsible for high porosity and agglomeration respectively (Figure 4.3c-d) [116,140,141]. Although, all the properties such as structural and magnetic properties are showing enhancement in some or other way, morphology of the sample after La doping is showing deterioration in morphology and uniformity of the sample. It has been observed from the Figure 4.3d that the prepared sample after $x = 0.63$ become porous and it drastically affect the coercivity of the materials. Therefore, the change in morphology does not mean the degradation of the sample. This is because the incorporation of rare earth elements for the ferrite phase formation due to larger ionic radii than $Fe^{3+}$and internal stress causes hindrance to the grain growth.

4.3.3 Magnetic analysis

The magnetic parameters have been measured from hysteresis loop [142]. It is seen from the Figure 4.4 that the magnetization (*M*) value decreases with increase in La^{3+} content, while coercivity value increases up to $x = 0.63$ and then decreases (Table 4.2). *M* value is larger for pure $SrFe_{12}O_{19}$ as compared to La^{3+} doped ferrite but still smaller than the results reported by Jacobo *et al.* 2010, which is endorsed to the occurrence of α-Fe_2O_3 phase [143]. The decrease of magnetization can be explained on the basis of exchange interaction, site occupation, spin canting and valence state change from high spin to low spin. The value of *M* is closely related to concentration of La^{3+} *i.e.* magnetization decreases with increase of La^{3+}. The La^{3+} has zero magnetic moment and preferentially occupies octahedral spin up crystallographic site. The site occupation of Fe^{3+} ($5\mu_B$) by La^{3+} reduces the number of magnetic ion and therefore the net magnetic moment decreases which results in reducing the strength of

superexchange interactions of Fe^{3+}-O^{2-}-Fe^{3+}. Also the difference in ionic radii (La^{3+} 1.22 Å and Fe^{3+} 0.63 Å ions) increases the distance between magnetic ions which decreases the Fe^{3+}-Fe^{3+} interactions subsequently causes a decrease in magnetization with the increase of La^{3+} content [144].

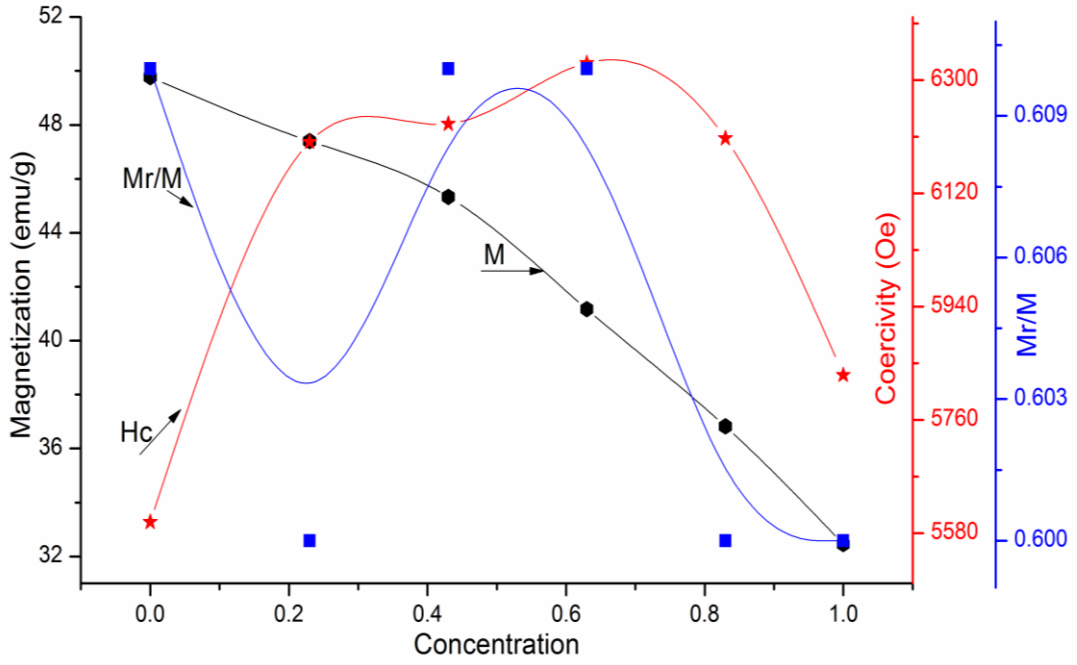

Figure 4.4: Variation of *M*, H_C and *Mr/M* for $SrLa_xFe_{12-x}O_{19}$ at different La^{3+} concentration.

Moreover, in addition to these effects the substitution of rare earth element in ferrite system causes; an environmental distortion, cationic vacancies, as well as it disturb the collinear ferrimagnetic order. Ounnunkad has proposed that the La^{3+} content produces cationic vacancies which arises the spin canting effect resulting in a lowering *M* [145]. The coercivity value (H_C) for single domain nanoparticles has been determined by magnetization and magnetocrystalline anisotropy constant [121,146]. It is observed that coercivity value increases with increase in '*x*' and the maximum value is 6326.94 Oe at $x = 0.63$. H_C is directly proportional to anisotropy constant and results are in accordance with the concentration of La^{3+}. As mentioned above, La^{3+} ions lead the conversion of high spin to low spin state and force iron ions to migrate

towards tetrahedral site. The formation of any low spin iron ions on tetrahedral site during processing preferentially occupy 2a octahedral site [147]. As a result, the number of Fe^{2+} ions on octahedral site increases with increase in La^{3+} content and maximum for x = 0.63. The Fe^{2+} ions enhance the coercivity value due to strong magnetocrystalline anisotropy of Fe^{2+} on 2a site [145,147]. On the other hand, beyond x = 0.63, the coercivity value found to be decrease. This decrease may be attributed to abundance of Fe^{2+} ions and expected to destroy the regular atomic arrangement of Fe^{3+} with an increase of porosity with La^{3+} content. This leads to the dilution of magnetic properties due to presence of pores in the La^{3+} doped samples [148]. The extrinsic parameter H_C has been significantly affected by particle morphology and varies inversely on grain size. Larger the grain size, fewer will be grain boundaries which in turn act as pinning sites for the magnetic domain wall movement. As x increases, grain size became smaller and results are consistent with XRD data (section 4.3.1.1). The reverse magnetic field for the demagnetization of the nanoparticles can be interpreted in relation with domain rotation, where the smaller grain sizes have lesser domain wall movement. Consequently, high coercivity is expected for smaller grain size.

Table 4.2: Values of magnetization, coercivity and squareness ratio for $SrLa_xFe_{12-x}O_{19}$ sample.

$SrLa_xFe_{12-x}O_{19}$	x = 0.0	x = 0.23	x = 0.43	x = 0.63	x = 0.83	x = 1.0
***M* (emu/g)**	49.77	47.40	45.33	41.17	36.82	32.46
H_C (Oe)	5597.35	6201.55	6230.05	6326.94	6207.25	5831.05
Mr/M	0.61	0.60	0.61	0.61	0.60	0.60

The remanence is the magnetization left behind in samples after the removal of external applied field. The magnitude of this remanence can be calculated from the hysteresis loop at the intersections of the loop with the vertical magnetization axis. The SQR of La^{3+} doped hexaferrite samples lies in the range ~ 0.60±0.1. According to

Stoner–Wolfarth model, the squareness ratio of single domain, non interacting particles is *Mr/M* = 0.5. However, nanoparticles of hard magnetic materials usually exhibit large squareness. The present SQR values (in the range of 0.60) are preferred in high density recording media. The variation of *Mr/M* with the concentration of La^{3+} is consistent with the morphological results where increase in SQR ratio is due to the improvement of coercivity value and the hindrance of the grain growth at higher concentration is responsible for the decrement.

4.4 Conclusions

Lanthanum substituted strontium hexaferrite nanoparticles have been successfully prepared from citrate precursor technique. Structural analysis confirms the formation of magnetoplumbite phase and obtained in the range of 31 to 38 nm. The preheating of prepared samples at 500°C for 5h is a key point for the formation of ultrafine nanoparticles because preheating of the precursor prevents the formation of (α-Fe_2O_3) intermediate phases. However, the presence of α-Fe_2O_3 in the system even after the final calcination indicates that the reaction process requires high and longer calcination temperature and time for complete conversion to hexagonal structure. New frequency bands at 435.05, 551.04 and 594.26 cm^{-1} have been observed indicating the formation of hexaferrite due to presence of stretching vibration of metal-oxygen bond. Sample calcinated at 900°C shows plate or needle like microstructure. As the concentration of La content increases particles exhibits porous and agglomerated structure. *M* values decrease with increasing La^{3+} content whereas coercivity values have been found to increase up to $x = 0.63$ after then decreases.

CHAPTER V

Synthesis and Characterization of Nd^{3+} doped Strontium Hexaferrite Nanoparticles: $SrNd_xFe_{12-x}O_{19}$

5.1 Introduction

Hexagonal ferrite $MFe_{12}O_{19}$ (M = Sr, Ba, Pb) materials with magnetoplumbite structure have been extensively used in modern technology applications due to appropriate properties including perfect mechanical, chemical and thermal stability [114,149]. After the discovery by Philips in the 1950s, M-type strontium hexaferrite have been the subject of interest of many researchers for magnetic recording media, telecommunications equipment, injection moulded pieces, plastoferrite, color imaging, ferrofluids as well as permanent magnets [85,143,150-152]. The exploitation of electromagnetic interference and environmental pollution encouraged for the development of electromagnetic attenuation materials (EAM) [153]. The nanoparticles with pyramidal and hexagonal plate like structure can be used as shielding materials to minimize the electromagnetic interference (EMI) [154]. The structures of hexaferrites are classified into five categories on the basis of chemical and crystalline structure *viz.* M-type or $SrFe_{12}O_{19}$, W-type or $SrMe_2Fe_{16}O_{27}$, Y-type or $SrMe_2Fe_{12}O_{22}$, X-type or $Sr_2Me_2Fe_{28}O_{46}$ and Z-type or $Sr_2Me_2Fe_{24}O_{41}$. The crystal structure of magnetoplumbite unit cell of the M-type hexagonal ferrite is combination of two structural blocks stacked along the c-axis consisting of 10 hexagonally closed-packed oxygen layers: RSR*S*. The S and R block stands for spinal and hexagonal structure. R* and S* are the blocks obtained by 180° rotation of R and S with respect to c-axis having equivalent atomic arrangements [154,155]. $SrFe_{12}O_{19}$ contains 64 ions per unit cell on 11 different sites (space group: $P6_3/mmc$). The Fe^{3+} ions are distributed over five distinct crystallographic sites, three octahedral sites (12k, 2a, $4f_2$), one tetrahedral site ($4f_1$) and trigonal bipyramidal site (2b) [156,157]. These crystallographic sites are coupled with O^{2-} ions to form collinear ferrimagnetic order and superexchange interaction between Fe^{3+}-O^{2-}-Fe^{3+}. A significant improvement in various properties for hexaferrite have been achieved by altering the substitution cations from metal ion to rare earth elements on the Fe^{3+} or Sr^{2+} sites or both and can be controlled by varying the size and shape of the particles. Numbers of researchers have reported that the rare earth elements (La^{3+}, Nd^{3+}, Sm^{3+} and Gd^{3+}) act as inhibiting agent for the grain growth and show enhancement in various properties [158]. Low solubility of the rare earth elements in hexaferrite lattice leads to the

formation of secondary phases in the system. However, the octahedral site preference of the rare earth elements and the difference in ionic radii of rare earth elements with respect to Fe^{3+} are expected to enhance the magnetocrystalline anisotropy due to the variation of the superexchange interaction [101,159].

An effort has been made to increase magnetocrystalline anisotropy and the solubility of rare earth elements in hexaferrite lattice under the optimum conditions in this work. The purpose of this work is to study the effects of substitution on the phase formation, crystallite size, lattice parameters, strain, porosity, electrical behavior and magnetic parameters. The outcomes of Nd^{3+} doped M-type hexaferrite have been presented and discussed in detail. In the work reported by Luo 2012 [160] coprecipitation technique has been opted for the synthesis of Nd^{3+} doped ferrite and structural, compositional and magnetic properties have been discussed. However, in the present work, the incorporation of Nd^{3+} in strontium hexaferrite and the influence of low soluble rare earth element on the magnetic properties have been studied.

5.2 Experimental

5.2.1 Synthesis and characterization: $SrNd_xFe_{12-x}O_{19}$

$SrNd_xFe_{12-x}O_{19}$ (x = 0.0, 0.23, 0.43, 0.63, 0.83 and 1.0) were prepared through citrate precursor route using highly pure reagent namely strontium nitrate, ferric nitrate nonahydrate, neodymium nitrate hexahydrate, citric acid monohydrate and ammonium solution (25%) as discussed in chapter 2. XRD, FTIR, SEM and VSM have been used to study the effects of substitution on various properties.

5.3 Results and discussion

5.3.1 Structural analysis

5.3.1.1 X-ray diffraction

$SrNd_xFe_{12-x}O_{19}$ calcinated at 900°C has been examined by versatile and non-destructive powder X-ray diffraction technique and presented in Figure 5.1. The structural analysis confirms that pure strontium ferrite exhibited crystalline ferrite phase with undesired diffraction peak related to hematite at 33.21°, Figure 5.1a. The diffraction peaks (110), (107), (114), (203), (205) and (206) of pure ferrite perfectly

matches with that of standard hexagonal ferrite (JCPDS: 84-1531, 80-1197). The intensity of (114) central maxima decreased and increases in the direction parallel to c-axis of the crystal (107) plane with Nd^{3+}content. The full width at half maxima of characteristic peaks became broader indicating the reduction of crystallite size.

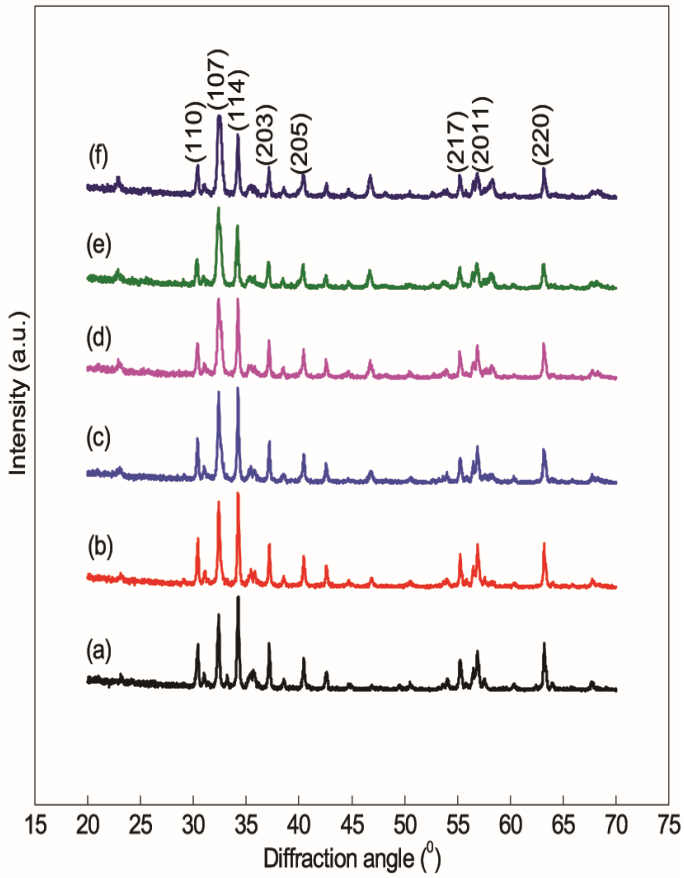

Figure 5.1: X-ray diffraction patterns of $SrNd_xFe_{12-x}O_{19}$ sample calcinated at 900°C (a) x = 0.0, (b) x = 0.23, (c) x = 0.43, (d) x = 0.63, (e) x = 0.83, (f) x = 1.0.

All the apparent peaks for Nd^{3+} doped ferrite (Figure 5.1b-f) exactly appears at same position and the partial substitution of Fe^{3+} by Nd^{3+} reveals the formation of single phase nanocrystalline materials without any intermediates. This indicates that the Nd^{3+} ions enter into the magnetoplumbite structure without disturbing the host lattice of strontium ferrite. It is clear from XRD data that the Fe^{3+}/Sr^{2+} ratio plays an

important role in the formation of pure strontium ferrite. The diffraction pattern of prepared nanoparticles with molar ratio Fe^{3+}/Sr^{2+}=12 calcinated at 900°C for 4h in air atmosphere shows undersired α-Fe_2O_3 residuals (Figure 5.1a, x = 0.0) which apparently disappeared after Nd^{3+} doping. The existence of α-Fe_2O_3 residuals in the system is usually due to the incomplete reaction or mixing of starting materials on ionic levels between Fe^{3+} and Sr^{2+} under particular synthesis condition. However, the crystal structure of α-Fe_2O_3 is similar to $FTiO_3$ structure which belongs to trigonal crystal structure having orthorhombic hexahedron crystal cell and is difficult to transform in hexaferrite phase [161]. It can be concluded from the structural analysis that the pure hexaferrite system needs high calcination temperature for complete crystallization and the iron deficient non-stoichiometric composition leads to the formation of pure product. The crystallite size D, strain η and specific surface area S, have been calculated using eq. (8-10) [162-165]. The crystallite size for different Nd^{3+} content has been calculated using well known Scherrer's equation (1) and listed in Table 5.1. The crystallite size has been found to decrease with the substitution of larger ionic radii, Nd^{3+}. This might happen mainly due to two reasons: (i) strain produced in the unit cell [166] (ii) diffusion inhibition of rare-earth element in magnetoplumbite structure [167]. The lattice parameters (a and c) have been calculated from X-ray data using eq. 11. The calculated parameters as functions of Nd^{3+} concentration are given in Table 5.1. It can be seen that values of 'a' nearly unchanged whereas 'c' slightly decreases with increase in Nd^{3+} content. Mozaffari *et al.* have reported that there should be increase in lattice parameter with addition of higher ionic radii element [144]. But in the present study, the lattice parameter has been found to decrease when Nd^{3+} is substituted in Fe^{3+}. This contraction of crystal axis (c/a) ratio is mainly due to chemical composition, defects, strain and suppression effect of Nd^{3+} in strontium ferrite. The bulk density D_b has been calculated from volume ($\pi r^2 d$) and mass (m) of pellet having thickness (d) and radius r. Porosity (P) and X-ray density (D_x) has been measured using the expression given in eq. (12,13) [168-170]. The calculated values of D_x, D_b and P are given in Table 5.1. The incorporation of Nd^{3+} in host lattice gives significant increase in X-ray density as observed.

Table 5.1: Summary of Structural Parameters*.

S. No.	2θ (°)		d-Values (Å)		*β* (°)	I/Imax *100	MI	a (Å)	c (Å)	c/a	D (nm)	S	*Dx*	*P* (%)	T_C
	Standard	Observed	Standard	Calculated											
***x* = 0**	32.35	32.38	2.76	2.76	0.26	84	(107)	5.91	23.18	3.92	31.80	37.58	5.01	0.48	0.97
	34.19	34.24	2.61	2.61	0.23	100	(114)				36.12	33.09			1.02
***x* = 0.23**	32.35	32.41	2.76	2.75	0.25	49	(107)	5.87	22.99	3.91	33.07	34.67	5.23	0.50	0.72
	34.19	34.24	2.61	2.61	0.22	100	(114)				37.76	30.37			1.27
***x* = 0.43**	32.35	32.42	2.76	2.75	0.26	93	(107)	5.88	22.98	3.90	31.80	35.50	5.31	0.51	1.02
	34.19	33.23	2.61	2.61	0.19	100	(114)				43.73	25.82			0.97
***x* = 0.63**	32.35	32.45	2.76	2.75	0.48	100	(107)	5.88	22.94	3.90	17.23	64.45	5.40	0.53	1.07
	34.19	34.22	2.61	2.61	0.21	98	(114)				39.56	28.07			0.92
***x* = 0.83**	32.35	32.42	2.76	2.75	0.49	100	(107)	5.89	22.96	3.90	16.87	65.06	5.46	0.54	1.18
	34.19	33.16	2.61	2.62	0.25	78	(114)				33.23	33.04			0.81
***x* = 1.0**	32.35	32.48	2.76	2.75	0.51	100	(107)	5.88	22.92	3.89	16.21	66.45	5.56	0.55	1.19
	34.19	33.22	2.61	2.61	0.26	77	(114)				31.95	33.72			0.80

The X-ray density is directly related to molecular weight and varies inversely with cell volume. The X-ray density increased from 5.01 to 5.56 g/cm^3 with increase in doping concentration. This can be explained on the basis of fact that according to eq. 13, D_x is inversely proportional to V_{cell} which is again directly proportional to c parameter. Thus decrease in *c*-value with doping concentration and larger molecular weights of Nd^{3+} doped sample are mainly responsible for the same [91]. The porosity of prepared samples increases with decrease in bulk density is mainly due to low density of Nd^{3+} (7.00 g/cm^3) as compared to Fe^{3+} (7.86 g/cm^3). The lower D_b than the D_x indicates the existence of pores in the samples, which were formed during the preparation and heat treatment causing irregular shape of grains and porosity of strontium ferrite. Microstrain values for the Nd^{3+} substituted ferrite have been calculated using the equation [163]: $\eta = \beta / 2\tan\theta$ and lies in the range of 6.2 x 10^{-3} to 7.37 x 10^{-3}. It has been observed that the lattice strain of hexaferrite system increases with decrease in crystallite size as a function of Nd^{3+} content. For x = 1.0, strain value has been obtained to be positive (tensile strain) and maximum. This may be explained on the basis of ionic radii or lattice contraction; the reduction in crystallite size probably decreases the crystal axis ratio thereby increasing tensile strain in the system. An interesting observation has also been noticed in diffraction patterns where the peak shifts to higher Bragg's angle. The substitution of Nd^{3+} leads to the change in the peak intensities and β of diffraction peaks in comparison to the pure strontium ferrite and dually credited to crystallite size and lattice strain. The diffraction patterns show that the XRD peaks shift towards the lower d-spacing value indicating the contraction in unit cell due to strain in the system [171]. These results suggest that the Nd^{3+} is systematically entered in the host lattice in place of Fe^{3+} radii.

5.3.1.2 Mid-Infrared spectral region analysis

Fourier transform infrared spectroscopy (Figure 5.2) gives qualitative and quantitative information about chemical and molecular bond structure in materials as well

as the identification and detection of impurities during calcination or incorporation of foreign atom in the parent compound.

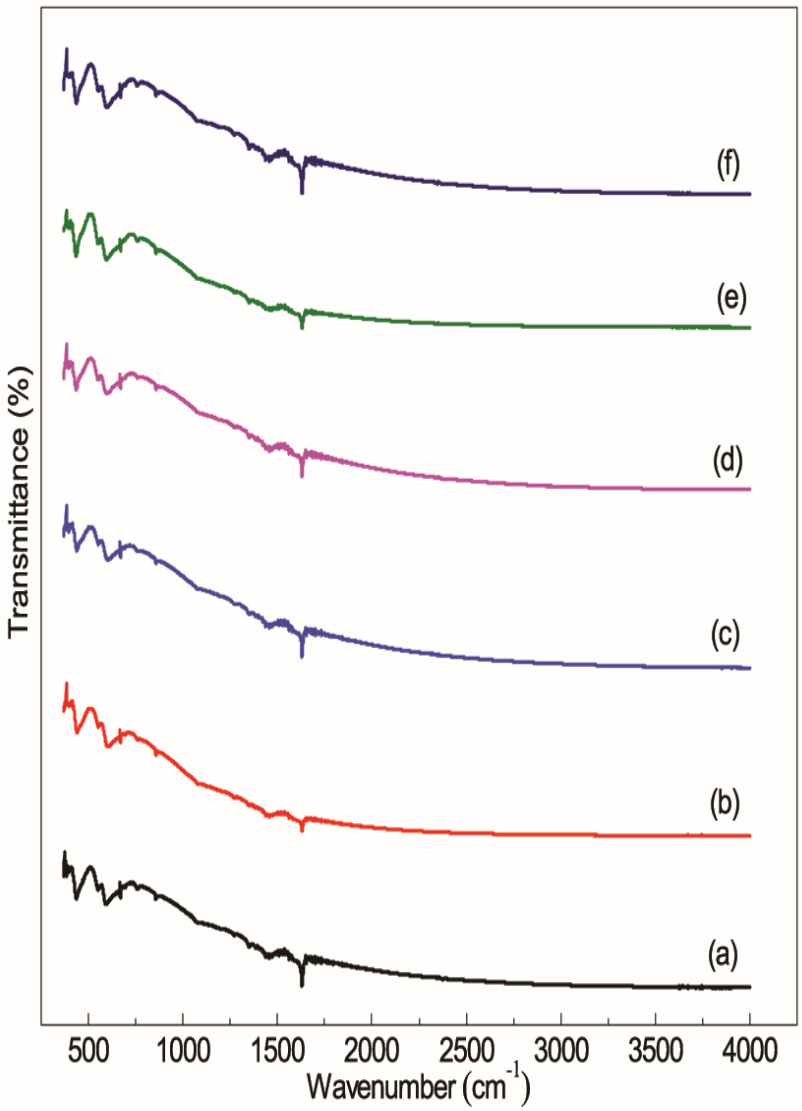

Figure 5.2: Mid-IR spectra of $SrNd_xFe_{12-x}O_{19}$ sample calcinated at 900°C (a) x = 0.0, (b) x = 0.23, (c) x = 0.43, (d) x = 0.63, (e) x = 0.83, (f) x = 1.0.

Considering this fact, Nd^{3+} doped strontium hexaferrite calcinated at 900°C in the range 4000-400 cm^{-1} have been analyzed. The frequency bands in the range 430-470 cm^{-1} and 550-580 cm^{-1} are attributed to the lattice vibration of metal ions at octahedral and

tetrahedral sites respectively [172]. The characteristic peaks at 429 cm^{-1} and 588 cm^{-1} corresponds to the stretching vibrations of metal-oxygen bond (Figure 5.2) indicating the formation of hexaferrite [149,173]. No absorption peaks of CO_2^- group and NO_3^- ions have been found after the calcination revealing the completion of redox reaction in which citrate ions act as reductant and nitrate ions as oxidant. The frequency band at 1630 cm^{-1} is assigned to the bending mode of water molecules in the spectra and is due to the moisture absorbed by the samples [138]. Nd^{3+} ions have sturdy octahedral site preference and is expected that substitution of Nd^{3+} alter the band position of octahedral and tetrahedral clusters. The difference in absorption peak position is attributed to the difference in bond length of Fe^{3+}-O^{2-} for octahedral and tetrahedral clusters. The incorporation of Nd^{3+} ions shift the absorption peaks corresponding to octahedral site to higher frequency site which confirms that Nd^{3+} ions occupy the octahedral sites [138,174].

5.3.2 Morphology of Nd^{3+}doped strontium ferrite nanoparticles

The SEM micrographs of Nd^{3+} doped hexaferrite nanoparticles at room temperature have been depicted in Figure 5.3(a-d). From Figure 5.3a, it can be seen that the particles are homogeneous and closely packed throughout the surface of sample. The average crystallite size of pure hexaferrite sample appears to be bigger along with the preeminent structure than doped samples and the crystallite size determined by X-ray diffraction technique respectively. The above facts can be justified on the basis of two different aspects: firstly, due to the suppression effect of rare earth elements in the development of grain growth [167] and secondly, the SEM technique discloses the results of secondary particles rather than the information about primary particles [175]. The microstructures reveal that the morphologies of prepared samples are strongly influenced by the Nd^{3+} content. It can also be seen from Figure 5.3b that with the addition of Nd^{3+} content, the agglomeration starts appearing and also the particles size found to decrease.

The substitution of Nd^{3+} also results in aggregation of nanoparticles for higher compositions due to magnetic interactions between the neighboring particles.

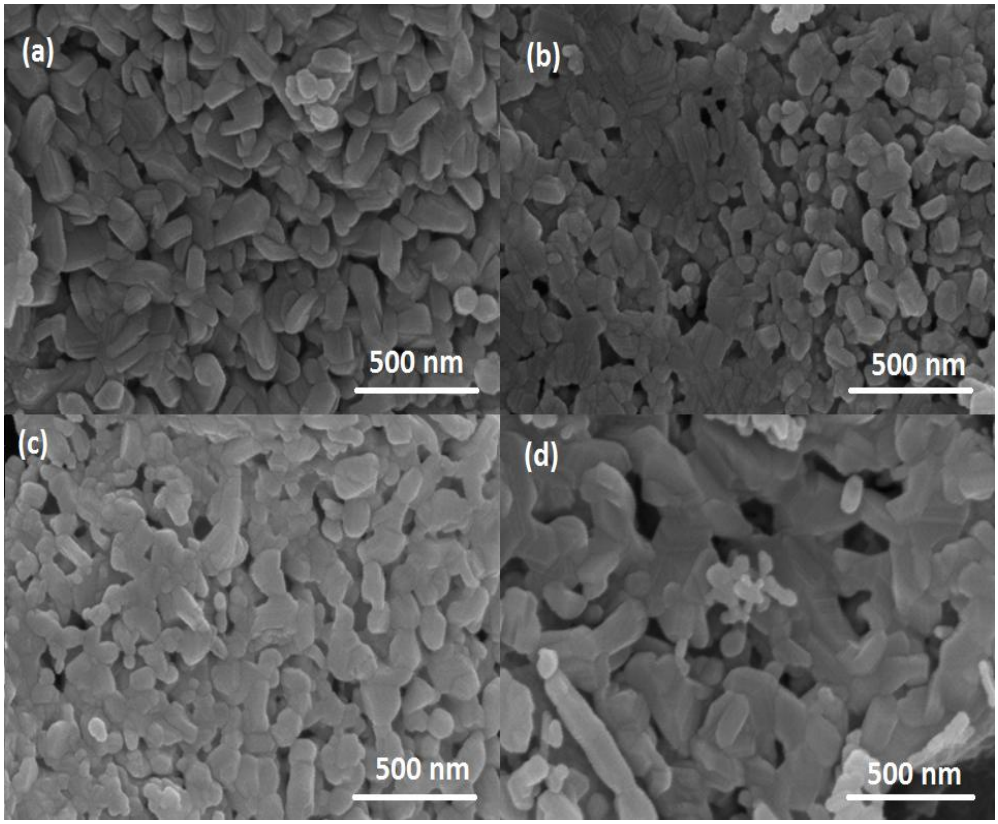

Figure 5.3: Micrographs of $SrNd_xFe_{12-x}O_{19}$ (a) x = 0.0, (b) x = 0.43, (c) x = 0.83, (d) x = 1.0.

The SEM image in Figure 5.3(c,d) shows that the particles exhibit highly porous and agglomerated microstructure [116,176,177]. The deterioration in microstructure does not mean the degradation of the sample. This may be attributed to the incorporation of Nd^{3+} ions in ferrite which causes liberation of large amount of gases during crystallization process. Also the difference in ionic radii between Nd^{3+} and Fe^{3+} and internal stress in the system causes hindrance to the grain growth.

5.3.3 Magnetic analysis

The magnetization (*M*) and coercivity (H_C) values of Nd^{3+} doped strontium ferrite have been measured from the hysteresis curves using VSM [178].

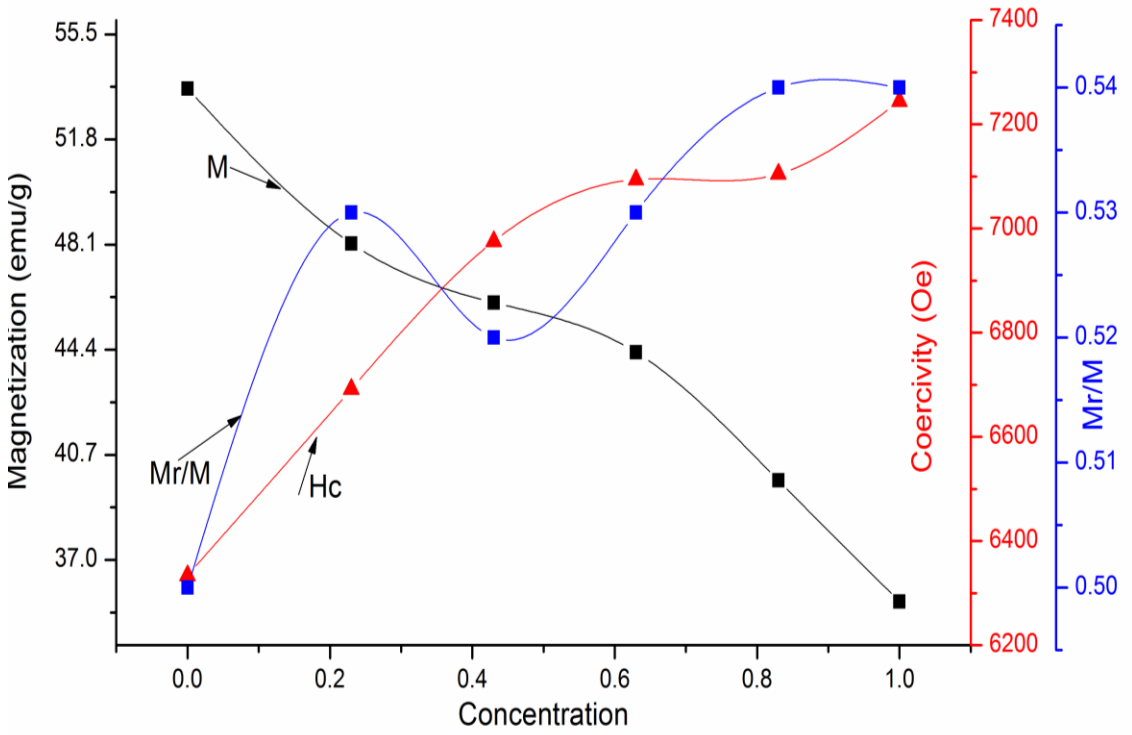

Figure 5.4.1: Variation of *M*, H_C and *Mr/M* for $SrNd_xFe_{12-x}O_{19}$ at different Nd^{3+} concentration.

It has been observed from the Figure 5.4.1 that saturation magnetization decreases while coercivity of strontium ferrite increases when Fe^{3+} ions are substituted by Nd^{3+}. *M* for pure $SrFe_{12}O_{19}$ at $x = 0.0$ is 53.59 emu g^{-1} which is larger than Nd^{3+} doped strontium ferrite but still lower than the result reported [179]. The presence of impurity (α-Fe_2O_3) phase in pure compound as discussed in section 3.1 may contributes in the reduction of *M* value. The intrinsic magnetic properties of M-type hexaferrite have been strongly affected by site occupation of substituted cation, ionic radii, density and valence state

change. This phenomenon has been discussed by means of superexchange interaction. It is known that the M is proportional to magnetic moment of a single particle (m) by the relation $M = \gamma m$, where γ is the volume fraction of the magnetic particles [180]. The substitution of Nd^{3+} for Fe^{3+} ions lead to decrease in density. The decrease in density means the reduction of magnetic dipoles per unit volume and hence, results in drop of M. Nd^{3+} ions generally introduce local strain that probably causes an environmental disorder or non-collinear ferrimagnetic arrangement. Also the difference in ionic radii between Fe^{3+} (0.63 Å) and Nd^{3+} (0.99 Å) increases the distance between magnetic ions and reducing the strength of superexchange interactions. Moreover, the replacement of each Fe^{3+} ($5\mu_B$) by Nd^{3+} ($3\mu_B$) ions result in lowering of M_S by $2\mu_B$. Further, the decrease in M with decreasing crystallite size can also be ascribed to increase in non-collinear magnetic order for various sites as the surface to volume ratio increase [181]. H_C is remarkably enhanced with the substitution of Nd^{3+} (Table 5.2). As shown in Figure 5.4.1, Nd^{3+} increases the coercivity of doped ferrite particles with respect to pure magnetic ferrite particles and sample with maximum Nd^{3+} content shows highest H_C (H_C is increased by about 14.3%).

Table 5.2: Values of magnetization, coercivity and squareness ratio for $SrNd_xFe_{12-x}O_{19}$ sample.

$SrNd_xFe_{12-x}O_{19}$	x = 0.0	x = 0.23	x = 0.43	x = 0.63	x = 0.83	x = 1.0
***M* (emu/g)**	53.59	48.14	46.06	44.31	39.80	35.54
H_C (Oe)	6334.13	6691.55	6975.56	7094.20	7104.70	7244.82
Mr/M	0.50	0.53	0.52	0.53	0.54	0.54

The plausible explanations for an improvement of H_C are crystal size and the magnetocrystalline anisotropy effect of Fe^{2+} [145,147]. The strong stabilization energy of Nd^{3+} for octahedral sites leads to increase in concentration of low spin Fe^{2+} ions at 2a

site. The existence of strong anisotropic Fe^{2+} ions enhanced the magnetocrystalline anisotropy along c-axis. The extrinsic properties of magnetic materials are not only associated with spin carriers but these are also considered to be depend upon microstructural defects, grain size and shape. The coercivity is in direct proportion to energy barrier from the theory of single domain nanoparticles. The energy barrier is the minimum applied field required for spin reversal of the nanoparticles in the direction of magnetic field orientation and can be expressed as eq. 15 [178,182]. The order of estimated energy barrier has been calculated using Stoner-Wohlfarth theory and is highest for $x = 1.0$.

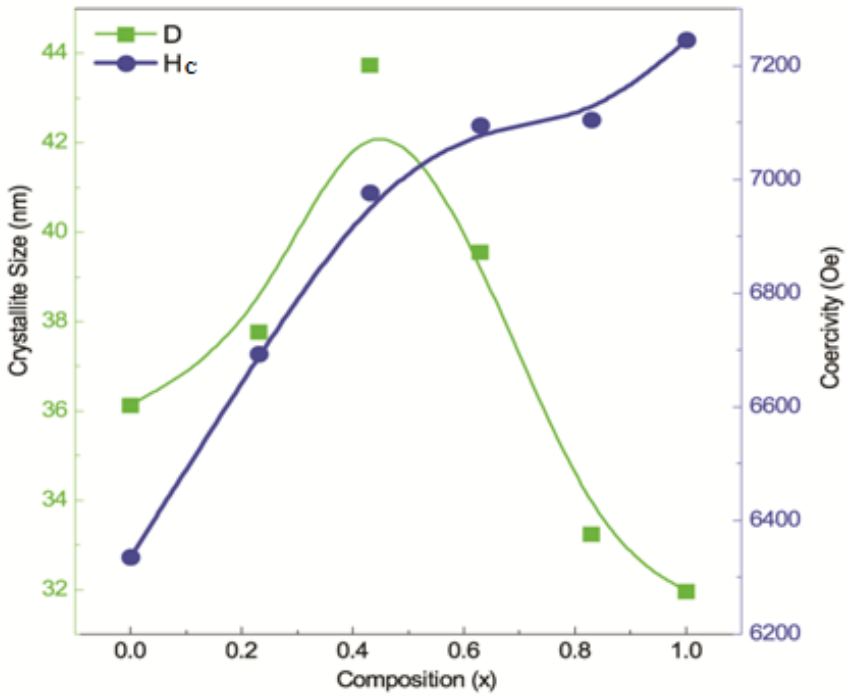

Figure 5.4.2: The coercivity of $SrNd_xFe_{12-x}O_{19}$ as a function of crystallite size.

The improvement in the coercivity is analogous to anisotropy energy and is considered to be due to increase in anisotropic Fe^{2+} ions. Therefore, a strong demagnetizing field is required to overcome the magnetocrystalline anisotropic energy barrier that results in

high coercivity. The variation of coercivity with crystallite size has been depicted in Figure 5.4.2. The coercivity results found are inversely proportional to the grain size and seem to be associated with the surface area. Smaller the grain size, larger will the grain boundaries and act as pinning sites for the magnetic domain wall movement. The decrease in crystallite size with the increase in density of Nd^{3+} leads to impede the rotation of magnetization because the grain boundaries act as pinning center [183] and hence the particles can exhibit the hard magnetic characteristics. It is clear from the Fig. 5.4.1 that SQR value increases with increase in Nd^{3+} content, where SQR is the ease with which the direction of magnetization reorients their magnetic spins to the nearest easy axis after the removal of applied magnetic field. The values of the remanence ratio of the prepared samples are in the range 0.50-0.54 which confirmed the single domain range.

5.4 Conclusions

The citrate precursor using the sol to gel route followed by gel to crystallization come out to be economical, convenient and versatile for mass production of homogeneous materials with controlled grain size and enhanced reaction activity. The nanoparticles of Nd^{3+} doped ferrite with hexagonal crystal structure having crystallite size in the range 31-36 nm can be used to minimize the EMI and aid to achieve desired signal to noise ratio for high density recording media. The introduction of Nd^{3+} ions in hexaferrite lattice have been confirmed from mid-infrared analysis in which the substitution results in shift of octahedral absorption band to higher frequency. The SEM results point that the crystallite size of pure hexaferrite are found to larger than doped hexaferrite nanoparticles. The incorporation of Nd^{3+} in a ferrite lattice results in aggregation of particles. However, Nd^{3+} ions show significant improvement in coercivity and the explanation has been given on the basis of abundance of strong magnetocrystalline anisotropy, Fe^{2+} ions on 2a-site distribution.

CHAPTER VI

Synthesis and Characterization of Ce^{3+} doped Strontium Hexaferrite Nanoparticles: $SrCe_xFe_{12-x}O_{19}$

6.1 Introduction

Strontium hexaferrite (SrM) ferrites with magnetoplumbite structure are promising candidates for the fabrication of multi-layer chip inductors because of the large coercivity which is mainly attributed to its high magnetoanisotropy [184]. The multi-layer chip inductors are the significant surface mounting devices and can be produced by interleaving ferrite layers with internal conductors (such as silver) and then co-fire them [185]. The surface mounting devices have growing interest in SrM ferrites for the development of diminutive products as well as the component track linking. Ferrites are magnetic as well as dielectric materials with desirable dielectric properties in hyper frequency range along with high cut off frequency up to the GHz range make these materials useful for chip inductors. However, the electromagnetic interference is the electrical disturbance in circuit due to electromagnetic induction caused by external source results in the exploitation of electromagnetic interference and environmental pollution in wireless communications encouraged for the development of electromagnetic attenuation materials, EAM [186]. It has been suggested that the problem of undesired electromagnetic signals can be sort out with electromagnetic absorbing materials. After the discovery of ferrite by Philips in the 1950s lot of research has been done by number of researchers in the interest for the improvement of the electromagnetic absorption properties of ferrite materials. Strontium ferrite nanoparticles with pyramidal or plate like structures having hard magnetic characteristics can be used as shielding materials and are extensively studied as absorbing materials. The structures of hexaferrites are classified into different categories on the basis of chemical and crystalline structure; M-type or $SrFe_{12}O_{19}$, W-type or $SrMe_2Fe_{16}O_{27}$, Y-type or $SrMe_2Fe_{12}O_{22}$, X-type or $Sr_2Me_2Fe_{28}O_{46}$ and Z-type or $Sr_2Me_2Fe_{24}O_{41}$. $SrFe_{12}O_{19}$, is isomorphous, M-type hexagonal ferrite in which crystallographic sites are coupled by O^{2-} ions to form hexagonal closed packing as well as superexchange interaction between Fe^{3+}-O^{2-}-Fe^{3+} [187] and is often expressed as RSR*S*, where R and S are hexagonal and spinel blocks represents a block of three-oxygen layer with composition $(Sr^{2+}Fe_6^{3+}O_{11})^{2-}$, and S a two oxygen layer block with composition $(Fe_6^{3+}O_8)^{2+}$ respectively; R* and S* are the blocks obtained by 180° rotation of R and S with respect to c-axis having equivalent atomic arrangements.

Moreover, simple way to explain the crystal structure is on the of oxygen layer where it is supposed that the unit cell consisting of two structural blocks or molecules stacked along the c-axis consisting of 10 oxygen layers. Every five oxygen layer one metal ion is replaced by divalent ion, four oxygen layers make one spinel block and five oxygen layers with one metal ions and spinel block make one molecule. Such two molecules make one unit cell [188].

The effects of Ce^{3+} on the structural, morphological and magnetic properties of $SrCe_xFe_{12-x}O_{19}$ nanoparticles have been discussed in this chapter.

6.2 Experimental

6.2.1 Synthesis and characterization: $SrCe_xFe_{12-x}O_{19}$

The chemicals used in the synthesis of $SrCe_xFe_{12-x}O_{19}$ (x = 0.0, 0.23, 0.43, 0.63, 0.83 and 1.0) are strontium nitrate, ferric nitrate nonahydrate, cerium nitrate hexahydrate, citric acid monohydrate and ammonium solution (25%) as discussed in chapter 2. XRD, FTIR, SEM and VSM have been used to study the effects of substitution on various properties.

6.3 Results and discussion

6.3.1 Structural analysis

6.3.1.1 X-ray diffraction

The diffraction patterns of sample calcinated at 900°C for 4h have been shown in Figure 6.1(a-f). The diffraction peaks of calcinated powder reveal that all the peaks are well indexed to standard hexagonal M-type ferrite which confirms the formation. As x increases, extra peaks appear and their intensities increase with x.

The presence of α-Fe_2O_3 phase in the system indicates the incomplete calcination reaction between the intermediates for the formation of ferrite phase. The existence of cerium oxide (28.5°) as a secondary phase indicates that Ce^{3+} ions are not able to enter into the ferrite lattice even at low concentration under these conditions. Also it provokes the growth of secondary phase (Figure 6.1b-f) and the intensity of

main peaks has been found to decrease with an increase of *x*, it confirms that secondary phase has been grown at the expense of ferrite phase.

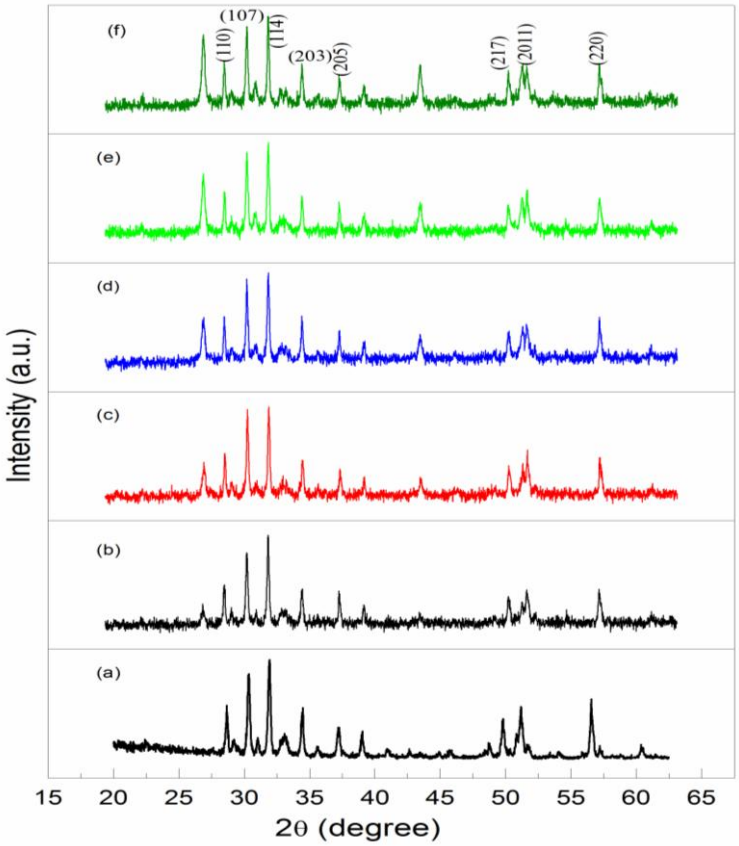

Figure 6.1: X-ray diffraction patterns of $SrCe_xFe_{12-x}O_{19}$ sample calcinated at 900°C (a) x = 0.0, (b) x = 0.23, (c) x = 0.43, (d) x = 0.63, (e) x = 0.83, (f) x = 1.0.

The lattice constant *a*, *c* has been calculated from XRD data using eq. (11). It is seen that the value of *a* is almost constant but the value of *c* decreases with an increase in Ce^{3+} content as shown in Table 6.1. This is due to the suppression effect of superexchange interaction energy and higher bond energy between Ce^{3+} and O^{2-} ions which may be responsible for decrease in lattice parameter even after the substitution of larger ionic radii element Ce^{3+} (1.11 Å) for Fe^{3+} sites [189]. The crystallite size firstly increases with an increase in Ce^{3+} concentration and then decreases thereafter for the most prominent peak (114).

Table 6.1: Summary of Structural Parameters*.

S.No.	2θ (°)		d-Values (Å)		β (°)	I/Imax *100	MI	a (Å)	c (Å)	c/a	D (nm)	S	D_x	P (%)	T_C
	Standard	Observed	Standard	Calculated											
***x* = 0.0**	32.35	32.18	2.76	2.78	0.22	85	(107)	5.92	23.15	3.91	33.0	36.2	5.01	0.404	0.98
	34.19	34.04	2.61	2.63	0.25	100	(114)				37.7	31.7			1.01
***x* = 0.23**	32.35	32.35	2.76	2.76	0.21	80	(107)	5.88	23.05	3.92	39.3	29.26	5.20	0.429	0.95
	34.19	34.22	2.61	2.62	0.19	100	(114)				43.7	26.34			1.04
***x* = 0.43**	32.35	32.41	2.76	2.76	0.19	96	(107)	5.87	23.00	3.91	43.5	25.94	5.31	0.442	1.04
	34.19	34.28	2.61	2.61	0.21	100	(114)				48.4	28.53			0.95
***x* = 0.63**	32.35	32.36	2.76	2.76	0.16	93	(107)	5.88	23.03	3.91	51.6	21.65	5.36	0.450	1.02
	34.19	34.23	2.61	2.62	0.22	100	(114)				37.7	29.64			0.97
***x* = 0.83**	32.35	32.36	2.76	2.76	0.20	89	(107)	5.87	23.04	3.92	41.5	26.62	5.45	0.461	1.00
	34.19	34.24	2.61	2.62	0.20	100	(114)				41.3	26.50			0.99
***x* = 1.0**	32.35	32.37	2.76	2.76	0.18	87	(107)	5.88	23.02	3.91	41.3	26.31	5.52	0.467	0.99
	34.19	33.21	2.61	2.62	0.20	100	(114)				46.1	23.57			1.00

The increase in crystallite size for Ce^{3+} doped samples has been supposed to be due to the growth of a new phase in the sample till x = 0.43 [190]. As the value of x increases (> 0.43) the bond energy Ce^{3+}–O^{2-} come in existence *i.e.* at higher Ce^{3+} concentration system requires large amount of energy to complete crystallization process and grain growth [190,191].

6.3.1.2 Mid-Infrared spectral region analysis

The infrared spectroscopy provides information about chemical and structural changes in ferrite compounds due to change in metal oxygen bond.

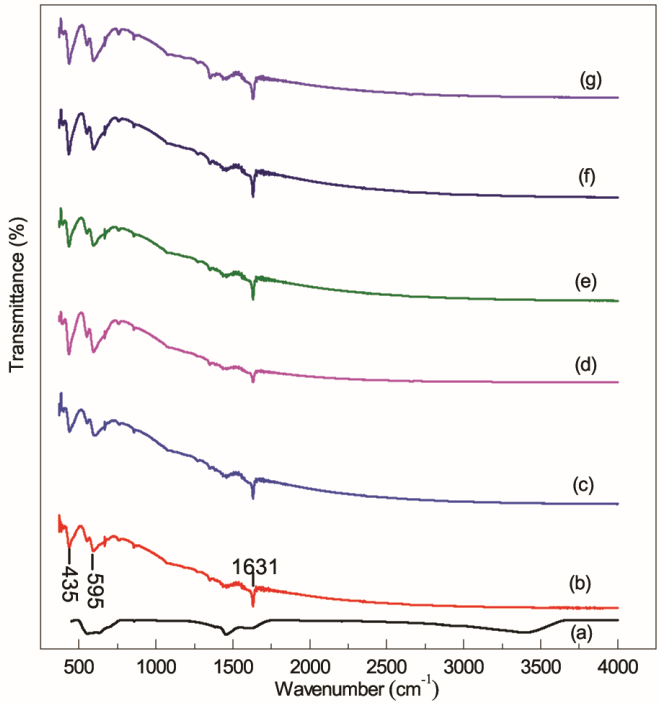

Figure 6.2: Mid-IR spectra of $SrCe_xFe_{12-x}O_{19}$ (a) precursor powder and sample calcinated at 900°C (b) x = 0.0, (c) x = 0.23, (d) x = 0.43, (e) x = 0.63, (f) x = 0.83, (g) x = 1.0.

The alteration in bond length may be attributed for synthesis conditions, heat treatment or inclusion of metal ions in Sr^{2+} or Fe^{3+} crystallographic sites. Mid-IR spectrum of

uncalcinated sample shows dominant peaks in the range 3000-3670 cm^{-1} and 1620 cm^{-1} corresponding to vibrations of hydroxyl and carboxyl group respectively (Figure 6.2a). The characterization band at 858 and 1384 cm^{-1} indicates the stretching vibration of NO_3^- [107,109,192,193]. However, NO_3^- and carboxyl group found to be disappear after calcinations indicates that ions in citrate-nitrate gel are taking part in the redox reaction in which citrate act as reductant and nitrate ions as oxidant. The vibration modes of water molecules at 1630 cm^{-1} has been found even after the calcinations. This is due to the moisture absorbed by the samples which infers the hydroscopic nature of the material. The characteristic bands in the frequency range 435 cm^{-1} and 595 cm^{-1} have been recognized to the vibration of metal oxygen bond at octahedral and tetrahedral sites in Figure 6.2(b-g), respectively [98,109,193,194].

6.3.2 Morphology of Ce^{3+}doped strontium ferrite nanoparticles

The morphologies of the Ce^{3+} doped samples for various concentrations have been shown in Figure 6.3.

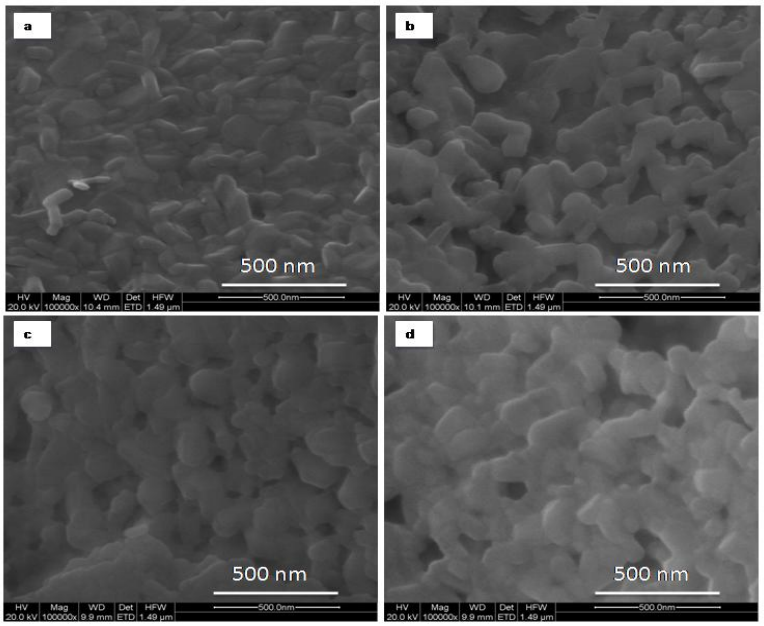

Figure 6.3: Micrographs of $SrCe_xFe_{12-x}O_{19}$ calcinated at 900°C (a) x = 0.0, (b) x = 0.43, (c) x = 0.83, (d) x = 1.0.

It can be seen that the substitution influenced the morphologies of the particles. The Figure 6.3a shows the micrograph of pure strontium ferrite nanoparticles calcined at 900°C. The micrograph clearly shows the hexagonal shaped particles with an average grain size 100-200 nm which is composed of several crystallite of size about 40-50 nm. The image also shows strong aggregation of particles in pure compound due to the interaction between the magnetic particles. With the increase in *x*, calcinated sample become irregular even at low concentration. This may be due to the presence of secondary phases in system and their strength increases with increase in concentration of Ce^{3+} content. The crystallite sizes determined by X-ray diffraction are smaller than average crystallite size calculated from SEM. This is because X-ray diffraction technique provides the information of primary particle size and SEM discloses the results of secondary particles.

6.3.3 Magnetic analysis

The effects of substitution on the magnetization *M* and coercivity H_C values have been presented in Figure 6.4.

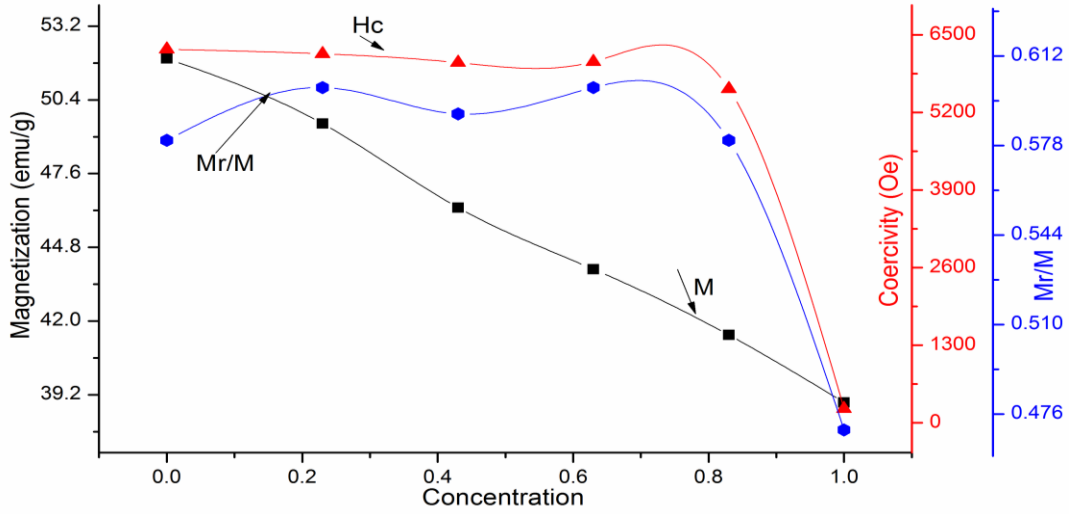

Figure 6.4: Variation of *M*, H_C and *Mr/M* for $SrCe_xFe_{12-x}O_{19}$ at different Ce^{3+} concentration.

The measurements inferred that the M and H_C values decrease with increasing Ce^{3+} content (Table 6.2). This decrease in M can be explained on basis of site occupation of Ce^{3+} ions. According to Gortor Model [195], Fe^{3+} ions are distributed to five different crystallographic sites. These sites are responsible for all increase or decrease of magnetic moment per unit formula. For example, if the substituted cation ions professionally occupy spin down sites, it leads to increase in M values. The decrease in M in present work with Ce^{3+} content can be attributed to replacement of Fe^{3+} ions from spin-up sites. This is because the cerium ions lower in magnetic moment (2.54 μ_B) than Fe^{3+} (5 μ_B) ions which results in decrease of superexchange interaction. The reduction in magnetic Fe^{3+} ions deviate the arrangement from collinear to non-collinear because the magnetic ions are collinearly organized in a ferrimagnetic order due to the superexchange interactions. This environmental disorder as well as cationic vacancy arise spin canting activity in nanomaterials on the substitution of rare earth element in iron sites materials that promotes the reduction of magnetic moment interactions [196], consequently M value decreases. The coercivity values decrease with increasing content of x, but for x = 1.0, value decreases abruptly.

Table 6.2: Values of magnetization, coercivity and squareness ratio for $SrCe_xFe_{12-x}O_{19}$ sample.

$SrCe_xFe_{12-x}O_{19}$	x = 0.0	x = 0.23	x = 0.43	x = 0.63	x = 0.83	x = 1.0
***M*(emu/g)**	51.97	49.50	46.31	43.97	41.47	38.91
H_C(Oe)	6258.54	6184.45	6036.25	6052.78	5597.35	239.39
Mr/M	0.58	0.60	0.59	0.60	0.58	0.47

The first decay of H_C values up to x = 0.83 may be due to the presence of or increase in the strength of secondary phase which restrict (or hinder) the orientation of ferromagnetic ions. The abrupt decrease for x = 1.0 is due to the abundance of strong

magnetocrystalline anisotropic ions at octahedral site in the system which might be destroying the ferrimagnetic arrangement that weakens the strength of superexchange (Fe^{3+}-O^{2-}-Fe^{3+}) interactions [197,198]. Moreover, an increase of porosity as seen in Table 6.1 with Ce^{3+} content leads the dilution of magnetic properties due to the presence of pores resulting to deterioration of extrinsic magnetic parameters [199]. The SQR ratio of Ce^{3+} doped hexaferrite nanoparticles lies in the range 0.47-0.60. SQR value increases with increase in doping concentrations and sharp decrease has been observed for higher concentration. This may be attributed to the presence of intermediate phases in the system. Basically, the existences of high SQR for all the doped hexaferrite nanoparticles are mainly due to two the factors. Firstly, it is due the doping of highly anisotropic materials in ferrite host lattice and secondly, the calcinated samples are not completely saturated at the maximum applied field.

6.4 Conclusions

The structural analysis confirms the formation, but secondary phase has been grown in the expense of ferrite phase. However, the strength of secondary phase increases with an increase in Ce^{3+} content. The absorption band in the frequency range 435 cm^{-1} and 595 cm^{-1} confirms the formation of ferrite phase. The well shaped hexagonal nanoparticles have been obtained for pure compound. The morphologies become irregular with an increase in concentration even at low concentration. M and H_C values have been decreased with an increase in Ce^{3+} content. This decrease in M can be attributed to replacement of Fe^{3+} ions from spin-up sites with lower magnetic moment. The abundance of strong magnetocrystalline anisotropic ions and an increase of porosity in the system with Ce^{3+} content lead to the dilution of H_C.

CHAPTER VII

Summary

Hexagonal ferrites form an important class of materials which are used in various scientific and technological applications. Here we have studied the synthesis and characterizations of $SrFe_{12}O_{19}$ and doped nanoparticles *viz.* $SrLa_xFe_{12-x}O_{19}$, $SrCe_xFe_{12-x}O_{19}$ and $SrNd_xFe_{12-x}O_{19}$ (x = 0.0, 0.23, 0.43, 0.63, 0.83 and 1.0). The work has been systematically described in seven different chapters: Chapter I contains a brief introduction of nanoferrites and their general properties. Techniques for the growth of nanoferrites and a review of the published literature have also been described in the same chapter. The synthesis of samples and details of the instrument used for characterization of the synthesized materials: XRD, FTIR, SEM, and VSM have been briefly described in chapter II.

Chapter III deals with results on synthesis and characterization of the pure strontium hexaferrite nanoparticles. In this chapter the crystallization kinetics of strontium hexaferrite has been investigated by means of TG/DTG/DTA. Thermal analysis reveals that the formation takes place in steps by mean of endothermic reaction. XRD analysis has also been used to confirm this formation of a precursor powder calcinated at 700°C and 800°C in air atmosphere. From the structural analysis it is clear that the existence of an intermediate phase have been in accordance with thermal analysis. However, the presence of α-Fe_2O_3 in the system infers that phase means the system need longer and high calcination temperature for the completion of reaction. As the calcination temperature of precursor powder increases to 1200°C, the diffraction peak becomes narrower and intense representing enhancement of crystallite size and crystallinity respectively. The diffraction peak broadening technique has been employed for most intense (114) peak to calculate the crystallite size. The sample calcinated at 1200°C stands for maximum crystallite size but still smaller than the single domain crystal particle size ~270 nm as reported earlier. The growth of crystallite size with increasing calcination temperature can be accredited to the fusion of nanoparticles with each other by melting their surfaces. The fusion of nanoparticles well below their melting point is owing to weak binding of surface atoms result in sharp decrease of surface melting point. The presence of impurities or incomplete reaction in samples results in a sheet like structure. As discussed above with the increase in calcination temperature it mends the crystallinity of ferrite phase

and can be describe in terms of Ostwald ripening. Mid-IR analysis has also confirmed the formation of hexaferrite. The influence of calcination temperature, impurities, and morphology as well as preparation technique on the magnetic properties of ferrite system have been studied. As expected, it has been observed that the magnetic properties perk up as the calcination temperature increases and the optimum values for prepared $SrFe_{12}O_{19}$ is at 1200°C. The continuous improvement in magnetic parameters can be indorsing to the progressive reaction between un-reacted constituents of iron oxide and non-ferromagnetic monoferrite to form 100% single phase hexaferrite (crystallinity increases with calcination). The obtained optimum result for sample calcinated at 1200°C are consistent with the thermal analysis indicates the formation of pure magnetoplumbite phase.

Chapter IV-VI deals with the effects of rare earth elements on the structural, morphological and magnetic properties of strontium hexaferrite nanoparticles. Structural analysis of Lanthanum (La^{3+}) doped strontium ferrite confirms the formation of ferrite phase along with the presence of α-Fe_2O_3 (32.9°) phase in diffraction pattern of pure compound. The crystallinity of the particles has improved with an increase in doping concentration and calcination. It has also been seen that the strength of intermediates start decreasing and new set of diffraction peaks related to hexagonal system increases. Still the presence of α-Fe_2O_3 at 32.9° indicates the incomplete reaction between the intermediates for the crystallization process. La^{3+} content shows significant effect on structural properties *i.e.* as the La^{3+} concentration increases, the secondary phase has disappeared even at $x = 0.23$. It means La^{3+} ions rearrange themselves in the host lattice without disturbing the parent lattice and Fe^{3+}/Sr^{2+} molar ratio less than 12 is more favourable to achieve single phase hexaferrite at calcination temperature of 900°C for 4h. The *D* size has been determined using the Scherer's formula and decreases with an increase in La^{3+} content. This decrease in *D* with an increase in doping can be explained on the basis of bond energy or crystallization of doped hexaferrite nanoparticles. Similar results have been obtained for Nd^{3+}-doped ferrite. Ce^{3+} shows the opposite behavior under similar conditions and it confirms the formation but with the presence of extra diffraction peak related to cerium oxide as a new phase in the system. The strength of

secondary phase increases with an increase in Ce^{3+} content. This means that the Ce^{3+} ions do not enter into the crystal structure under present synthesis conditions and it provokes the growth of secondary phase at the expense of ferrite phase. The structural analysis of La^{3+} and Nd^{3+} indicates that the iron deficient non-stoichiometric (Fe^{3+}/Sr^{2+} less than 12) compositions are more favourable for the formation of single phase ferrite nanoparticles. However, the Ce^{3+} doped system needs high calcination for the exclusion of all the secondary phases found in the system. The nanoparticles of rare earth elements doped ferrite with hexagonal crystal structure having crystallite size in the range 31-36 nm can be used to minimize the EMI and aid to achieve desired signal to noise ratio for high density recording media. The infrared spectroscopy gives detailed information regarding the change in structural environment as well as it enables us to identify the possible chemical species in the system during the calcination or incorporation of foreign atoms in the parent compound. Mid-IR analysis is in good agreement with the results of thermal and structural analysis, where the precursor powder shows weight loss due to the evaporation of water content from the precursor (in TG-curve). The broad absorption bands in the range 3200-3270 cm^{-1} and the frequency bands in the range 400-800 cm^{-1} confirms the presence of water content and intermediates of iron oxides. As the calcination temperature increases, the strength of intermediate phases decreased or disappeared after the calcination. The new set of characteristic peaks at 430-450 cm^{-1} and 580-590 cm^{-1} have appeared and corresponds to the stretching vibrations of metal-oxygen bond indicates the formation of hexaferrite phase.

Micrograph of precursor powder shows the uneven distribution of particles and non-uniformity. Substitution and heat treatment influence the morphologies of the particles. The particles are well shaped and homogeneous throughout the surface of sample for undoped compound. As the dopant (La^{3+} and Nd^{3+}) concentration increases sample become irregular. The microstructure of Ce^{3+} doped compound found to be more irregular even at low concentration comparatively. This may be due to the presence of secondary phases in system and their strength increases with increase in concentration of dopant content. The micrographs of the prepared samples exhibit porous and agglomerated microstructure. This can be due the release of gases during

the combustion or decomposition process and magnetic nature of the particles might be responsible for high porosity and agglomeration respectively.

The intrinsic parameter *M* for La^{3+}, Nd^{3+} and Ce^{3+} doped ferrite decreases with an increase in doping concentration while extrinsic parameter H_C increases except for Ce^{3+} (Table 7.1). The inclusion of Ce^{3+} ions in the same system results in dilution of extrinsic parameter. Cause of this distinct behavior for Ce^{3+} doped system can be attributed to incomplete crystallization and low solubility of rare earth element in strontium ferrite lattice, leads to the formation of intermediates. Among the three, La^{3+} and Nd^{3+} dopant contributes in the improvement of H_C in a positive way while Ce^{3+} ions do not enter into the crystal structure properly under similar synthesis conditions. It has been concluded that the addition of rare earth metals on strontium ferrite enhances the magnetocrystalline anisotropy of system, but all the ions does not respond in the similar way. The comparison of magnetic properties for various dopants has been shown in Figure 7.1.

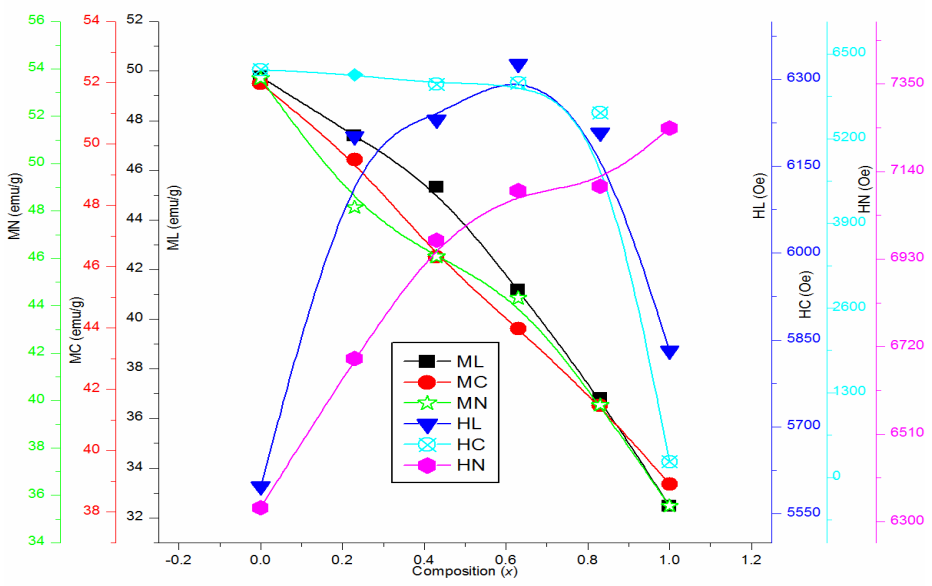

Figure 7.1: Comparative graph of magnetic parameters of La^{3+}, Nd^{3+} and Ce^{3+} doped strontium hexaferrite, where, ML, MN, MC and HL, HN, HC stands for magnetization of lanthanum (L), magnetization of neodymium (N), magnetization of cerium (C) and coercivity of lanthanum (L), coercivity of neodymium (N), coercivity of cerium (C), respectively.

Table 7.1: Comparative studies of La^{3+}, Nd^{3+} and Ce^{3+} doped strontium hexaferrite for various properties *viz.* XRD, IR, SEM and VSM.

Composition	XRD	IR	SEM	VSM
Precursor Powder	Intermediate Phases	Confirms	Irregular shape	The precursor powder shows almost paramagnetic behaviour due to the presence of non-magnetic secondary phases.
$SrFe_{12}O_{19}$	Confirms the formation. The calcination temperature amends the structural properties and Fig. 3.3d represents the sharp, intense and narrower diffraction peaks with high crystallinity for sample calcinated at 1200°C.	Confirms	Flawless hexagonal particles with well resolved structure have been obtained for the same.	The magnetic parameters *viz. M* (57.76 emu/g) and H_C (6828.54 Oe) have been improved with calcination. The results are in accordance with structural and thermal properties.
$SrLa_xFe_{12-x}O_{19}$	XRD analysis reveals that the diffraction peak positions for La^{3+} doped hexaferrite nanoparticles exactly appears at same position as for the pure compound.	Confirms	Morphological investigation points that La^{3+} content retards the grain growth and the sample exhibits porous and agglomerated microstructure, Figure 4.3(c-d).	The magnetization values have been decreased with increase in La content while H_C increases. The optimum coercivity (6326.94 Oe) value has been obtained for La content (x = 0.63).
$SrNd_xFe_{12-x}O_{19}$	The influence of the Nd^{3+} substitution, Fe^{3+}/Sr^{2+} molar ratio and the calcination temperature on the crystallization of ferrite phase have been examined for Nd^{3+} doped hexaferrite nanoparticles. The structural analysis reveals that the Nd^{3+} ions rearrange themselves in the host lattice without disturbing the parent lattice and Fe^{3+}/Sr^{2+} molar ratio less than 12 is more favorable to achieve single phase hexaferrite at calcination temperature 900°C for 4h.	Confirms	The incorporation of Nd^{3+} shows better results than remaining rare earth elements up to higher concentration with preeminent structure. Still there is aggregation of nanoparticles for higher compositions due to magnetic interactions between the neighboring particles.	The magnetic output are directly associated with structural and morphological results. As they confirm Nd^{3+} ions directly enters in the ferrite lattice without disturbing host lattice. As a consequence, Nd^{3+} doped ferrite shows highest H_C value for highest Nd^{3+} content (x = 1.0).

$SrCe_xFe_{12-x}O_{19}$	XRD patterns confirm that all the diffraction peaks of calcinated powder are belongs to the standard hexagonal M-type ferrite. However, as Ce^{3+} content increases in the system extra peaks appear and their intensities increase with *x*.	Confirms	Under similar calcination conditions, Ce^{3+} ions lead the formation of irregular particles even at low concentration. This may be attributed to the presence of secondary phases in system and their strength.	The Ce^{3+} ions produced unexpected contradicted results for Ce^{3+} doped hexaferrite. The magnetic parameters *viz. M* and H_C found to be decreased with increase in Ce^{3+} content.

References

[1] Mansoori G A "Principle of nanotechnology: Molecular based study of Condensed Matter in small system" World Scientific Publishing Co. Pte. Ltd, ISBN 981-256-154-4, 2005.

[2] Cao G "Nanostructures and Nanomaterials" World Scientific Publishing Co. Pte. Ltd, ISBN 1-86094-415-9, 2003.

[3] Goldman A "Modern Ferrite Technology" Pittsburgh, PA, USA Library of Congress Control Number: 2005933499, 2nd edition 2006.

[4] Gopalan V "On the Synthesis and Multifunctional Properties of some Nanocrystalline Spinel Ferrites and Magnetic Nanocomposites" Cochin University of Science and Technology 2009.

[5] Gurkan N "Studies on interaction of electromagnetic waves with barium hexaferrite ceramics" the graduate school of natural and applied sciences of middle east technical university, 2008.

[6] Calleja A, Tijero E, Martinez B and Pifiol S 1999 *J. Magn. Magn. Mater.* **196-197** 293.

[7] Pereira F M M, Junior C A R, Santos M R P, Sohn R S T M, Freire F N A, Sasaki J M, Sohn R S T M, Freire F N A, Sasaki J M, de Paiva J A C and Sombra A S B 2008 *J. Mater. Sci. Mater. Electron.* **19** 627.

[8] Schmidt M W "Phase formation and structural transformation of strontium ferrite $SrFeO_x$" The Australian National University 2001.

[9] Sarnot S L, Mathur A and Govila R K 1997 *J Phys. IV France* 7 Colloque C1, Supplement au Journal de Physique III de mars C1-31.

[10] Information on https://www-03.ibm.com/press/us/en/pressrelease/29245.wss

[11] Rezlescu N, Doroftei C, Rezlescu E and Popa P D 2008 *J. Alloys Compd.* **451** 492.

[12] Panda R N, Shih J C and Chin T S 2013 *J. Magn. Magn. Mater.* **257** 79.

[13] R.R. Muslim "Magnetic Properties of Manganese Ferrite Nanoparticles" Thapar University Patiala 2012.

[14] Dey S, Roy A and Ghose J 2001 *J. Appl. Phys.* **90** 4138.

[15] R. Bharol "Synthesis and characterization of Manganese ferrite nanoparticles" Thapar University Patiala, 2011.

[16] Pullar R C 2012 *Prog. Mater. Sci.* **57** 1191.

[17] Ashiq M N "Effects on Physical, Electrical and Magnetic properties of Stronitum hexaferrite nanomaterials doped with binary mixture of various metal ions" Department of chemistry Quaid-I-Azam University, Islamabad" 2009.

[18] Angeles A G, Suarez G M, Gruskova A, Lipka J Papanova M and Slama J 2005 *J. Magn. Magn. Mater.* **285** 450.

[19] Craik D J, Hill E H 1977 *J. Phys. Colloque.* **38** C1–39.

[20] Dho J, Lee E K, Park J Y, Hur N H 2005 *J. Magn. Magn. Mater.* **285** 164.

[21] Chen J Z and Wu S K 2001 *J. Non-Cryst. Solids* **288** 159.

[22] Tyagi S, Agarwala R C and Agarwala V 2010 *Transactions of The Indian Institute of Metals* **63** 15.

[23] Kools F 1973 *Sci. Ceram.* **7** 27.

[24] Steier H P, Requena J and Moya J S 1999 *J. Mater. Res.* **14** 3647.

[25] Dursun S, Topkaya R, Akdogan N and Alkoy S 2012 *Ceram. Int.* **38** 3801.

[26] Tyagi S, Baskey H B, Agarwala R C, Agarwala V and Shami C 2011 *J. Electron. Mater.* **40** 2004.

[27] Benito G, Morales M P, Requena J, Raposo V, Vazquez M and Moya J S 2001 *J. Magn. Magn. Mater.* **234** 65.

[28] Lisjak D and Drofenik M 2007 *J. Eur. Ceram. Soc.* **27** 4515.

[29] Chin T S, Hsu S L, Deng M C 1993 *J. Magn. Magn. Mater.* **120** 63.

[30] Hasab M G, Ebrahimi S A S and Badiei A 2007 *J. Non-Cryst. Solids* **353** 814.

[31] Hasab M G, Ebrahimi S A S and Badiei A 2007 *J. Eur. Ceram. Soc.* **310** 2477.

[32] Cullity B D and Graham C D Introduction to Magnetic Materials, 2nd ed. (Hoboken, NJ: Wiley, 2008).

[33] Jin Z, Tang W, Zhang J, Lin H and Du Y 1998 *J. Magn. Magn. Mater.* **182** 231.

[34] Ebrahimi S A S, Kianvash A, Ponton C B and Harris I R 2000 *Ceram. Int.* **26** 379.

[35] Fang Q, Liu Y, Yin P and Li X 2001 *J. Magn. Magn. Mater.* **234** 366.

[36] Kumar K V and Ravinder 2001 *Int. J. Inorg. Mater.* 3 661.

[37] Sileo E E, Rotelo R and Jacobo S E 2002 *Phys. B: Condens. Matter* **320** 257.

[38] Wang X, Li L, Shu S, Yue Z, Ma Z and Zhou J 2002 *J. Cryst. Growth* **55** 8.

[39] Singh A K, Verma A, Thakur O P, Prakash C, Goel T C and Mendiratta R G 2003 *Matter. lett.* **57**1040.

[40] Thakur A and Singh M 2003 *Ceram. Int.* **29** 505.

[41] Wang J and Zeng C 2004 *J. Cryst. Growth* **270** 729.

[42] Sivakumar M, Gedanken A, Zhong W, Du Y W, Bhattacharya D, Yeshurun Y and Felner I 2004 *J. Magn. Magn. Mater.* **268** 95.

[43] Lechevallier L and Breton J M 2005 *J. Magn. Magn. Mater.* **290–291** 1237.

[44] Verma A, Thakur O P, Prakash C, Goel T C and Mendiratta R G 2005 *Mater. Sci. and Eng. B* **55** 8.

[45] Dimri M C, Verma A, Kashyap S C, Dube D C, Thakur O P and Prakash C 2006 *Mater. Sci. and Eng. B* **133** 42.

[46] Alamolhoda S, Ebrahimi S A S and Badiei A 2006 *J. Magn. Magn. Mater.* **303** 69.

[47] Doroftei C, Rezlescu E, Popa P D and Rezlescu N 2006 *Cryst. Res. Technol.* **41** 1112.

[48] Shirtcliffe N J, Thompson S, O Keefe E S, Appleton S and Perry C C 2007 *Mater. Res. Bull.* **42** 281.

[49] Litsardakis G, Manolakis I, Serletis C and Efthimiaadis K G 2007 *J. Magn. Magn. Mater.* **316** 170.

[50] Pan X, Mu G, Shen H and Gu M 2007 *Appl. Surf. Sci.* **253** 4119.

[51] Ghasemi A and Morisako A 2008 *J. Magn. Magn. Mater.* **320** 1167.

[52] Iqbal M J and Ashiq M N 2008 *Chem. Eng. J.* **136** 383.

[53] Soibam I, Phanjoubam S, Sharma H B, Sarma H N K and Prakash C 2009 *Phys. B: Condens. Matter* **404** 3839.

[54] Costa A C F M, Vieira D A, Silva V J, Diniz V C S, Kiminami R H G A and Gama L 2009 *J. Alloys Compd.* **483** 37.

[55] Jacobo S E, Herme C and Bercoff P G 2010 *J. Alloys Compd.* **495** 513].

[56] Raghavender A T, Zadro K, Pajic D, Skokko Z and Biliskov N 2010 *Matter. lett.* **64** 1144.

[57] Meena R S, Bhattachrya S and Chatterjee R 2010 *Mater. Sci. and Eng. B* **171** 133.

[58] Iqbal M J and Farooq S 2011 *Mater. Res. Bull.* **46** 662.

[59] Zhang Z, Liu X, Wang X, Wu Y and Li R 2012 *Journal of Alloys and Compounds* **525** 114.

[60] Zi Z F, Liu Q C Dai J M and Sun Y P 2012 *Solid State Commun.* **152** 894.

[61] Chang S, Kangning S and Pengfei C 2012 *J. Magn. Magn. Mater.* **324** 802.

[62] Li C J, Wang B and Wang J N 2012 *J. Magn. Magn. Mater.* **324** 1305.

[63] Piccirillo C Shortage of some elements: the problems and the challenges; March 7th 2011, http://www.suite101.com/content/shortage-of-some-elements-the-problems-and-the-challenges-a356603 [accessed February 2012].

[64] Aly K A, Othman A A and Abousehly A M 2009 *J. Alloys Compd.* **467** 417.

[65] Saxena M 2005 *J. Phys. D: Appl. Phys.* **38** 460.

[66] Kissinger H E 1956 *Journal of Research of the National Bureau of Standards* **57** 217 – 221.

[67] Mehta N, Agarwal P and Kumar A 2004 Indian Journal of Engineering and Materials Sciences **11** 511.

[68] Augis J A and Benett J E 1978 *J. Thermal. Anal.* **13** 283.

[69] Tang X, Yang Y and Hu K 2009 *J. Alloys Compd.* **477** 488.

[70] Singh R R 2005 "Studies on surface passivation of mercury cadmium telluride for IR detectors" Department of Physics Barkatullah University, Bhopal.

[71] Oh S W, Bang H J, Bae Y C and Sun Y K 2007 *J. Power Sources* **173** 502.

[72] Dixit G, Singh J P, Srivastava R C, Agrawal H M 2012 *J. Magn. Magn. Mater.* **324** 479.

[73] Khan I, Sadiq I, Naeem M, and Rana M 2011 *J. Alloys Compd.* **509** 8042.

[74] Khademi F, Poorbafrani A, Kameli P, Salamati H 2012 *J. Supercond. Nov. Magn.* **25** 525.

[75] Ahmad M, Aen F, Islam M U, Niazi S B and Rana M U 2011 *Ceram. Int.* 37 3691.

[76] Jeyaprakash B G, Kesavan K, Kumar R A, Mohan S and Amalarani A 2011 *Bull. Mater. Sci*. **34** 601.

[77] Stoner E C, Wohlfarth E P 1948 *Philos Trans. R. Soc.London, A* **240** 599.

[78] Song Q and Zhang Z J 2004 *J. Am. Chem. Soc.* **126** 6164.

[79] Liu X S, Garcia L F, Hu F, Zhu D R, Suarez M and Menendez J L 2012 *Mater. Chem. Phys.* **133** 961.

[80] Ebrahimi Y, Alvani A A S, Sarabi A A, Sameie H, Salimi R, Alvani M S and Moosakhani S 2012 *Ceram. Int.* 38 3885.

[81] Masoudpanah S M, Ebrahimi S A S and Ong C K 2012 *J. Magn. Magn. Mater.* **324** 1440.

[82] Davoodi A and Hashemi B 2012 *J. Alloys Compd.* **512** 179.

[83] Zhang Z, Liu X, Wang X, Wu Y and Li R 2012 *J. Alloys Compd.* **525** 114.

[84] Haq A and Rehman M A U 2012 *Physica B* **407** 822.

[85] Rai G M, Iqbal M A and Kubra K T 2010 *J. Alloys Compd.* **495** 229.

[86] Almeida R M, Paraguassu W, Pires D S, Correa R R and de Araujo Paschoal C W 2009 *Ceram. Int.* **35** 2443.

[87] Lima R D C, Pinho M S and Ogasawara T 2009 *J. Therm. Anal. Calorim.* **97** 131.

[88] Chakrabarti N and Maiti H S 1997 *Matter. lett.* **30** 169.

[89] Zhao W, Zhang Q and Guan J 2006 *J. Wuhan. Univ. Technol.* **21** 36.

[90] Tyagi S, Agarwala R C and Agarwala V 2011 *J. Mater. Sci. Mater. Electron.* **22** 1085.

[91] Iqbal M J and Farooq S 2011 *Mater. Res. Bull.* **46** 662.

[92] Kissinger H E 1957 *Anal. Chem.* **29** 1702.

[93] Augis J A and Benett J E 1978 *J. Thermal. Anal.* **13** 283.

[94] Matusita K and Sakka S 1979 *Phys Chem Glasses.* **20** 81.

[95] Shang H, Wang J and Liu Q 2007 *Mater. Sci. and Eng. A.* **456** 130.

[96] Yuan C L, Hong Y S and Lin C H 2011 *J. Magn. Magn. Mater.* **323** 1851.

[97] Zhanyong W, Liuming Z, Jieli L, Huichun Q, Yuli Z, Yongzheng F, Minglin J and Jiayue X 2010 *J. Magn. Magn. Mater.* **322** 2782.

[98] Mali A and Ataie A 2005 *Scr. Mater.* **53** 1065.

[99] Qiu J, Liang L and Gu M 2005 *Mater. Sci. and Eng. A.* **393** 361.

[100] Iqbal M J, Khan R A, Mizukami S and Miyazaki T 2011 *Mater. Res. Bull.* **46** 1980.

[101] Iqbal M J and Farooq S 2010 *J. Alloys Compd.* **505** 560.

[102] Fang Q, Cheng H, Huang K, Wang J, Li R and Jiao Y 2005 *J. Magn. Magn. Mater.* **294** 281.

[103] Chen D Y, Meng Y Y, Zeng D C, Liu Z W, Yu H Y and Zhong X C 2012 *Mater. Lett.* **76** 84.

[104] Kumar V, Rana A, Yadav M S and Pant R P 2008 *J. Magn. Magn. Mater.* **320** 1729.

[105] Matsuo Y, One K, Hashimoto T and Nakao F *2001 IEEE Trans. Magn.* **37** 2369.

[106] Hasab M G, Ebrahimi S A S and Badiei A 2007 *J. Magn. Magn. Mater.* **316** e13.

[107] Hasab M G, Ebrahimi S A S and Badiei A 2007 *J. Eur. Ceram. Soc.* **27** 3637.

[108] Song F, Shen X, Xiang J and Song H 2010 *Mater. Chem. Phys.* **120** 213.

[109] Shen X, Liu M, Song F and Meng X 2010 *J. Sol-Gel Sci. Technol.* **53** 448.

[110] Wang X, Li D, Lu L and Wang X 1996 *J. Alloys Compd.* **237** 45.

[111] Iqbal M J, Ashiq M N and Gul I H 2010 *J. Magn. Magn. Mater.* **322** 1720.

[112] Qiu J, Liang L and Gu M 2005 *Mater. Sci. and Eng. A.* **393** 361.

[113] Hsuan F Y and Pei C L 2006 *J. Alloys Compd.* **416** 222.

[114] Ashiq M N, Iqbal M J and Gul I H 2009 *J. Alloys Compd*, **487** 341.

[115] Doroftei C, Rezlescu E, Dorin P and Rezlescu N 2006 *Cryst. Res. Technol.* **41** 1112.

[116] Mingquan L, Fuzhan S, Xiangqian S and Yongwei Z 2010 *J. Sol-Gel Sci. Technol.* **56** 39.

[117] Durmus Z, Kavas H, Sozeri H, Toprak M S, Aslan A and Baykal A 2012 *J. Supercond. Nov. Magn.* **25** 1185.

[118] Ostwald W Z 1900 *Phys. Chem.* **34** 495.

[119] Sudakar C, Subbanna G N and Kutty T R N 2001 *J. Electroceram* **6** 123.

[120] Ai L and Jiang J 2009 *J. Mater. Sci. Mater. Electron.* **20** 257.

[121] Xu P, Han X and Wang M 2007 *J. Phys. Chem. C,* **111** 5866.

[122] Stoner E C and Wohlfarth E P 1991 *IEEE Trans. Magn.* **27** 3475.

[123] Herzer G 1991 *Mater. Sci. Eng. A*, **133** 1.

[124] Piramanayagam S N 2007 *J. Appl. Phys.* **102** 011301.

[125] Morisakoa A, Naka T, Ito K, Takizawa A, Matsumoto M and Hong Y K 2012 *J. Magn. Magn. Mater.* **242** 304.

[126] Kazin P E, Trusov L A, Zaitsev D D, Tretyakov Yu D and Jansen M 2008 *J. Magn. Magn. Mater.* **320** 1068.

[127] Iqbal M J, Ashiq M N, Gomez P H, Munoz J M M and Cabrera C T 2010 *J. Alloys Compd.* **500** 113.

[128] Zi Z F, Liu Q C, Dai J M, Sun Y P 2012 *Solid State Commun*. **152** 894.

[129] Meaz T M and Koch C B 2005 *Hyperfine Interact*. **166** 455.

[130] Xiong G, Xu M and Mai Z 2001 *Solid State Commun.* **118** 53.

[131] Deschamp A, Bortant E and Acad C R 1957 *Sci. Paris* **224** 3069.

[132] Zhidong H, Limin D, Ze W and Xianyou Z 2006 *J Rare Earth* **24** 75.

[133] Nair J P, J.R., Chaure N B and Pandey R K 1998 *Semicond. Sci. Technol.* **13** 340.

[134] Peng Z, Fu X, Ge H, Fu Z, Wang C, Qi L and Miao H 2011 *J. Magn. Magn. Mater.* **323** 2513.

[135] Iqbal M J, Ashiq M N and Gomez P H 2009 *J. Alloys Compd.* **478** 736.

[136] Yu H F and Lin H Y 2004 *J. Magn. Magn. Mater.* **283** 190.

[137] Tang X, Zhao B Y and Hu K A 2006 *J. Mater. Sci.* **41** 3867.

[138] Singh J P, Dixit G, Srivastava R C, Agrawal HM and Asokan K 2011 *J. Phys. D: Appl. Phys.* **44** 435306.

[139] Khademi F, Poorbafrani A, Kameli P and Salamati H 2012 *J. Supercond. Nov. Magn.* **25** 525.

[140] Capitaneo J L, Caffarena V da R, Ogasawara T and Pinho M S 2008 *Material research* **11** 319.

[141] Qi Y, Yang Y, Zhao X, Liu X, Wu P, Zhang F and Xu S 2010 *Particuology* **8** 207.

[142] Franco A and Silva M S 2011 *J. Appl. Phys.* **109** 07B505.

[143] Jacobo S E, Herme C and Bercoff P G 2010 *J. Alloys Compd.* **495** 513.

[144] Mozaffari M, Arab A, Yousefi M H and Amighian J 2010 *J. Magn. Magn. Mater.* **322** 2670.

[145] Ounnunkad S 2006 *Solid State Commun.* **138** 472.

[146] Yang Z, Wang C S, Li X H and Zeng H X 2002 *Mater. Sci. and Eng. B* **90** 142.

[147] Li C J, Wang B and Wang J N 2012 *J. Magn. Magn. Mater.* **324** 1305.

[148] Hemeda D M and Hemeda O M 2008 *J. Magn. Magn. Mater.* 320 1557.

[149] Mali A and Ataie A 2004 *Ceram. Int.* **30** 1979.

[150] Wane I, Bessaudou A, Cosset F, Ce A, Girault C, Decossas J L and Vareille J C 2000 *J. Magn. Magn. Mater.* **211** 309.

[151] Mohsen Q 2010 *J. Alloys. Compd.* **500** 125.

[152] Anjum S, Rafique M S, Khaleeq-ur-rahman M, Siraj K and Usman A 2012 *J. Magn. Magn. Mater.* **324** 711.

[153] Drmota A, koselj J, Drofenik M and Znidarsic A 2012 *J. Magn. Magn. Mater.* **324** 1225.

[154] Sharbati A, Choopani S, Azar A and Senna M 2010 *Solid State Commun.***150** 2218.

[155] Pereira F M M, Junior C A R, Santos M R P, Sohn R S T M, Freire F N A, Sasaki J M, Sohn R S T M, Freire F N A, Sasaki J M, de Paiva J A C and Sombra A S B 2008 *J. Mater. Sci. Mater. Electron.* **19** 627.

[156] Murtaza G, Iqbal M A and Kubra K T 2010 *J. Alloys. Compd.* **495** 229.

[157] Zi Z F, Sun Y P, Zhu X B, Yang Z R, Dai J M and Song W H 2008 *J. Magn. Magn. Mater.* **320** 2746.

[158] Lechevallier L, Le Breton J M, Morel A and Tenaud P 2008 *J. Phys. Condens. Matter.* **20** 175203.

[159] Kaur B, Bhat M, Licci F, Kumar R, Kulkarni S D, Joy P A, Bamzai K K and Kotru P N 2006 *J. Magn. Magn. Mater.* **305** 392.

[160] Luo J 2012 *Mater. Lett.* **80** 162.

[161] Mu G, Pan X, Shen H and Gu M 2007 *Mater. Sci. and Eng. A* **445** 563.

[162] Gharagozlou M 2010 *J. Alloys. Compd.* **495** 217.

[163] Khademi F, Poorbafrani A, Kameli P and Salamati H 2012 *J. Supercond. Nov. Magn.* **25** 525.

[164] Dixit G, Pal J, Srivastava R C and Agrawal H M 2012 *J. Magn. Magn. Mater.* **324** 479.

[165] Fuji M, in: M. Hosokawa, K. Nogi, M. Naito, T. Yokoyama (Eds.), Nanoparticle technology handbook, Elsevier, 2012, pp. 21.

[166] Kumar P, Sharma S K, Knobel M, Chand J and Singh M 2011 *J. Electroceram.* **27** 51.

[167] Rezlescu N, Doroftei C, Rezlescu E and Popa P D 2008 *J. Alloys. Compd.* **451** 492.

[168] Dhage V N, Mane M L, Keche A P, Birajdar C T and Jadhav K M 2011 *Phys. B: Condens. Matter* **406** 789.

[169] Kaur B, Bhat M, Licci F, Kumar R, Kotru P N and Bamzai K K 2004 *Nucl. Instr. Meth. Phys. Res. B* **222** 175.

[170] Barati M R 2009 *J. Alloys. Compd.* **478** 375.

[171] Badapanda T, Rout S K, Panigrahi S and Sinha T P 2008 *Bull. Mater. Sci.* **31** 897.

[172] Singhal S, Namgyal T, Singh J, Chandra K and Bansal S 2011 *Ceram. Int.* **37** 1833.

[173] Liu M, Song F and Shen X 2010 *J. Sol-Gel Sci. Technol.* **56** 39.

[174] Gadkari A B, Shinde T J and Vasambekar P N 2009 *Mater. Charact.* **60** 1328.

[175] Wu X, Wu W, Cui X and Liao S 2012 *J. Therm. Anal. Calorim.* **107** 625.

[176] Topal U and Bakan H I 2010 *J. Eur. Ceram. Soc.* **30** 3167.

[177] Lisjak D, Bobzin K, Richardt K, Begard M, Bolelli G, Lusvarghi L, Hujanen A, Lintunen P, Pasquale M, Olivetti E, Drofenik M and Schläfer T 2009 *J. Eur. Ceram. Soc.* **29** 2333.

[178] Liu Y, Michael, Drew G B and Liu Y 2011 *J. Magn. Magn. Mater.* **323** 945.

[179] Kikuchi T, Nakamura T, Yamasaki T, Nakanishi M, Fujii T, Takada J and Ikeda Y 2010 *J. Magn. Magn. Mater.* **322** 2381.

[180] Xie Y, Hong X, Gao Y, Li M, Liu J, Wang J and Lu J 2012 *Synth. Met.* **162** 677.

[181] Pileni M P 2001 *Adv. Funct. Mater.* **11** 323.

[182] Batlle X, Muro M G, Tejada J, Pfeiffer H, Gornert P, Batlle X, Garcfa M,Tejada J, Pfeiffer H and Sinn E 2012 *J. Appl. Phys.* **3333** 3333.

[183] Yu R H, Basu S, Zhang Y, Majidi A P and Xiao J Q 1999 *J. Appl. Phys.* **85** 6655.

[184] Zhang H, Zhou J, Wang Y, Li L, Yue Z, Wang X, Gui Z 2002 *Matter. Lett.* **56** 397.

[185] Bao J, Zhou J, Yue Z, Li L, Gui Z 2012 *J. Magn. Magn. Mater.* **250** 131.

[186] Tyagi S, Baskey H B, Agarwala R C, Agarwala V, Shami T C 2011 *Ceram. Int.* **37** 2631.

[187] Wang Y, Li L, Liu H, Qiu H and Xu F 2008 *Matter. Lett.* **62** 2060.

[188] Sankaranarayanan V K and Khan D C 1996 *J. Magn. Magn. Mater.* **153** 337.

[189] Iqbal M J and Khan R A 2009 *J. Alloys Compd.* **478** 847.

[190] Thankachan S, Jacob B P, Xavier S and Mohammed E M 2013 *Phys. Scr.* **87** 025701.

[191] Zhao L, Yang H, Yu L, Cui Y 2006 *J. Mater. Sci.* **41** 3083.

[192] Naeem M, Javed M and Hussain I 2011 *J. Magn. Magn. Mater.* **323** 259.

[193] Li J, Wu Y, Pan Y and Guo J 2007 *Ceram. Int.* **33** 735.

[194] Jiang J and Ai L H 2010 *J. Alloys. Compd.* **502** 488.

[195] Gorter E F 1957 *Proc. IEEE* 104B 255S.

[196] Ahmed M A, Okasha N, and Kershi R M 2008 *J. Magn. Magn. Mater.* **320** 1146.

[197] Anbarasu V, MdGazzali P M, Karthik T, Manigandan A and Sivakumar K 2013 *J Mater Sci: Mater. Electron.* **24/3** 916.

[198] Dimri M C, Khanduri H, Kooskora H, Subbi J, Heinmaa I, Mere A, Krustok J and Stern R 2012 *Phys. Status Solidi A.* **209/2** 353.

[199] Hemeda D M and Hemeda O M 2008 *J. Magn. Magn. Mater.* **320** 1557.